

Facultad de Física  
Departamento de Física Atómica, Molecular y Nuclear



VNIVERSITAT  
DE VALÈNCIA

# TRITIUM: Design, Construction and Commissioning of an In-Water Tritium Detector

Marcos Martínez Roig

PhD in Physics  
June 2, 2021

Under the supervision of:  
José Díaz Medina  
Nadia Yahlali Haddou



*Dedicated to  
my family*

Sometimes it is the people no one imagines anything  
of who do the things that no one can imagine.

"Alan Turing"

I



# Acknowledgements

Al echar la mirada atrás a estos años de trabajo y formación como investigadora, siento que ha habido muchas personas que me han ayudado directa o indirectamente en esta aventura, por lo que no puede faltar este espacio para agradecer la ayuda que he recibido.

Durante estos 4 años han sido muchas las personas que me han ayudado. Espero no dejarme a nadie.

Ver memoria de "Detectores monolíticos y sensores compatibles con altos campos magnéticos para tomografía por emisión de positrones"

AGRADECER A:

- Gente de tritium Valencia: PEPE, NADIA, MIREIA, ANA, MARQUITOS, ANDREA.
- Gente del LARAM -> TERESA, VANESA, ROSA, CLODO
- Gente de Tritium -> GENTE DE PORTUGAL, Antonio y Jose Angel de extremadura, gente de francia...
- Gente que ha aportado al trabajo:
  - Gente de DUNE (Anselmo, Miguel, Justo)
  - Gente de NEXT (Vicente, Marc, Javier, la chica, etc...)

- Ingeniero electrónico David Calvo del IFIC
  - Gente del IFIMED (Ana Ros, Jhon Barrio y Gabriela Llosa del IFIMED, Rita, Jorge, Marina)
  - Gente de Espectrometría Gamma (El hombre y su mujer, Cesar, Ion, el doctorado, etc)
  - Gente de ATLAS (Urmila, Carlos Mariñas)
  - Gente del ICMOL (El que manda, Lidon)
  - Departamento de mecánica del IFIC (Manolo "Apellidos", Jose Luis Jordan, Jose Vicente Civera Navarrete, Tchogna Davis, Daniel)
  - departamento de electrónica del IFIC (Jorge Nacher Arándiga, Manu ... y el otro )
  - Al departamento de informática (gente)
- Gente externa que ha ayudado
    - DAVID CANAL DE SAMTEC
    - A LUIS FERR... DE PETSYS..
  - Gente externa que no ha ayudado
    - Grupo de amigos del IFIC (nombrar a todos, tanto en el master como en el doctorado)
    - Familia
    - Amigos del pueblo
  - Al programa interreg sudoe -> Soporte financiero!

A carlos por todo su trabajo aportado a esta tesis (TRITIUM-Aveiro 0 prototype and simulations)

# Abstract

Tritium is one of the most abundantly emitted radioisotopes in a nuclear power plant. Large quantities of tritium are normally produced in the water of their cooling system, which are finally emitted to the environment. Due to the fact that high quantities of tritium could be dangerous for human health and for the environment, there exist several normative around the world which try to control this radioactive emissions in each country, like the Directive Europeen 2013/51/Euratom, which establishes the tritium limit in drinking water in Europe to 100 Bq/L, or the U. S. Environmental Protection Agency, in United States, whose tritium limit in drinking water is established at 740 Bq/L.

Nowadays, due to such a low energy emitted in the tritium decay, high sensitive detectors are needed for measuring it like LSC. The problem with LSC is that it is an off-line method the measurement process of which can take up to 3 or 4 days, too much time if there are any problem with the NPP.

Detectors based on solid scintillators is a promissing idea for building a tritium detector that works in quasi-real time. This type of detectors has been developed so far succesfully but without achieving enough sensibility for measuring the legal limits.

In this study the results of TRITIUM project is presented. In the

framework of this project a quasi-real time monitor for low tritium activities in water have been developed . This monitor is based on a tritium detector that contains several detection cells which are read in parallel, several active vetos and a pasive shielding for reducing the natural background of our system and an ultrapure water system to prepare the sample before being measured. Each detection cell is made up of hundreds of scintillating fibers read out by PMTs or SiPM arrays.

The final objective of this monitor will be the radiological protection around the nuclear power plant. This monitor will provide an alarm in case of an unexpected tritium release. It will be included in the early alarm system of Extremadura consisting of several detectors the objective of which is to reduce the impact of Nuclear Power Plants to the environment.

**Keywords:** Tritium in water, Real-time monitor, Nuclear Power Plant, Environmental Safety, ...

# Nomenclature and Acronyms

Acronyms:

<i>ICRU</i>	— International Commission of Radioactivity Units and Measurements
<i>ICRP</i>	— International Commission on Radiological Protection
<i>ISR</i>	— International Society of Radiology
<i>UNSCEAR</i>	— United Nations Scientific Committee on the Effects of Atomic Radiation
<i>IAEA</i>	— International Atomic Energy Agency
<i>UN</i>	— United Nations
<i>EU</i>	— European Union
<i>EURATOM</i>	— European Atomic Energy Community
<i>CSN</i>	— Nuclear Safety Council
<i>REA</i>	— Network of automatic stations
<i>REM</i>	— Network of sampling stations
<i>quasi-real</i>	— Less than 10 minutes
<i>LSC</i>	— Liquid Scintillation Counting
<i>PMT</i>	— PhotoMultiplier Tub
<i>SiPM</i>	— Silicon PhotoMultiplier
<i>NPP</i>	— Nuclear Power Plants
<i>U.S.DOE</i>	— United States Department of Energy
<i>U.S.</i>	— United States
<i>PWR</i>	— Pressurized Water Reactor

<i>BWR</i>	— Boiled Water Reactor
<i>HWR</i>	— Heavy Water Reactor
<i>GCR</i>	— Gas-Cooled Reactor
<i>USA</i>	— United States of America
<i>LARAM</i>	— Laboratorio de Radiactividad Ambiental
<i>WHO</i>	— World Health Organization
<i>ALARA</i>	— As Low As Reasonably Achievable
<i>GL</i>	— Guideline
<i>EPA</i>	— Environmental Protection Agency
<i>LDL</i>	— Lower Detection Limit
<i>IC</i>	— Ionization Chamber
<i>BIXS</i>	— Beta Induced X-ray Spectrometry
<i>SDD</i>	— Silicon Drift Detector
<i>APD</i>	— Avalanche Photodiode
<i>EEC</i>	— European Economic Community
<i>CNRS</i>	— Le Centre National de la Recherche Scientifique, France
<i>PMMA</i>	— Polymethyl Methacrylates
<i>CCD</i>	— Charge-Coupled Device
<i>HV</i>	— High Voltage
<i>QE</i>	— Quantum Efficiency
<i>CE</i>	— Collection Efficiency
<i>MPPC</i>	— Multi-Pixel Photon Counter
<i>G – APD</i>	— Geiger Avalanche Photodiode
<i>SSPM</i>	— Solid State PhotoMultiplier
<i>MRS – ADP</i>	— Metal-Resistor-Semiconductor Avalanche Photodiode
<i>MAPD</i>	— Micro-Pixel Avalanche Photodiode
$\lambda$	— Wavelength
$\lambda_p$	— Maximum wavelength of the associated spectrum
<i>PDE</i>	— Photodetection Efficiency of the SiPM
<i>C<sub>t</sub></i>	— Terminal Capacitance of the SiPM
<i>G<sub>SiPM</sub></i>	— Gain of the SiPM

$V_{BR}$	— Breakdown Voltage of the SiPM
$\Delta TV_{op}$	— Temperature Coefficient (mV/ $^{\circ}C$ )
$q_e$	— Electron Charge
$\sigma_T$	— Total Uncertainty of the Measurement
$\sigma_{st}$	— Stadistical Component of the Uncertainty
$\sigma_{si}$	— Sistematically Component of the Uncertainty
$A_m$	— Activity Measured
$10 \mu\text{Sv}/\text{cm}$	— MicroSievert per Centimeter
$HPGe$	— High Purity Germanium Detector
$ROI$	— Region of interest
$PHWR$	— Pressurized Heavy Water Reactor
$UDL$	— Upper Detection Limit
$LWR$	— Liquid Water Reactor

### Atomic and nuclear symbols

${}_1^1\text{H}$	— Hydrogen
${}_1^2\text{H}$	— Deuterium (Non-Radiactive Hydrogen Isotope)
${}_1^2\text{D}$	— Deuterium (Non-Radiactive Hydrogen Isotope)
${}_1^3\text{H}$	— Tritium (Radiactive hydrogen Isotope)
${}_1^3\text{T}$	— Tritium (Radiactive hydrogen Isotope)
${}_6^{14}\text{C}$	— Carbon
${}_{19}^{40}\text{K}$	— Potassium
${}_{86}^{226}\text{Ra}$	— Radon
${}_2^3\text{He}$	— Isotope of the Helium(Non-radiactive, 1 neutrons)
${}_7^{14}\text{N}$	— Nitrogen
${}_6^{12}\text{C}$	— Carbon
${}_3^6\text{Li}$	— Lithium Isotope
${}_3^7\text{Li}$	— Lithium
${}_5^{10}\text{B}$	— Boron
${}_8^{16}\text{O}$	— Oxygen

# X

$^{222}_{86}\text{Rn}$	— Radon
$^{40}_{19}\text{K}$	— Potassium
$^{137}_{55}\text{Cs}$	— Cesium
n	— Free Neutron
$\text{H}_2\text{O}$	— Usual Water
$\text{D}_2\text{O}$	— Heavy Water
HT	— Air tritium molecule
HTO	— Water tritium molecule
OBT	— Organic tritium molecule
$T_{1/2}$	— Half-life Time of a Radioactive Element
$\beta$	— Beta Decay
$\bar{\nu}_e$	— Electron Antineutrino
$e^-$	— Electron
$\gamma$	— Gamma
$\sigma$	— Cross Section of a radioactive process
$\eta_{det}$	— Intrinsic Detector Efficiency
$F_{sci}$	— Active surface of the Plastic Scintillator
$\varepsilon_{det}$	— Specific Detector Efficiency
mip	— Minimum Ionizing Particle
$Q_\beta$	— Energy released in a radioactive decay
S	— Specific Energy Lost
Z	— Atomic number
$E_\gamma = h\nu$	— Energy of a photon
$E_e$	— Energy of a electron
$m_0$	— Rest mass of a electron
c	— Speed of the light in the vacumm
$E_b$	— Binding Energy
$S_{ij}$	— Single states of energy levels of electrons in scintillator
$T_{ij}$	— Triple states of energy levels of electrons in scintillator

Units:

$\text{mSv/yr}$	— Millisievert per Year
$\text{mrem}$	— Millirem
$\text{STP}$	— Standard Temperature ( $0^\circ\text{C} = 273\text{K}$ ) and Pressure (1 atm)
$\text{W}$	— Watt
$\text{h}$	— Hour
$\text{g CO}_2/\text{kWh}$	— Grams of $\text{CO}_2$ per Kilowatt Hour
$\text{L}$	— Liter
$\text{Bq}$	— Becquerel, Nuclear Decay Number per Second
$\text{Bq/L}$	— Becquerel per Liter
$\text{Ci}$	— Curies
$\text{Ci/L}$	— Curies por Liter
$\text{yr}$	— Year
$\text{Ci/yr}$	— Curies per year
$\text{GW}$	— GigaWatt
$\mu\text{S/cm}$	— MicroSivers per Centimeter
$\text{kcps}$	— Kilo Counts per Second
$\text{pF}$	— picoFarads
$\text{A}$	— Ampere (C/s).
$\text{C}$	— Coulomb.
$V$	— Voltage.
$T$	— Temperature ( $^\circ\text{C}$ ).
$\text{Vol}$	— Volume ( $\text{m}^3$ ).

Añadir en un futuro:

$D\&D$	— Decontamination and Decommissioning.
$DWS$	— Drinking Water Standars
$NA$	— Numerical Apertures



# Contents

<b>Acknowledgements</b>	<b>III</b>
<b>Abstract</b>	<b>V</b>
<b>Nomenclature and acronyms</b>	<b>VII</b>
<b>List of Figures</b>	<b>XXVIII</b>
<b>List of Tables</b>	<b>XXXII</b>
<b>1 Introduction</b>	<b>1</b>
1.1 Tritium and Nuclear Energy . . . . .	1
1.2 Tritium Properties and Radiological Hazards . . . . .	9
1.3 Current Legislation . . . . .	17
1.4 This thesis . . . . .	20

<b>2 Tritium Detection Systems</b>	<b>21</b>
2.1 State-of-the-Art . . . . .	21
2.2 TRITIUM Project . . . . .	25
<b>3 TRITIUM Design Principles</b>	<b>29</b>
3.1 Detector System Overview . . . . .	29
3.2 TRITIUM Detector . . . . .	31
3.2.1 Interaction of Particles with Matter . . . . .	32
3.2.2 Plastic Scintillators . . . . .	36
3.2.3 Light Detection in Photosensors . . . . .	43
3.2.4 Electronic Readout . . . . .	55
3.3 Ultrapure Water System . . . . .	67
3.3.1 Introduction to the Water System . . . . .	67
3.3.2 Water System Set Up . . . . .	68
3.4 Background Rejection System . . . . .	70
3.4.1 Passive Shield (Lead) . . . . .	72
3.4.2 Active Shield (Cosmic Veto) . . . . .	74
<b>4 TRITIUM Detector R&amp;D</b>	<b>79</b>
4.1 Characetrization of the Scintillating Fibers . . . . .	80

4.1.1	Conditioning Process . . . . .	80
4.1.2	Automatic Polishing Machine . . . . .	84
4.1.3	Characterization of Scintillating Fibers . . . . .	89
4.1.4	Cleaning Process for Scintillating Fibers . . . . .	103
4.2	Characterization of the SiPM . . . . .	107
4.3	Characterization of the Ultrapure Water System . . . . .	107
4.4	Characterization of the Cosmic Veto . . . . .	110
<b>5</b>	<b>TRITIUM Monitor Prototypes</b>	<b>119</b>
5.1	Preliminary Prototypes . . . . .	120
5.1.1	TRITIUM-IFIC 0 . . . . .	120
5.1.2	TRITIUM-IFIC 1 . . . . .	124
5.2	Latest TRITIUM Prototypes . . . . .	128
5.2.1	TRITIUM-Aveiro 0 . . . . .	129
5.2.2	TRITIUM-IFIC 2 . . . . .	134
5.3	Modular TRITIUM Detector . . . . .	138
<b>6</b>	<b>Simulations</b>	<b>141</b>
6.1	Geant4 Environment . . . . .	141
6.2	Description of the Simulations Performed . . . . .	143

6.2.1	Tritiated Water Source . . . . .	143
6.2.2	Energy deposition and light output of scintillating fibers	144
6.2.3	Fiber Length . . . . .	145
6.2.4	Fiber Diameter . . . . .	146
6.2.5	Tritium-IFIC 2 . . . . .	147
6.2.6	Lead Shielding and Cosmic Veto . . . . .	149
<b>7</b>	<b>TRITIUM Monitor Results and Discussion</b>	<b>151</b>
7.1	Results from Laboratory measurements . . . . .	152
7.1.1	Experimental Results of TRITIUM-IFIC 0 . . . . .	152
7.1.2	Experimental Results of TRITIUM-IFIC 1 . . . . .	154
7.1.3	Experimental Results of TRITIUM-Aveiro 0 . . . . .	157
7.1.4	Experimental Results of TRITIUM-IFIC 2 . . . . .	164
7.2	Experimental Results in Arrocampo dam . . . . .	169
<b>8</b>	<b>Results of the TRITIUM Simulations</b>	<b>171</b>
8.1	Optimization of the TRITIUM Monitor Design . . . . .	172
8.1.1	Optimization of the Tritiated Water Source . . . . .	172
8.1.2	Simulation of the Output Light of Scintillating Fibers	174
8.1.3	Optimization of the Scintillating Fiber Length . . . . .	177

8.1.4	Optimization Scintillating Fiber Diameter . . . . .	179
8.1.5	Effect of the PMMA windows . . . . .	181
8.2	Simulation Results of TRITIUM monitor . . . . .	181
8.2.1	Simulation Results of TRITIUM-IFIC 2 . . . . .	183
8.2.2	Simulation Results of Background Rejection System .	189
<b>9</b>	<b>Conclusions and Prospects</b>	<b>191</b>
 <b>Appendices</b>		
<b>A</b>	<b>Electronical Schemes of PCBs Used for SiPM Characterization</b>	<b>197</b>
<b>B</b>	<b>Ultrapure Water System</b>	<b>199</b>
<b>C</b>	<b>Preparation of Liquid Radioactive Source of Tritium</b>	<b>203</b>
<b>D</b>	<b>Electronic System of TRITIUM-Aveiro 0 prototype</b>	<b>205</b>
<b>Bibliography</b>		<b>211</b>



# List of Figures

1.1	Annual average distribution of the radioactive dose received by the population [1] . . . . .	2
1.2	Networks of automatic and sampling stations managed by the spanish CSN. . . . .	5
1.3	Tritium sampling locations around Cofrentes NPP. . . . .	11
1.4	Tritium activity levels in surface water around Cofrentes NPP from January 2006 to November 2019. The white points are used for the detection limit and the green points are used for the measured activity, when it is above the detection limit. [9]	12
1.5	Tritium activity levels in groundwater around Cofrentes NPP from January 2006 to November 2019. [9] . . . . .	13
1.6	Tritium decay . . . . .	14
1.7	Energy spectrum of tritium electrons [31] . . . . .	15
2.1	Arrocampo dam, Almaraz NPP and Tajus river . . . . .	26
3.1	Scheme of the scintillator detector . . . . .	32

3.2	Domain regions of the three most probable types of interactions of gamma rays with matter. The lines show the values of Z and $h\nu$ where the two neighboring effects are equally likely. [76, 77]	34
3.3	Jablonsky diagram. [76]	37
3.4	Stokes shift. [76]	38
3.5	Emission spectrum of BCF-12 fibers of Saint-Gobain. [78]	41
3.6	How photons are collected in a fiber with single clad. [78]	42
3.7	Scheme of a PMT. [76]	45
3.8	Quantum efficiency spectrum for the PMT used (R8520-406). [81]	46
3.9	Hamamatsu commercial voltage divider electronic circuit. Upper circuit with negative supply and lower circuit with positive supply. [81]	48
3.10	Scheme of a APD and electrical symbol used. [84]	50
3.11	Using persistence on the oscilloscope to show several pulses with different heights. Each height associated with a different number of SiPM pixels lit at the same time.	51
3.12	(Left) Electronic scheme of a SiPM and (right) output current of a SiPM as a function of the reverse voltage. It show that the quenching mechanism is essential for working with SiPMs [89].	52
3.13	Electronic scheme of the electronic voltage divider circuit used for working with PMTs without its internal gain.).	56
3.14	Schemes of the different electronic for measuring with PMTs.	58

3.15 Different situation that can happen when time coincidences with PMTs are done. . . . .	61
3.16 Signal amplified and logical gate (input signals of MCA). . . . .	62
3.17 Different parts of PETSYS system. [103] . . . . .	63
3.18 Three PCBs used for the SiPM characterization and LED emission spectrum. . . . .	66
3.19 Scheme of water purification system. . . . .	68
3.20 Lead Bricks and their arrangement in the lead shielding. . . . .	73
3.21 Lead Bricks and their arrangement in the lead shielding. . . . .	73
3.22 Cosmic veto and Tritium-IFIC 2 prototype in an aluminum mechanical structure developed by IFIC's mechanical engineering department. . . . .	74
3.23 Hard cosmic events detected with the cosmic veto of TRI-TIUM: a) Affecting to the tritium measurement, b) Does not affecting to the tritium measurement. . . . .	75
3.24 Hard cosmic muon rate [111]. . . . .	76
3.25 Emission energy spectrum of the plastic scintillation used for the cosmic vetos. [112] . . . . .	77
3.26 Different layers used to cover of the cosmic veto. . . . .	78
4.1 Unsuccessful results of using commercial techniques to cut fibers. . . . .	82

4.2	Cutting device developed in the TRITIUM experiment and additional part to make precise measurements of fiber length.	82
4.3	Result of the polishing process. a) Fiber end after cutting b) Fiber end after cutting and polishing with Thorlabs technique.	84
4.4	Polishing machine developed in TRITIUM experiment. . . . .	85
4.5	Polishing table of the polishing machine . . . . .	86
4.6	Electronic system of Polishing machine. . . . .	88
4.7	Set up used to test the effect of the polishing machine. . . . .	89
4.8	Energy spectrums used to test the effect of the Polishing machine . . . . .	90
4.9	Set up used for fiber characterization. . . . .	92
4.10	Emission spectrum measured for the LED model 435-03 from Roithner LaserTechnik GmbH Company. . . . .	93
4.11	Difference between the results obtained in both tests carried out to check the light-tight quality of the system. . . . .	94
4.12	Response of the PMT as a function of its high voltage using the designed PCB with which no internal gain of the PMT is obtained. . . . .	95
4.13	Linearity tests of the PMT response . . . . .	96
4.14	Number of photons/ns reaching the PMT for Uncladded fibers.	100
4.15	Number of photons/ns reaching the PMT for ten samples of each fibers type. . . . .	101

4.16	Average of 10 samples for each fiber type (uncladded, single clad and multiclad fibers). . . . .	102
4.17	Wetting property produced by the cleaning process. [127] . .	104
4.18	Energy spectra obtained before and after the cleaning process	106
4.19	Reference points used for veto mapping. . . . .	111
4.20	Measurement of a radioactive source $^{137}\text{Cs}$ with the TRITIUM cosmic detector with and without its coverage. . . . .	112
4.21	Bidimensional graph of the count rate (Mapping) measured with two different TRITIUM cosmic detectors using a radioactive source of $^{60}\text{Co}$ . . . . .	113
4.22	Counting rate as a function of high voltage for fixed thresholds and as a function of thresholds for fixed high voltage. .	115
4.23	Energy spectrum measured with the cosmic veto. . . . .	116
4.24	Measurement of the cosmic veto for several distances between its cosmic detectors. . . . .	117
5.1	Bundle of 35 fibers, the length of which is 20 cm, used in TRITIUM-IFIC 0 prototype . . . . .	121
5.2	TRITIUM-IFIC 0 Prototype. . . . .	122
5.3	PMMA vessel used to check photon loss due to fiber bundle curve. . . . .	124
5.4	Teflon structure used to arrange the fibers of TRITIUM-IFIC 1 prototype in a matrix of 8 · 8. . . . .	125

5.5 Teflon vessel of TRITIUM-IFIC 1 prototype . . . . .	126
5.6 A general view of TRITIUM-IFIC 1 prototype . . . . .	127
5.7 TRITIUM-Aveiro prototype. . . . .	129
5.8 Teflon structure and fiber bundle used in TRITIUM-Aveiro 0 prototype. . . . .	129
5.9 Transmission spectrum of light (in the visible range) in a piece of PMMA of X thickness measured in the ICMOL lab- oratory. . . . .	131
5.10 Graphical User Interface developed to control the TRITIUM- Aveiro prototype. . . . .	133
5.11 TRITIUM-IFIC 2 prototype. . . . .	134
5.12 TRITIUM-IFIC 2 teflon vessel. . . . .	135
5.13 Graphical User Interface (GUI) of PETSYS. . . . .	137
5.14 A schematic design of the TRITIUM detector. . . . .	138
5.15 A TRITIUM detector design based on the TRITIUM-IFIC 2 prototype. . . . .	140
6.1 Distribution of the scintillating fibers in the simualtion of Tritium-IFIC 2 prototype. . . . .	147
6.2 Simualtion of Tritium-IFIC 2 prototype. PMTs (black), the optical grease (blue), PMMA windows (white), tritiated wa- ter (green) and scintillating fibers (yellow) . . . . .	148

7.1	Energy spectra experimentally measured with TRITIUM-IFIC 0 prototype. . . . .	153
7.2	Energy spectra experimentally measured with TRITIUM-IFIC 1 prototype. . . . .	155
7.3	The single-photon energy distribution of both PMTs used in the TRITIUM-Aveiro 0 prototype and their sum [151]. . . . .	158
7.4	Measurement of a $^{55}\text{Fe}$ radioactive source with the TRITIUM-Aveiro 0 prototype [151]. . . . .	159
7.5	Measurement of the background with TRITIUM-Aveiro 0 prototype covered with different thicknesses of lead [151]. . . . .	160
7.6	Measurements of the background and tritium liquid source (with an activity of 29.8 kBq/L) performed with the TRITIUM-Aveiro 0 prototype and integrated during a minute [151]. . . . .	162
7.7	Measurements of the background and tritium liquid source (with an activity of 29.8 kBq/L) performed with the TRITIUM-Aveiro 0 prototype and integrated during an hour [151]. . . . .	164
7.8	Energy spectra experimentally measured with TRITIUM-IFIC 2 prototype. . . . .	165
7.9	Tritium measurement with TRITIUM-IFIC 2 prototype and expressed in photons detected per event. . . . .	167
7.10	Monitoring of the signal and background prototypes for several months. . . . .	168
7.11	Background measured with the TRITIUM-Aveiro 0 prototype during its installation in Arrocampo dam [151]. . . . .	169

8.1 Energy distribution of a) simulated tritium decays b) Initial energy of tritium decays that reach the scintillating fibers (red histogram) compared the all simulated tritium events (blue histogram) [152]. . . . .	173
8.2 a)Transversal cut of simulated scintillating fiber (yellow) and tritium source (green) with various tritium decays (red dots) b) Distribution of the radial distance between the position where the tritium decay takes place and the surface of the scintillating fiber [152]. . . . .	174
8.3 Distribution of the initial energy of tritium events that has reach the scintillating fibers, blue histogram, and the energy deposited, red histogram [152]. . . . .	175
8.4 Energy distribution of photons produced by the scintillating fiber when the birks coefficient is not considered, red histogram, and when this is considered, blue histogram [152]. . . . .	176
8.5 Number of photons produced in front of the energy deposited in the scintillating fibers when a)the birks coeficient is not considered ( $k_B = 0$ ) b) the Birks coefficient is considered ( $k_B = 0.126 \text{ mm/MeV}$ ) [152]. . . . .	177
8.6 Number of photons produced in the fiber per tritium event for all tritium events that reach the fiber (blue histogram) and only for tritium events the photons of which are detected by photosensors (red histogram) [152]. . . . .	178
8.7 Counts integrated over 60 min, normalized to the same active area and taken over a week for a fiber length of 1 m, dashed lines, and 20 cm, solid lines and two different activities, 0.5 kBq/L, blue lines, and 2.5 kBq/L, red lines [152]. . . . .	179

8.8	Comparison of the energy deposition of cosmic ray events in scintillating fibers of 1 mm and 2 mm in diameter. . . . .	180
8.9	Distribution of photons reaching PMMA windows. The red histogram includes those guided by fibers and the blue histogram includes those traveling in the water medium [152]. . .	182
8.10	Tritium electron detected in the simulated TRITIUM-IFIC 2 prototype. The path of the optical photons is represented by green lines and the position in which it is absorbed is represented by red and blue dots (absorbed in water or PMT, respectively). .	183
8.11	Photons detected by both PMTs per tritium event in the simulated TRITIUM-IFIC 2 prototype. . . . . . . . . . . . . . .	184
8.12	Tritium counts detected with a simulated TRITIUM-IFIC 2 prototype using a integration counting time of 10 min a) as a function of the time b) distribution of them. . . . . . . . .	185
8.13	The distribution of the tritium counts detected with a simulated TRITIUM-IFIC 2 prototype for three different integration counting time, a)10 min b) 30 min and c) 60 min. . . . .	186
8.14	The distribution of the tritium counts detected with several simulated TRITIUM-IFIC 2 prototypes a) 1, b) 5 and c) 10 for an integration counting time of 10 min. . . . . . . . .	188
8.15	Resolution of the TRITIUM-IFIC 2 prototype as a function of the a) integration counting time b) number of prototypes.	189
B.1	Scheme of the ultrapure water system. . . . . . . . . .	199
B.2	Different stages of filtration of the ultrapure water system. . .	200

B.3 Doble phase reverse osmosis stage and containers used to store the outlet water of the ultrapure water system. . . . .	201
B.4 Siemens PLC, software for remote control of ultrapure water system. . . . .	201
B.5 General photo of the complete ultrapure water system. . . . .	202
B.6 Raw water, reject water and ultrapure water obtained with this system. . . . .	202
D.1 Electronic scheme of the PCB designed to power the PMTs of Aveiro prototype and the graphical user interface developed to control it. . . . .	206
D.2 Simplified electronic scheme used to process and analyze the signal of TRITIUM-Aveiro 0 prototype. . . . .	206
D.3 Graphical user interface used to manage the counter system. .	209
D.4 Two different situations of the electronic chain response. A.- Event accepted since veto has not detected it. B.- Event rejected since veto has detected it . . . . .	210

# List of Tables

1.1	Annual average distribution of the effective dose received by the population due to natural radioactive [2, 3]. . . . .	3
1.2	Emission of tritium per year from different types of nuclear reactors. Pressurized Water Reactor (PWR), Boiled Water Reactor (BWR), Heavy Water Reactor (HWR) and Gas-Cooled Reactor (GCR) [13] . . . . .	7
1.3	Most common nuclear reactions of artificial tritium production [13] . . . . .	10
1.4	Penetration depth for decay electron of mean (5, 7 keV) and maximum (18, 6 keV) energies in different media (tritium gas and air at standard conditions of temperature (273 K) and pressure (1 atm), STP, and water) [32] . . . . .	15
1.5	Legal limit of tritium in drinking water established in each country. . . . .	20

2.1	State-of-the-art in the tritium detection for different techniques. This table show the measured quantity, low detection level (LDL) and the sample form for four different techniques, liquid scintillator counting (LSC), ionization chamber (IC), calorimetry and beta induced X-rays spectrometry (BIXS) . . . . .	22
2.2	Results of different scintillator detector for tritiated water detection. This table shows the efficiency of the detector ( $\varepsilon_{det}$ ), its active surface ( $F_{sci}$ ), its specific efficiency ( $\eta_{det} = \varepsilon_{det}/F_{sci}$ ), defined as its efficiency normalized to its active surface, and its low detection-level (LDL) for each study listed above. . . . . . . . . . .	24
3.1	Critical angles asosciated to different interfaces created with polystyrene, $n_0 = 1.6$ , and other materials . . . . .	43
3.2	Properties of BCF-12 fibers from Saint-Gobain Inc. [78] . . . . .	44
3.3	Characteristics of SiPM S13360-6075 from Hamamatsu Photonics [86]. . . . . . . . .	53
3.4	Classification of natural radioactive series [107, 108]. . . . .	71
3.5	Properties of plastic scintillators from Epic-Crystals. [112] . .	77
4.1	Mean and standard deviation (due to fiber position in the setup) of photons per nanosecond that reach the PMT for 0.1 mA LED intensity. . . . . . . . . . .	97
4.2	Number of the collected photons versus LED intensity for 10 different samples of uncladded fibers. . . . . . . . . .	99
4.3	Number of the collected photons versus LED intensity for 10 different samples of single clad fibers. . . . . . . . . .	99

4.4 Number of the collected photons versus LED intensity for 10 different samples of multi clad fibers. . . . .	99
4.5 Relative standard deviations ( $\sigma_t$ , $\sigma_{pos}$ and $\sigma_{con}$ ) measured in this test. . . . .	100
4.6 Number of the collected photons versus LED intesntity for 10 different fibers of 10 cm length. . . . .	103
4.7 Collection efficiencies $CE_{10}$ and $CE_{100}$ . . . . .	103
4.8 Chemical components and turbidity measured in the raw wa- ter sample. . . . .	108
4.9 Measurements of the conductivity for several samples of water.	109
4.10 Measurements of the tritium activity for several samples of both, raw and pure water. . . . .	110
4.11 Count rate measured with two different cosmic detectors us- ing a radioactive source $^{60}\text{Co}$ . . . . .	114
8.1 Difference in activity that can be clearly distinguished for various cases of the TRITIUM-IFIC 2 prototype based on different integration counting times and different number of prototypes. . . . .	189

9.1 Results of different scintillator detector for tritiated water detection. This table shows the efficiency of the detector ( $\varepsilon_{det}$ ), its active surface ( $F_{sci}$ ), its specific efficiency ( $\eta_{det} = \varepsilon_{det}/F_{sci}$ ), defined as its efficiency normalized to its active surface, and its low detection-level (LDL) for each study listed above. The "*" symbol indicates that this is the specified activity that the detector can distinguish from the background, but it is not its LDL. . . . .	193
--	-----

# Chapter 1

## Introduction

### 1.1 Tritium and Nuclear Energy

Radioactivity has been present in the Universe since its inception. It was an important element of the Big Bang<sup>1</sup>, which occurred about  $14 \cdot 10^9$  years ago. It was also present during the formation of the earth,  $4.5 \cdot 10^9$  years ago, which explains why the different layers that make up the earth contain radioactive elements.

Therefore, humanity has been exposed to radioactivity since its origin, whether present in the Earth's crust or in the universe (external natural irradiation). Even the human being himself is radioactive as radioactive elements are contained in the human body such us  ${}^3\text{H}$ ,  ${}^{14}\text{C}$  or  ${}^{40}\text{K}$ , introduced into the body through food or water ingestion or air inhalation (internal natural irradiation). The annual average of the radioactive dose received by the population is presented in Figure 1.1 and Table 1.1.

---

<sup>1</sup>The Big Bang is the most acceptable hypothesis that explains the formation of the universe and its development over time so far.

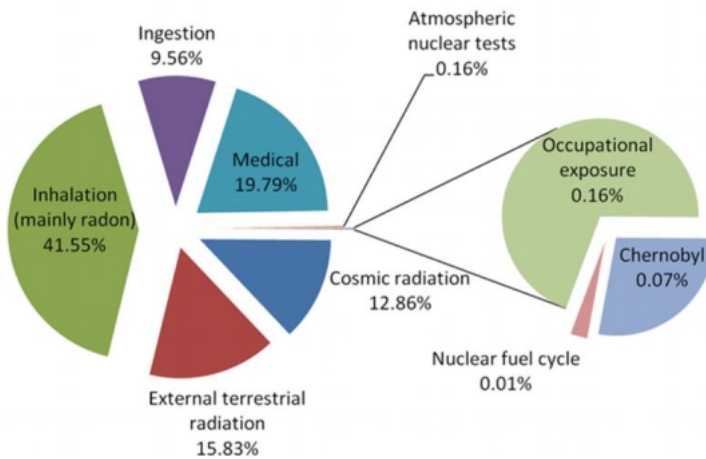


**Figura 1.1** – Annual average distribution of the radioactive dose received by the population [1]

As can be seen in Figure 1.1, most of the radioactive dose received by the population is due to both, internal and external natural radiatioactivity, called natural radiation, the effective dose<sup>2</sup> of which is estimated in 2.42 mSv/yr as can be seen in Table 1.1. It can also be appreciated in Figure 1.1 that the most important part of the artificial radiation received comes from medical treatments.

Since the discovery of radioactivity, made by Hènri Becquerel in 1896, a lot of technology based on nuclear concepts has been developed and applied to several fields such as energy production, research, medicine, industry, etc.

Due to the introduction of radioactivity in the society, various anthropogenic radioactive sources have appeared in the environment, resulting in increased levels of its radioactive elements, called radioactive background.

As our knowledge about radioactivity and our measurement tech-

---

<sup>2</sup>The effective dose is the radioactive dose absorbed by the population, taking into account the different radiosensitivity in each organ or tissue.

Radiation source	Eff. dose (mSv/yr)	Typical range (mSv/yr)
Cosmic (external)	0.39	0.3 – 1.0
terrestrial (external)	0.48	0.3 – 0.6
Inhalation (internal)	1.26	0.2 – 10
Ingestion(internal)	0.29	0.2 – 0.8
Total	2.42	1 – 12.4

Table 1.1: Annual average distribution of the effective dose received by the population due to natural radioactive [2, 3].

niques advanced, the negative effects of radioactivity was observed and characterized. Because of that, it is important to control the level of radioactive background to which the population is exposed and to ensure that these levels is kept below of a safe limit. For this task, several organizations were created to forward recommendations in radiological protection to the different organizations and governments of the world.

1. Firstly, a definition of concepts and units was necessary to quantify the negative effects of radioactivity and, for that, the International Commission of Radiological Units and Measurements, ICRU [4], was created during the first international conference of radiology held in London, in 1925.
2. Secondly, the International Commission on Radiological Protection, ICRP [5], was created in 1928 by the International Society of Radiology, ISR [6]. The ICRP aims to make recommendations and to provide guidance on different aspects of protection against radioactivity. The ICRP does not have the legal capacity to enforce its recommendations, but these are widely accepted the legislation of most countries.
3. Thirdly, the United Nations Scientific Committee on the Effects of Atomic Radiation, UNSCEAR [2], was created in 1955, the objective of which is to estimate and report the levels and effects of ionizing

radiation on the population and the environment. These estimates are taken into account by governments around the world to establish their limits and safety standards.

4. Fourthly, the International Atomic Energy Agency, IAEA [1], was created in 1957, which is though to promote the peaceful use of nuclear energy and to avoid its use for any military purpose such us nuclear weapons. Although it is an independent agency, it must to report to the United Nations, UN [7].
5. Fifthly, at the level of the European Union, EU, the European Atomic Energy Community, EURATOM, was created in 1957, which is a international organization established by the EURATOM treaty. Its objective is to coordinate research programs for the peaceful use of nuclear energy and the sharing of knowledge, infrastructure and financing of nuclear energy.
6. Finally, at the national level in Spain, the Nuclear Safety Council, CSN for its acronym in Spanish, was created in 1980 [3]. The CNS is the only institution in Spain in matter of nuclear safety and radiological protection and its objective is to reduce to the maximum the radioactivity in the environment due to anthropogenic origins.

For this task, the CSN has created a number of networks consisting of several detectors of radioactivity that are in charge of controlling the levels of radioactivity in the environment and checking the impact of radioactivity facilities to it. Two of the most important networks are the network of automatic stations and network of sampling stations:

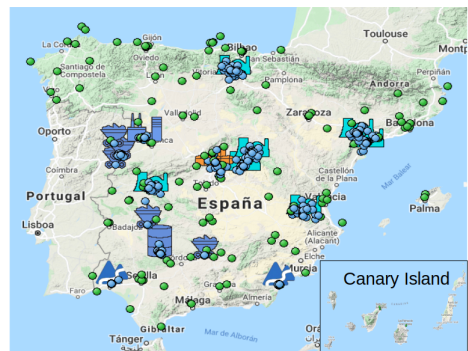
- (a) On the one hand, the network of automatic stations [8], REA for its acronym in Spanish, shown in Figure 1.2a, which consists of several gamma detectors<sup>3</sup> distributed in Spain that measure the radioactive dose in real time. The REA is used for the immediate

---

<sup>3</sup>Detectors that only measure gamma radioactivity



**(a)** Measured points of the REA [8]. The white box is the daily average of the gamma dose and the green box is the monthly average of the gamma dose.



**(b)** Measured points of the REM [9]. Blue dots are located around nuclear facilities. Green dots are uniformly distributed in Spain.

**Figura 1.2** – Networks of automatic and sampling stations managed by the spanish CSN.

detection of radiological problems and the application of quick response.

- (b) On the other hand, the network of sampling stations [9], REM for its acronym in Spanish, shown in Figure 1.2b, which consists of several interesting points in Spain where samples are taken and transported to a laboratory to be measured. About twenty Spanish laboratories are integrated into this network, the objective of which is to characterize the concentration and evolution of various radioisotopes present in the radioactive background of Spain and to quantify the impact of radioactive facilities on the environment.

There are other networks that measure different parameters such as the concentration of  $^{226}\text{Ra}$  in the air and the measurements of all the networks are adapted to the EUROTAM treaty [10].

The goal of this thesis and the *TRITIUM* project is to develop a monitor capable of automatically measuring low levels of tritium in water in quasi-real time<sup>4</sup>. This monitor is destined to be finally included in the REA.

Tritium is one of the radioactive isotopes routinely measured in REM tests and it is detected through the low-energy electrons produced in tritium beta decay, mainly through the liquid scintillation counter technique, LSC. Due to the limitations of the current methods, which will be shown in section 2.1, the objective of the *TRITIUM* project is to build a tritium detector based on scintillating fibers that will be put directly in contact with the sample (water). The photons produced in these scintillating fibers will be read out using photosensors, either photomultiplier tubes (PMTs) or silicon photomultipliers (SiPMs).

The *TRITIUM* collaboration is an international group consisting of a consortium of 6 different European institutions of 3 different countries: Portugal, France and Spain. The final emplacement of the *TRITIUM* monitor is the Arrocampo dam, Extremadura, Spain, the water of which is used for the cooling system of the Almaraz fission nuclear power plant, NPP. This detector will be installed 4 km downstream from the Almaraz Nuclear Power Plant.

The monitor will be used to ensure that the tritium levels of the Arrocampo dam water are below of the legal limit specified in the EURATOM treaty [10], which is 100 Bq/L. It will be used indirectly to verify the correct operation of the Almaraz NPP, located 4 km above the river since a malfunctioning of it will produce an increase of the tritium activity.

Tritium is one of the most abundantly produced radioisotope in a NPP, as it was verified in the United States Department of Energy complex,

---

<sup>4</sup>Quasi-real time is an approximation of real-time measurements. It means a relatively small time, like ten minutes.

(U.S. DOE) [11, 12] and in several research facilities in China [13] and places around them (ground water, surface water and process waste water).

Tritium is usually produced in the water used in the nuclear reactor cooling system of some NPPs. It is produced by neutron capture of deuterium, existing in the heavy water ( $D_2O$ ), semi-heavy water ( $HDO$ ) or the deuterium created by neutron capture in usual water ( $H_2O$ ). All these processes have a large probability to happen due to the huge neutron flux in the nuclear reactor, of the order of  $10^{14} \text{ n cm}^{-2}\text{s}^{-1}$  [14]. This tritium is finally released partially or totally to the environment with a quantity that depends on the reactor type as it is shown in Table 1.2. The most common way that tritium is released to the environment is HTO [13].

Reactor type	Gaseous discharge (GBq/y)	Liquid discharge (GBq/y)
PWR	$3.70 \cdot 10^3$	$2.59 \cdot 10^4$
BWR	$1.85 \cdot 10^3$	$3.70 \cdot 10^3$
HWR	$7.40 \cdot 10^5$	$1.85 \cdot 10^5$
GCR	$7.40 \cdot 10^3$	$1.11 \cdot 10^4$

Table 1.2: Emission of tritium per year from different types of nuclear reactors. Pressurized Water Reactor (PWR), Boiled Water Reactor (BWR), Heavy Water Reactor (HWR) and Gas-Cooled Reactor (GCR) [13]

NPPs are operational since more than 60 years and, nowadays, they are essential for providing a large part of the electric power used in the world (more than 20% in Spain [15]). Although the Spanish government is planning to progressively shut down all NPP there are other countries like China [16] or United States, USA [17], that promote their use.

On the one hand, NPPs are an interesting investment since it is one of the cheapest source of energy production. It is stable, as it doesn't depend on meteorological parameters and it doesn't emit greenhouse gases. Although there are other alternative energy sources which are being devel-

oped quickly (photovoltaic, wind, tidal energy, etc.), even other concepts of energy production and saving (local production, solar roofs, energy efficiency, smart cities, etc.), today they are not developed enough to fully cover the population needs. On the other hand, NPPs still have some problems such as the contamination of fresh water from uranium mining, the nuclear waste produced, the nuclear proliferation or the risk of radioactive contamination from accidents as happened in the past: Chernobyl, Fukushima and Three Mile Island [18].

In any case nuclear energy production in the world is not going to stop in the next decade, in fact, it will increase as the United States Energy Information Administration (U.S. EIA) expects [19]. Therefore the development of different types of alarm systems is a good investment. Safety is not a negotiable aspect and there must be mechanisms that warn us of any malfunction of a nuclear power plant.

In addition, it is important to highlight that the developed monitor could be used to verify the correct operation of a nuclear power plant, but it is not our objective. Our much broader objective is to ensure that the levels of tritium in the analyzed water are below the Spanish legal limit. It means that this monitor could be used in many different places with radioactive facilities like the future fusion power plants<sup>5</sup>, nuclear research facilities<sup>6</sup> or tracking the pathway of tritium discharges to ground water [22].

---

<sup>5</sup>The International Thermonuclear Experimental Reactor, ITER, will need up to several tens of kilograms of tritium to function, which correspond to various TBq of tritium.

<sup>6</sup>Tritium is one of the main emissions from these sites [20], [21].

## 1.2 Tritium Properties and Radiological Hazards

Tritium is the only radioactive isotope of hydrogen present in the environment. It was for the first time produced in 1934 from neutron capture of deuterium by Ernest Rutherford, Mark Oliphant and Paul Harteck [23] and it was first time isolated in 1939 by Luis Walter Alvarez and Robert Cornog [24], who checked that tritium is a radioactive element.

Tritium is naturally produced in the environment through the interaction of cosmic rays and gaseous elements of the upper atmosphere like nitrogen ( $^{14}\text{N}(\text{n}, ^3\text{H}) ^{12}\text{C}$ ) [25] and oxygen ( $^{16}\text{O}(\text{n}, ^3\text{H}) ^{14}\text{N}$ ) [26]. Around 99% of cosmogenic tritium forms water (HTO) and reaches the Earth's surface as rain with an estimated production rate of  $4 \cdot 10^6 \text{ Ci/yr}$  ( $1.48 \cdot 10^8 \text{ GBq/yr}$ ), producing a tritium concentration of  $0.6 - 1.2 \text{ Bq/L}$  in precipitation [13, 25].

Tritium can be produced artificially in the environment from different anthropogenic sources [13, 25]. There is a large amount of tritium which was produced in military nuclear test explosions between 1945 and 1975, with an estimated total production of  $8 \cdot 10^9 \text{ Ci}$  ( $2.96 \cdot 10^{11} \text{ GBq}$ ) and a part of which remains to the date. In these nuclear explosions, tritium was produced mainly from the nuclear reactions  $^{14}\text{N}(\text{n}, ^3\text{H}) ^{12}\text{C}$  and  $^2\text{H}(\text{n}, \gamma) ^3\text{H}$ . Tritium can also be produced by commercial producers of radioluminescent and neutron generator devices ( $1 \cdot 10^6 \text{ Ci/yr}$ ), nuclear power and defense industries (around  $2 \cdot 10^6 \text{ Ci/yr}$ ) and several research facilities and nuclear reactor for energy production ( $2 \cdot 10^6 \text{ Ci/GWyr}$ ), through the production cross sections shown in Table 1.3:

Tritium levels in the environment excluding anthropogenic radioactive sources are between 1 and 4 Bq/L, larger than the expected due to the cosmogenic background levels ( $0.6 - 1.2 \text{ Bq/L}$ , previously mentioned) [27]. It can be explained by the consequences of nuclear weapons tests.

Source	Origin	Nuclear reaction	Cross section (b)
$^2_1\text{H}$	Water coolant	$^2_1\text{H}(\text{n}, \gamma)^3_1\text{H}$	$5.2 \cdot 10^{-4}$
$^3_2\text{He}$	Helium coolant	$^3_2\text{He}(\text{n}, \text{p})^3_1\text{H}$	5330
$^6_3\text{Li}$	Moderator	$^6_3\text{Li}(\text{n}, \alpha)^3_1\text{H}$	940
$^{10}_5\text{B}$	Moderator, control rods	$^{10}_5\text{B}(\text{n}, 2\alpha)^3_1\text{H}$	3835

Table 1.3: Most common nuclear reactions of artificial tritium production [13]

Tritium levels in rivers around a nuclear facility are between 1 and 10 Bq/L and even between 20 and 50 Bq/L at the water discharge site of NPPs [27], where the produced tritium is partially or totally released into the environment, mainly in the HTO water form.

The effect of NPP on tritium levels can be observed from REM date, for example the case of Cofrentes. Cofrentes is the closest nuclear power plant to Valencia, in the measurements of which are involved the LARAM<sup>7</sup>. There, the tritium level is measured in three different places along the Jucar river, marked on the map shown in Figure 1.3. The first place, P1, is located in the river, 6 km upstream from the NPP, the second place, P2, is located 1 km downstream and the third place, P3, is located 5 km downstream. The level of tritium measured in these three locations is shown as a function of the time in Figures 1.4a, 1.4b and 1.4c respectively.

In these figures, the detection limit and the measured activity are shown using white and green dots, respectively. The measured activity is only displayed when it is larger than the corresponding detection limit. The tritium level in the river increases due to the discharge of the NPP and it is diluted again after 4 km downstream, as can be seen from these date.

Two additional measurements of the tritium level in groundwater

---

<sup>7</sup>The LARAM is a Valencia laboratory specialized in environmental radioactivity measurements



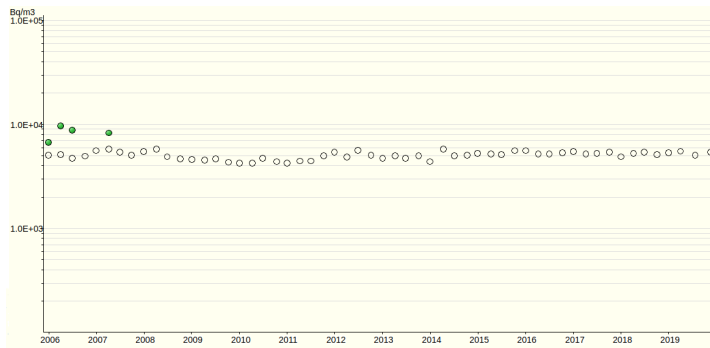
**Figura 1.3** – Tritium sampling locations around Cofrentes NPP.

have been included, points S1 and S2 on the map in Figure 1.3, which are located 1 km before and 1 km after the NPP. Both tritium levels are shown in the figure 1.5a and 1.5b respectively, where it can be observed that they are not affected by the nuclear power plant.

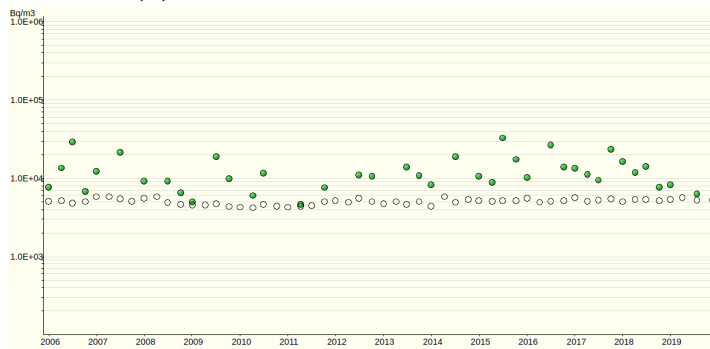
It is important to note that, although environmental tritium level is affected by NPP, these levels are below the maximum allowed limit. The maximum level of tritium measured since of January 2, 2006 is around 32 Bq/L, below to the maximum allowed limit in Europe, 100 Bq/L.

Tritium is a radioactive element with a half-life time of  $T_{1/2} = 12.32$  years. It has one proton and two neutrons and decays exclusively through  $\beta$  radiation. It decay 100% directly to the ground state of the  $^3_2\text{He}$  isotope of helium, which is a stable nuclei, thorough the decay scheme of equation 1.1:

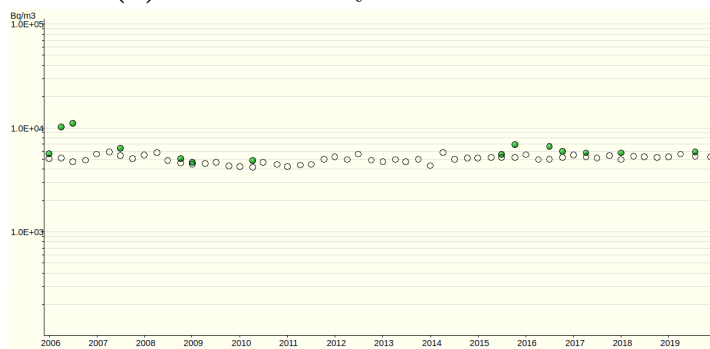




(a) Tritium activity 6 km upstream.

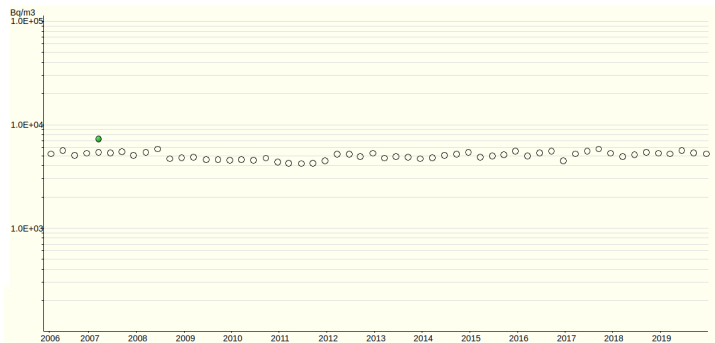


(b) Tritium activity 1 km downstream.



(c) Tritium activity 5 km downstream.

**Figura 1.4** – Tritium activity levels in surface water around Cofrentes NPP from January 2006 to November 2019. The white points are used for the detection limit and the green points are used for the measured activity, when it is above the detection limit. [9]

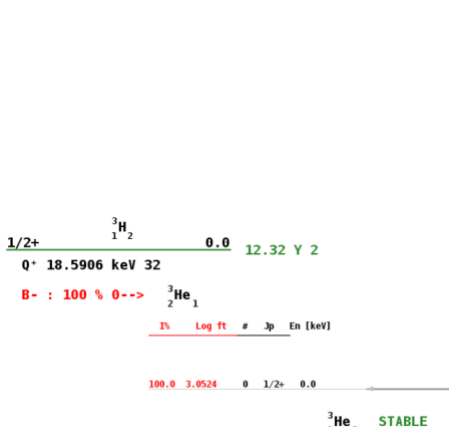


(a) Tritium activity 1 km before NPP.

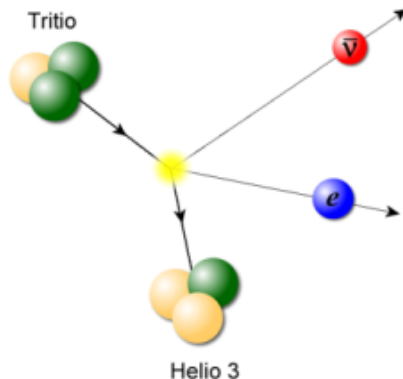


(b) Tritium activity 1 km after NPP.

**Figura 1.5** – Tritium activity levels in groundwater around Cofrentes NPP from January 2006 to November 2019. [9]



(a) Tritium energy levels. [29]



(b) Graphic representation of tritium decay [30].

**Figura 1.6 – Tritium decay**

In Figure 1.6 the scheme of tritium energy levels is shown. In this decay it is not possible to detect the neutrino because of its extremely weak interaction with matter ( $\sigma \propto 10^{-42} \text{ cm}^2$  [28]) and, since  ${}^3\text{He}$  has a much larger mass than electrons and neutrinos, by conservation of energy and momentum, the energy that is taken by this daughter nucleus is very small. Therefore, the detection of tritium is through its decay electron.

The energy released in the tritium decay is  $Q_\beta = 18.6 \text{ keV}$ , shared between the decay products. Therefore, the energy spectrum of the decay electrons is a continuum with a maximum value of 18.6 keV, as shown in Figure 1.7. This energy spectrum has an average energy of 5.7 keV and the most likely energy is slightly below, around 4.5 keV.

The releasing energy of the tritium decay, is very low. In fact, it is the radioactive isotope with the lowest energy released in its  $\beta$  disintegration [25]. Consequently, the  $\beta$  particle which is emitted in this tritium decay will have a very small mean free path, shown in Table 1.4.

This short mean free path is a major issue in tritium detection, as

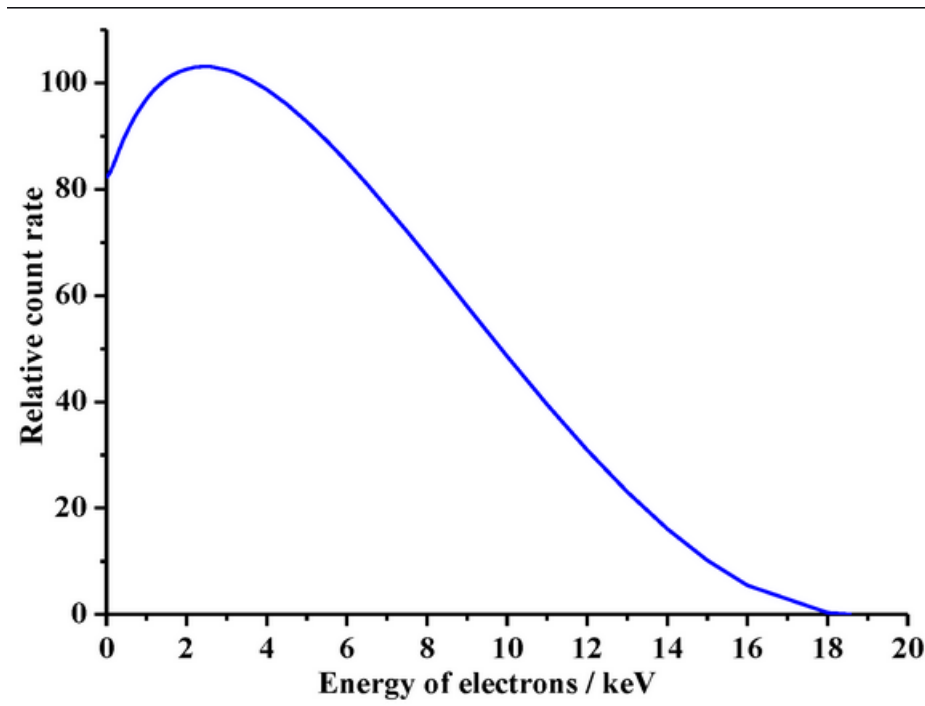


**Figura 1.7** – Energy spectrum of tritium electrons [31]

Material	P. Depth (5.7 keV)	P. Depth (18.6 keV)
${}^3_1\text{H}_2$	0.26 cm	3.2 cm
Air	0.036 cm	0.45 cm
Water, soft tissue (solid matter with a density of $1 \text{ g} \cdot \text{cm}^{-3}$ )	$0.42 \mu\text{m}$	$5.2 \mu\text{m}$

Table 1.4: Penetration depth for decay electron of mean (5, 7 keV) and maximum (18, 6 keV) energies in different media (tritium gas and air at standard conditions of temperature (273 K) and pressure (1 atm), STP, and water) [32]

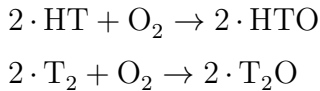
it makes more difficult the electron detection, which will require a highly sensitive detector. It means that tritium electrons have a low penetration in our body and they are easily stopped with clothes or laboratory gloves, resulting in a low radiological hazard of external tritium.

Nevertheless, the danger of tritium increases when it is ingested or inhaled since it can bind anywhere that hydrogen can and perform the same chemical reactions, sometimes with higher rate if the tritium concentration is high enough to catalyze the reaction.

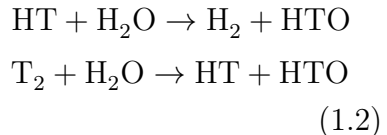
Tritium can be absorbed in our body in three different ways, gaseous tritium (mainly HT), tritiated water (mainly HTO) and organically bound tritium (called OBT).

- The gaseous tritium, which is normally found mixed in the air, is the least important since less than a  $3 - 5 \cdot 10^{-3} \%$  is absorbed by the human body, which is insignificant [25]. However, it can be transformed into tritiated water, more harmful from a radiobiological point of interest [25], through the oxidation and exchange reactions by equations 1.2:

*Oxidation :*



*Exchange*



- Tritiated water, which is normally found in drinking water and food, has a larger impact since the 99% of it is absorbed [25]. Its biological life time corresponds to the water cycle in the body, around 9.5 days ( $\pm 50\%$ ), time during which tritium will remain in our body [25, 27, 33]. As in water, the biological life time of tritiated water can vary

due to various external parameters such as temperature, humidity, drinking habits, etc. or reduced with the use of diuretics [25].

- Organically bound tritium, normally found in food, generally forms a covalent bond with a carbon and it corresponds to 5 – 10 % of tritium absorbed in the body. Although it is less absorbed in the body than tritiated water, it can be more dangerous since it has a longer biological life time. The biological life time of this tritium type depends on the affinity of the organic molecule to the different biological tissues and it can vary from tens to hundreds of days (larger than the ICRP estimate) [27, 33, 34, 35].

There are many studies showing that tritium in living matter can cause the same effects than X-rays or  $\gamma$  rays, which are mutations, tumors, cancer, genetic effects, reproductive effects, etc [36, 37]. In fact, the consequences of tritium radiation can be worse than a similar  $\gamma$  radiations since its biological efficiency<sup>8</sup> is two or three times larger [36].

In summary, tritium is a naturally occurring radioactive element that can affect health if it is released excessively. Because of that, each country has developed a legislation, shown in section 1.3, to manage the release of tritium and ensure that these background levels are safe for health.

## 1.3 Current Legislation

Due to the radiological risk of tritium, which was deal with in section 1.2, it is important that the current legislation limits the release of tritium to the environment ensuring that the levels are below a safe value for health.

---

<sup>8</sup>The biological efficiency is used to quantify the damage produced in the living cells due to an external radiation.

The guidelines setting impose the limit of radioactive elements in drinking water for many countries are based on the radiation protection methodology developed by the ICRP [38] and the recommendations of the world health organization (WHO) [39].

The objective of the international radiation methodology is to protect people and the environment from the negative effects of ionizing radiations but allowing beneficial activities that involve a reasonable radiation exposure. It is based on three main points, which are the justification (the benefit from radiological exposure must outweigh the detriment to health that it causes), the ALARA principle, "As Low As Reasonably Achievable" (the radiological exposure must be kept as low as possible considering social and economic factors) and dose limitation (limit that must never be exceeded).

While the ICRP recommends a maximum dose of 1 mSv/yr, excluding the natural background and medical interventions, the WHO is more conservative, recommending a maximum dose of 0.1 mSv/yr, which correspond to less than 5% of the annual dose due to background radiation, 2.42 mSv/year, Table 1.1.

The guideline reference level of each radionuclide in drinking water, GL, is usually calculated from these recommendations using the equation

$$GL = \frac{RDL}{DCF \cdot q} \quad (1.3)$$

where RDL is the reference dose level, DCF is the dose conversion factor (the normal used value for tritium is  $1.810^{-11}$  SvBq, provided by ICRP [40]) and q is an estimation of the annual volume of drinking water consumed (normally assumed two liters per day, 730 L/yr).

The GLD calculated for tritium in drinking water according to the ICRP and WHO recommendations is 76,103 Bq/L and 7,610 Bq/L

respectively. It means that tritiated water with activities below these values is considered not harmful to health.

Based on these recommendations, each country has created organizations in charge of developing its own legislation on radionuclide limits. In Spain, the responsible organization of this task is the CSN.

Most of the countries in the world implement the RDL of 0.1 mSv/yr recommended by the WHO. The legal limit for tritium in drinking water in this case is 76,103 Bq/L but it is often approximated in different ways. Some countries like Switzerland [41] or some organizations like the WHO [39] rounded this value to 10,000 Bq/L. Others like some countries of Canada, such as Ontario and Québec, truncate this value to the first number 7,000 Bq/L [42, 43]. There are other countries like Russia which use the much more accurate approximation value of 7,700 Bq/L [44].

There are other countries like Australia that prefer to implement the RDL of 1 mSv/yr, recommended by the ICRP, the legal limit of which is 76,103 Bq/L [45]. Other countries like Finland are based in the ICRP recommendations and use only the middle of this value, 0.5 mSv/yr, the value of which is rounded to a legal limit of 30,000 Bq/L for tritium in drinking water [46].

There are two different exceptions to these recommendations:

1. On the one hand, most of the USA states like California use a RDL of 4 mrem (0.04 mSv), which corresponds to a legal limit of 20 nCi/L (740 Bq/L) [47]. This value was proposed by the United States Environmental Protection Agency (US EPA) as a result of an analysis of the available information [48].
2. On the other hand, most of the EU countries, such as France, Germany or Spain, impose an GL of 100 Bq/L, which is one of the most restrictive limit in the world [49, 50, 51]. This value arise from the

consideration that it is an indicator of the presence of other radionuclides more dangerous than tritium. These limits are fixed by the EURATOM Council Directive [52].

All limits mentioned in this section are summarized in table 1.5.

Country/Agency	Legal limit of tritium (Bq/L)
ICRP	76,103
WHO	10,000
Switzerland	10,000
Canada	7,000
Russia	7,700
Australia	76,103
Finland	30,000
United States	740
European Union	100

Table 1.5: Legal limit of tritium in drinking water established in each country.

## 1.4 This thesis

# Chapter 2

## Tritium Detection Systems

### 2.1 State-of-the-Art

Measurement of tritium activity is one of the routine environmental controls that are carried out in the vicinity of nuclear research facilities and nuclear power plants during their energy production lifetime. Consequently, this measurement has been carried out with different available technologies under development to improve the state of the art of tritium detection. The most employed techniques are summarized in Table 2.1.

Nowadays, the most used technique for measuring tritium in water is liquid scintillator counting (LSC). This technique consists of mixing a liquid sample (some ml for environmental measurements or less for higher activities) with liquid scintillator. This mixture is usually made in a ratio of 50:50 but it depends on the detection system and the samples used [53, 54]. In this technique, the  $\beta$  energy emitted from the sample excites the molecular energy levels of the liquid scintillator which promptly decays emitting several photons with a well-known energy (fluorescence), usually in the visible spectrum. Finally these photons are detected with photosen-

	LSC	IC	Calorimetry	BIXS
Measured quantity	Scintillation photons	Ionization current	heat	X-rays
LDL	$\sim$ Bq	10 – 100 kBq	$\sim$ GBq	$\sim$ MBq
Sample form	Liquid	Gas, vapor	All	All

Table 2.1: State-of-the-art in the tritium detection for different techniques. This table show the measured quantity, low detection level (LDL) and the sample form for four different techniques, liquid scintillator counting (LSC), ionization chamber (IC), calorimetry and beta induced X-rays spectrometry (BIXS)

sors, which convert the optical signal into measurable electrical charge. The liquid scintillator technique has a very good detection sensitivity for low activity levels of tritiated water ( $< 1 \text{ Bq/L}$ ) [55] but it has the problems of long measurement time (up to 2 days) and of producing chemical waste, as liquid scintillator contains toluene which is toxic. In addition, this technique requires special staff for sampling, chain-of-custody and lab analysis which require economical and time resources. In order to avoid this problem some unsuccessful efforts have been made in order to build a monitor of tritium with LSC [56].

The ionization chamber (IC) consists of a gas chamber (sample) which contains electrodes connected to different voltages. These electrodes collect the ionization current that is produced due to the  $\beta$  radiation. It is a simple and fast system, but it has the problem of high Low Detection Limit ( $> 10 \text{ kBq}$ ) and of requiring the samples to be in a state of gas or steam [57, 58].

The calorimetry method is based on the measurement of the heat generated in the detection medium (normally platinum) [59, 60]. The problem with this technique is that it has a high LDL, of the order of GBq, and requires long measurement time, 2 days or more.

The Beta Induced X-ray Spectrometry (BIXS) is based on the measurement of the bremsstrahlung radiation produced by the tritium decay electrons, using a NaI(Tl) crystal couplet to a PMT [61, 62] or Silicon Drift Detector (SDD) [63]. The problem with this technique is a high LDL, of the order of MBq.

There are additional methods for tritium detection, although they are less employed or less experimentally developed, each one with its own advantages and limitations. For example, the Avalanche PhotoDiode (APD) cannot be used in contact with water [64], the mass spectrometry which needs to store the sample several months before taking the measurement [65] and the Cavity ring spectroscopy requires a special optical configuration that is not possible outside a laboratory [66].

All the above techniques are offline methods that need long time for sample collection, shipment to the laboratory and activities measurements. Therefore, they cannot be used for in-situ monitoring of tritium in water. The liquid scintillation technique is the only one with sufficiently small Low-Detection-Limit to fulfill the compliance of 100 Bq/L in tritium of the water samples, established by the EURATOM directive.

The purpose of the TRITIUM project is to develop an alternative method, based on solid scintillators, that allows to accomplish the requirements of in-situ monitoring of levels as low as the legal limit in Europe 100 Bq/L in quasi-real time. There are several studies that have developed with solid scintillators so far:

1. The study done by M. Muramatsu, A. Koyano and N. Tokunaga in 1967 who used a scintillator plate read out by two PMTs in coincidence [67].
2. The study carried out by the A. A. Moghissi, H. L. Kelley, C. R. Phillips and J. E. Regnier in 1969 that used one hundred plastic fibers

coated with anthracene powder and read out by two PMTs in coincidence [68].

3. The study performed by R. V. Osborne in 1969 that used sixty stacked scintillator plates read out by two PMTs in coincidences [69].
4. The study done by A. N. Singh, M. Ratnakaran and K. G. Vohra in 1985, that used a scintillator sponge read out by PMTs in electronic coincidence [70, 71].
5. The study carried out by K. J. Hofstetter and H. T. Wilson in 1991, that tested different shapes of scintillator plastics like several sizes of beads, fibers, etc. The better result obtained for solid plastic scintillator was a tritium detection efficiency of the order of  $10^{-3}$  [72, 73].

Study	$\varepsilon_{det}(\frac{cps \cdot 10^{-3}}{kBq/L})$	$F_{sci}$ (cm <sup>2</sup> )	$\eta_{det}(\frac{cps \cdot 10^{-6}}{kBq/L \cdot cm^2})$	LDL (kBq/L)
Muramatsu	0.39	123	3.13	370
Moghissi	4.50	> 424.1	< 10.6	37
Osborne	12	3000	4	37
Singh	41	3000	13.7	< 37
Hofstetter	2.22	~ 100	< 22.2	25

Table 2.2: Results of different scintillator detector for tritiated water detection. This table shows the efficiency of the detector ( $\varepsilon_{det}$ ), its active surface ( $F_{sci}$ ), its specific efficiency ( $\eta_{det} = \varepsilon_{det}/F_{sci}$ ), defined as its efficiency normalized to its active surface, and its low detection-level (LDL) for each study listed above.

The results of these experiments are summarized in Table 2.2. As can be seen, in the first column that the intrinsic detector efficiency,  $\varepsilon_{det}$ , is very different in these experiments. As one of the most important factor that affect the efficiency is the active surface of the plastic scintillator,  $F_{sci}$ , which varies largely with the detector type, the specific detector efficiency (third column) is used in order to compare these experiments, that is, the intrinsic

detector efficiency normalized to this active surface. It can be checked that, effectively, these specific efficiencies are quite similar. The specific efficiency obtained by Moghissi for scintillating fibers is sufficiently high to justify our choice of scintillating fibers as a detection medium. Finally, as can be seen in the last column, the LDL in all these experiments are of the order of a few tens of kBq/L. Thus, to develop a detector which much lower LDL is essential to comply with the EURATOM directive of 100 Bq/L of tritium in water for human consumption.

## 2.2 TRITIUM Project

As a conclusion of section 2.1, the current techniques cannot be used for tritium monitoring in quasi-real time since they have either a higher LDL or they work in off-line method (too slow).

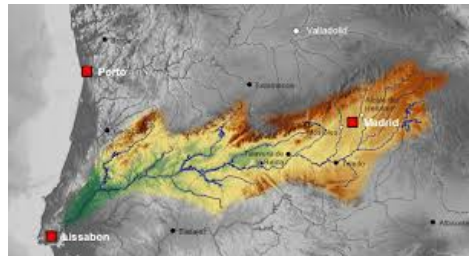
To overcome these limitations the *Tritium* project [74], with the title of "Design, construction and commissioning of automatic stations for quasi-real time monitoring of low radioactive levels of tritium in water", was proposed.

The *Tritium* collaboration is a international group consisting of a consortium of 6 different european institution of 3 different countries: The University of Aveiro, in Portugal, The University of Bordeaux and the National Center for Scientific Research, CNRS (Section Aquitaine-Limousin), in France and the University of Extremadura, *Junta de Extremadura* and University of Valencia, in Spain.

This project was funded by the Interreg Sudoe program of the European Economical Community, EEC, in the 2016 call with the reference number SOE1/P4/EO214. The purpose of this project is the development of a tritium monitor in quasi-real time. This monitor consists of a ultra-



**(a)** Arrocampo dam and Almaraz Nuclear Power Plant.



**(b)** Tajus river along Spain and Portugal.

**Figura 2.1** – Arrocampo dam, Almaraz NPP and Tajus river

pure water system, which prepare the water sample before introducing it in the detector for tritium measurement, a cosmic veto and a passive shielding, which reduce the natural background of our tritium detector, and several electronic modules which control all the different parts of the monitor, analyze the tritium measurement and send an alarm if the configured limit (100 Bq/L) is exceeded.

A crucial problem is to distinguish tritium signals from the background because tritium events has low energy ( $\sim$  keV) and fall in an energy range of the spectrum where there is significant background. To reduce the background counts of TRITIUM monitor, coincidence techniques are used.

The TRITIUM monitor will be installed in the Arrocampo dam, Almaraz, Spain, where the Almaraz NPP release the water of the secondary cooling circuit, displayed in Figure 2.1. This NPP has two nuclear reactors of PWR type. Arrocampo dam is located near the Tagus river, shown in Figure 2.1b, which is the longest river in Spain, with a long of the 1007 km. This river, shown in Figure 2.1a, rises in Aragon (Spain) and flows into the Atlantic Ocean, Lisbon (Portugal). The water of this river is used for agriculture and drinking water by both, Spanish and Portuguese people. Therefore the international cooperation in order to maintain the quality of the tajus river water is very important.

Each institution has concentrated its efforts in the development of a different part of this project:

1. The Extremadura group has developed and installed the ultrapure water system to produce water with very low conductivity,  $\sigma \approx 10 \mu\text{Sv}/\text{cm}$  (two orders less than sample before the cleaning process,  $1000 \mu\text{Sv}/\text{cm}$ ). This cleaning process is very important for two reasons. On the one hand, for maintaining our detector very clean, which is a critical point. On the other hand, to reduce the natural background since several natural radioactive isotopes presents in this water (except tritium) are removed such as  $^{222}\text{Rn}$ ,  $^{40}\text{K}$  or  $^{137}\text{Cs}$ . This system is explained in section 3.3.
2. The french group has develop the pasive shielding for the detector. The shielding is made of ultra radiopure lead with very low intrinsic activity in order to reduce the external natural background of the system. This shielding is presented in section 3.4.1.
3. The Portuguese and Spanish group have collaborated for designing, developing and building four different prototypes of tritium detector and active vetos for removing cosmic events. These prototypes and vetos are explained in chapter 5 and section 3.4.2 respectively.
4. The Portugal and Spanish people have also carried out simulations of this system. The environment chosen to develop these simulations is the package GEANT4 [75], consisting of an extensive C++ library with which the geometry of our detector, the relevant physical processes, etc. can be designed. This simulation are explained in chapter 6.

The important characteristics of the TRITIUM detector must have:

- *Compact.* This is an important point because in the place where this detector will be installed the useful space to be used is very limited.

- *Thin active volume and large active area.* On the one hand, it have to be taken into account that the mean free path of the  $\beta$  particle of tritium decay is very low so thin detector active volumes are needed. In practice, active thickness beyond the mean free path of the tritium electrons will only contribute to background. On the other hand, as explained in section 2.1, the efficiency of this type of detector scales with the active area, so it is crucial to design the detector with the largest possible active area.
- *High efficiency to tritium.* As the tritium activities to be measured are very low, it is very important to reduce as much as possible the non-detected tritium events.
- *High specificity to tritium.* The detector has to be able to distinguish the tritium signal from the signal due to other radioactive elements present in the sample.
- *Quasi-real time response.* It is important that the sistem work in quasi-real time in order to detect any problem as fast as possible.
- *Rugged system.* Finally, it has to be take into account that the final goal is to install an automatical system which work during a number of years without requiring the intervention of specialized people, which requires a rugged monitor.

In order to get the measurement in quasi-real time it is needed to work *in situ*, that is, in the same place that the water sample is taken. Working *in situ* has some benefits for the detector such as faster and cheaper maintenance since the sampling process, chain of custody, etc. are eliminated, more frequent measurements are carried out and safer monitoring since personal exposure dose is reduced, changes in activity levels can be detected quickly and possible errors due to specialized staff are eliminated.

# Chapter 3

## Design Principles of the Tritium Monitor

### 3.1 Detector System Overview

The objective of the TRITIUM project is the design, development, construction and commissioning of an automatic station for real-time monitoring of low levels of tritium in water. To achieve this aim, the TRITIUM group has developed a monitor consisting of several parts, listed below:

1. The TRITIUM detector, described in chapter 5, is based on several modules read in parallel. Each module consists of hundreds of scintillating fibers, section 3.2.2, which are in contact with the water sample measured, read by two coincident photosensors, section 3.2.3. The photosensors are photomultiplier tubes (PMT) (section 3.2.3) and silicon photomultipliers (SiPM) (section 3.2.3).
2. The ultrapure water system (section 3.3) that prepares the water sample before measurement. This system removes all the organic parti-

cles dissolved and all the particles with a diameter greater than  $1 \mu\text{m}$  without affecting the tritium content of the sample. This system is important for two reasons: First, because the mean free path of tritium in water is very short,  $5$  or  $6 \mu\text{m}$ , so it is essential to avoid the deposition of particles onto the fibers because this would prevent the tritium decay electrons from reaching the fibers. Second, particles dissolved in water may contain radioactive isotopes like  $^{40}\text{K}$ , which would increase the background. As the water sample has very low tritium counters, to reduce the background is a crucial matter.

3. The background rejection system (section 3.4), that has two different parts. The first one is a passive shield (section 3.4.1), consisting of a lead castle inside of which the TRITIUM detector is located. This castle is employed to eliminate natural radioactive background and cosmic rays with energies of the order of  $200 \text{ MeV/nucleon}$ . The second part is an active veto (section 3.4.2), consisting of two plastic scintillation blocks located inside of a passive shielding, above and below the TRITIUM detector and read by several photosensors. The goal of this active veto is to remove the remaining high energy events ( $> 200 \text{ MeV}$ ) cosmic rays that can travel through the passive shielding and contribute to background. Contrary to low energy cosmic rays, high energy cosmic rays are difficult to be stopped. The technique employed to eliminate their contribution consists of reading the TRITIUM detector in anti-coincidence with the active veto.
4. A monitoring electronic system sends an alarm if the signal limit of the tritium level,  $100 \text{ Bq/s}$ , is exceeded.

The different parts of TRITIUM monitor were subjected to tests to verify their correct operation before installing them in the Arrocampo dam. The final goal is to include TRITIUM in the network of automatic stations, REA (section 1.1).

## 3.2 TRITIUM Detector

As discussed in section 2.1, the TRITIUM consists in a chain of three main elements:

- The scintillator, that detects the tritium event, as ionizing radiation hits this material and deposits kinetic energy through ionization and excitation processes, part of the absorbed energy is converted in to photons, mostly in the visible range<sup>1</sup>. The produced photons carry information about the particle detected, like its energy, type, etc.
- The photosensor, that detects the photons produced in the scintillator. The most common photosensors in nuclear physics are PMTs and SiPMs. They detect the photons produced in the scintillator with an efficiency and transforms them in electrons with a multiplication factor of around  $10^6$ . These electrons form a electronic pulse than gives information of the detected photons.
- The electronic system, which is the part of the scintillator detector in charge of processesing and analyzing (first analogically and then digitally) the electrical pulse given by the photosensor. The output of the electronic system is the useful information about the events detected such as number and energy spectrum.

In Figure 3.1 a scheme of a scintillation detector is shown. There, the scintillator detects ionizing radiation and produces photons that are guided by the reflector and the light guide to the photosensor. Some of the photons that reach the sensitive part of the photosensors are converted and multiplied, forming a electronic pulse. The output signal of the photosensor (electronic pulse) is processed and analyzed by the corresponding electronics:

---

<sup>1</sup>The visible range is made up by photons with a wavelength between 380 nm and 750 nm

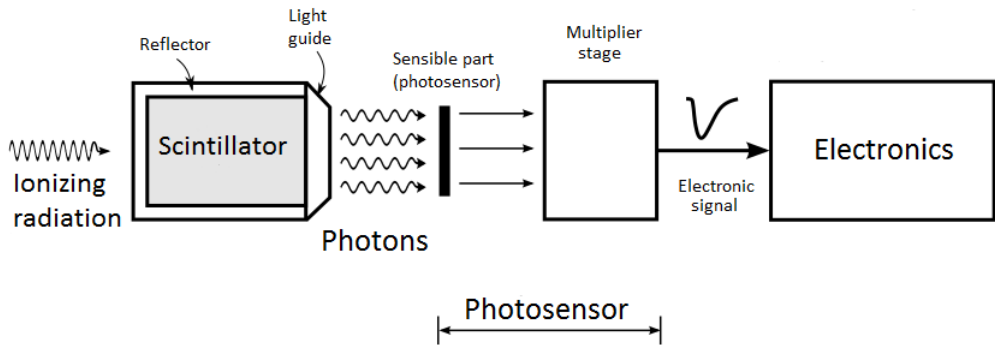


**Figura 3.1** – Scheme of the scintillator detector

### 3.2.1 Interaction of Fast Electrons and Photons with Matter

This section describes the interaction of particles with matter, focusing on the particles and energy range relevant for this thesis, electrons (0–18 keV) and photons in the visible range (approx. 380 – 750 nm).

Electrons have charge so their interaction with matter is mainly with the orbital atomic electrons through the Coulomb force. The electron trajectory is much more tortuous than other heavier particles because the mass of both interacting particles is equal. Furthermore, for the same reason, these electrons lose a significant amount of energy in each collision. The specific energy loss is defined as  $S = -\frac{dE}{dx}$  which gives the energy loss suffered by the particle per unit of path length. In the case of electrons, this total energy loss has two main contributions, the collisions (elastic and inelastic) and radiative processes (bremsstrahlung) [76, 77]:

$$\frac{dE}{dx} \approx \left( \frac{dE}{dx} \right)_c + \left( \frac{dE}{dx} \right)_{br} \quad (3.1)$$

The radiative part is roughly proportional to the collision part:

$$\frac{\left(\frac{dE}{dx}\right)_{br}}{\left(\frac{dE}{dx}\right)_c} \approx \frac{EZ}{700} \quad (3.2)$$

where  $E$  is the energy of the electron in MeV and  $Z$  is the atomic number of the absorbing material. Due to this energy loss, the electrons can only penetrate a material as far as they go before losing their total kinetic energy. This distance is known as range and, in the case of tritium electrons, its value is quoted in Table 1.4.

As photons don't have charge, their possible interactions with the matter are photoelectric effect, Compton effect, coherent scattering and pair production and the probability of each process depends on the energy of the photon,  $E_\gamma = h\nu$ , and on the atomic number of the material,  $Z$ , displayed in Figure 3.2.

The only relevant photons for this thesis are in the visible range, between 400 and 700 nm, that corresponds to energies of the order of the eV. Therefore, pair productions, which requires a photon energy equal or more than 1.022 MeV, does not play any role.

The photoelectric effect occurs when a photon interacts with an orbital electron in the material, losing all its energy. This energy is absorbed by the electron that is released from the atom (ionization). The energy of the resulting electron,  $E_e$ , is [76, 77]:

$$E_e = E_\gamma - E_b \quad (3.3)$$

where  $E_b$  is the binding energy of the electron in this material. The probability of this effect depends on the number of available electrons in the matter through the variable  $Z$ , and the energy of the electron according to

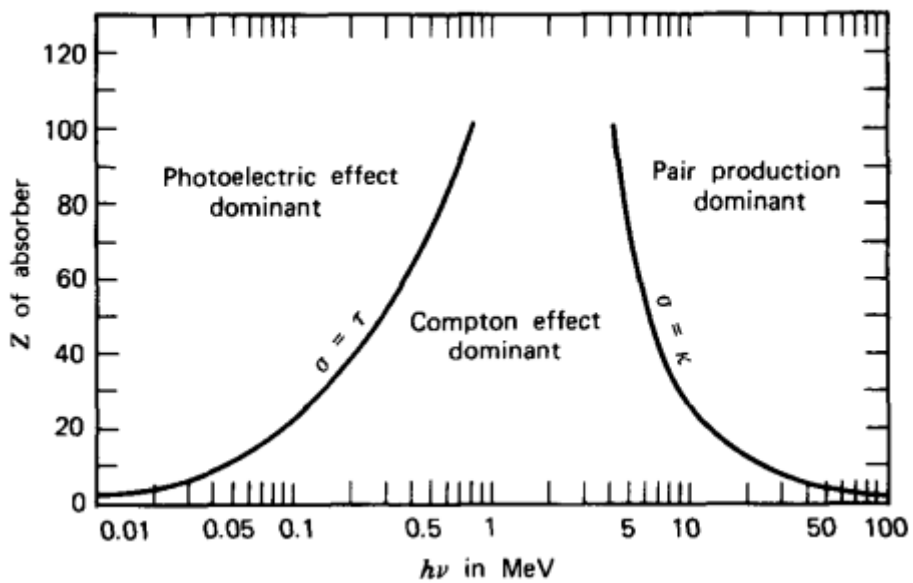


**Figura 3.2** – Domain regions of the three most probable types of interactions of gamma rays with matter. The lines show the values of  $Z$  and  $h\nu$  where the two neighboring effects are equally likely. [76, 77]

the expression [76]:

$$(Pr)_{Ph-eff} \approx \frac{Z^n}{E_\gamma^{3.5}} \quad (3.4)$$

Thus, the photoelectric effect is most probable for elements with high atomic number. This is the reason why elements with high atomic number are the best insulators against gamma radiation and why the passive shielding of TRITIUM monitor consists of lead bricks ( $Z = 82$ ) (section 3.4.1).

The Compton effect occurs when a photon interacts with an orbital electron of the material, transferring part of its energy to the electron, which is released, scattered at an angle  $\theta$  with respect to the original direction. If the electron binding energy is neglected, the energy,  $E_e$  transferred to it is given by [76, 77]:

$$E_e = \frac{\frac{E_\gamma^2}{m_0 c^2} (1 - \cos\theta)}{1 + \frac{E_\gamma^2}{m_0 c^2} (1 - \cos\theta)} \quad (3.5)$$

where  $m_0$  is the rest mass of the electron and  $c$  is the speed of the light in the vacuum. The probability of the Compton effect is proportional to the atomic number (available electrons in the matter),  $Z$ , and decreases with the energy of the photon.

As can be seen in Figure 3.2, for photon energies in the visible spectrum (of the order of eV), the Compton effect is only likely for very light materials, ( $Z < 4$ ). For heavier materials the photoelectric effect is the dominant effect.

Finally, for coherent scattering, the atom is neither excited nor ionized and the photon conserves all its energy in the collision. Coherent scattering is more probable for photons with low energies and materials with high atomic numbers and, as it will be shown in section 3.2.2, it explains

why the produced photons are guided along scintillating fibers.

### 3.2.2 Plastic Scintillators

Scintillators are widely employed for radiation detection in nuclear physics. Scintillator converts kinetic energy of the incoming particles in to light<sup>2</sup> which can be detected and quantified. Light emission happens through photon de-excitation of excited atoms.

Light production is linear in a wide energy range of incoming particles. Scintillators should have good optical properties, such as being transparent to the wavelenght of their own emission and having a refractive index as close as possible to that of glass for optimizing optical coupling with photosensors. Photon emission in scintillators is a stadistical process, which means that two identical events will emmit a different number of photons that follows a poisson statistics.

Scintillators can be organic and inorganic. Inorganic scintillators normally have a higher atomic number and density so their light output are higher. Due to these reasons they are better for gamma-ray spectroscopy. Organic scintillators are generally faster and they are commonly used for beta spectroscopy and neutron detection. This section is focussed on organic scintillators since they are the ones used in the TRITIUM project.

Organic scintillators are based on a scintillator material dissolved in a base solvent, normally aromatic hydrocarbons as C<sub>18</sub>H<sub>14</sub>, C<sub>24</sub>H<sub>22</sub>N<sub>2</sub>O or C<sub>15</sub>H<sub>11</sub>NO with an average atomic numbers of which are between 3,5 and 5.

The scintillator molecules, in which the organic scintillators are based, have a  $\pi$ -electron structure. The energy levels of their electrons are

---

<sup>2</sup>The light is made up of photons in the visible energy range.

commonly illustrated with a Jablonsky diagram, shown in Figure 3.3, which shows the fundamental singlet state,  $S_{0i}$ , where the valence electrons are, the excited singlet states,  $S_{jk}$ , and the excited triplet states,  $T_{lm}$ . The energy difference between  $S_1$  and  $S_0$  states is around 3 or 4 eV, in the visible range. As it is shown in the figure, each energy states are splitted in close sublevels separated around 0.15 eV. This fine energy structure is due to excitations of molecular vibrational modes tabbed by the second index of the energy states. As the energy levels and sublevels have an energy larger than the thermal energy, 0.025 eV, non-excited electrons are in the ground state  $S_{00}$  at STP<sup>3</sup>.

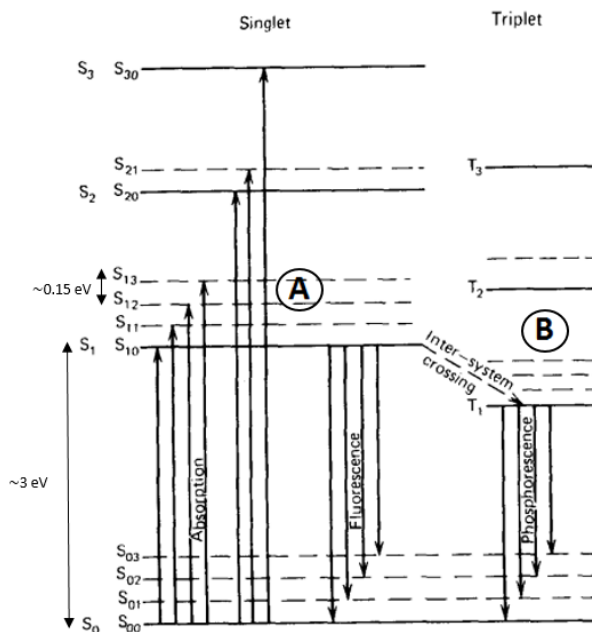


**Figura 3.3 –** Jablonsky diagram. [76]

When a particle deposits their kinetic energy in a scintillator, their valence electrons are exited to higher singlet energetic states very fast (times of the order of picoseconds) and are quickly de-excited to the first singlet

---

<sup>3</sup>Standar temperature and pressure conditions

excited state,  $S_{10}$ , through non-radiative processes known as internal conversion. These electrons can de-excited to the fundamental single state,  $S_{00}$ , through three different physical mechanisms:

- Prompt fluorescence (process A in Figure 3.3), where the electron in the  $S_{10}$  energy level is de-excited to some sublevel of the ground state  $S_{0i}$ , emitting a photon. This process happens immediately after the excitation of the scintillator molecules (around tens of nanoseconds after excitation). Each scintillator has a characteristic emission spectrum that defines its response due to the fluorescence mechanism.

Organic scintillators are practically transparent to their own fluorescence emission because there exist a quenching effect in each de-excitation process by which all emitted photons by the scintillator have less energy than the excitation. This effect is called Stokes shift and it is represented in Figure 3.4.

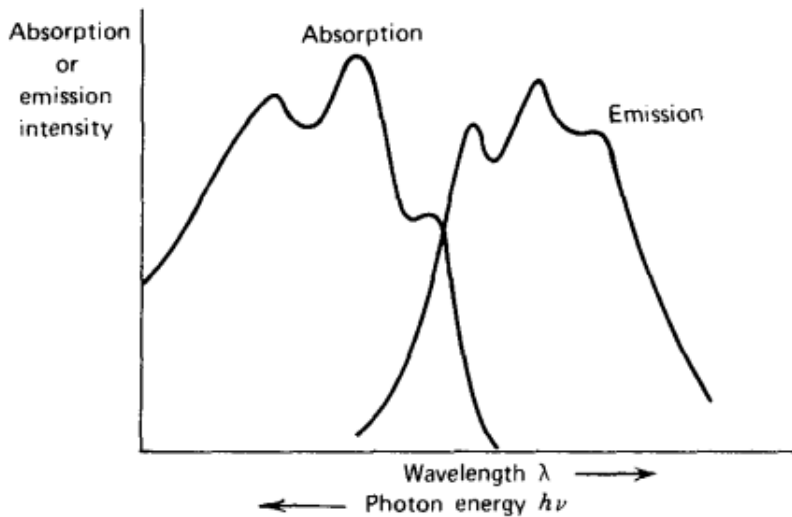


**Figura 3.4 – Stokes shift. [76]**

The intensity of the fluorescence emission in an organic scintillator over time is a combination of two exponential functions, one associated

with the lifetime of the level,  $\tau$  (on the order of nanoseconds), and the other associated with the energetic level population,  $\tau_1$  (on the order of picoseconds) [76].

$$I = I_0 (e^{t/\tau} - e^{t/\tau_1}) \quad (3.6)$$

- Phosphorescence, where the electron that is in the first single excited state cross to a triple excited state (process B in Figure 3.3) with a process called "intersystem crossing". This is a metastable state with a longer lifetime than phosphorescence. This process happens around  $10^{-3}$  seconds after scintillator excitation.
- Delayed fluorescence, which occurs when an electron is in a triple excited state but its transition to the ground state is forbidden. In this case, this electron interacts with another electron in a similar state, falling and return to the first singlet state and quickly de-exciting to the ground state.



This emission has the same emission spectrum as immediate fluorescence, but occurs later.

As the prompt fluorescence light produces the scintillator signal, detector design should increase it and reduce other possible physical mechanisms. One of the most important parameters is the scintillation yield<sup>4</sup>, defined as the the number of photons emitted by unit of absorbed energy. This yield depends on the type of particle and on other mechanisms that doesn't produce prompt fluorescence, like phosphorescence or delayed fluorescence

---

<sup>4</sup>The scintillation yield is a way of expressing the efficiency of the scintillator in converting the energy deposited by the particle into photons.

or even internal conversion. The scintillator yield is normally quoted by the manufacturer for mips<sup>5</sup>.

Plastic scintillators are easy to machine to any desired shape. The chosen shape for TRITIUM detector is the fiber, specifically, commercial fibers BCF-12 from Saint-Gobain Crystals Inc company [78]. This type of fiber was chosen as the result of a comparative study [79] among some of the best-known commercial manufacturers.

The BCF-12 fibers consist of a scintillating of polystyrene with the possibility of surrounding it by a cladding of polymethylmethacrylate (PMMA) (smaller refractive index than core in order to achieve a critical angle) or a multicladding (second cladding) with even smaller refractive index.

When a particle deposits all or part of its kinetic energy, some photons are produced in the fiber core as a result of the scintillating process. The number of photons produced depend on the scintillation efficiency and its value is around 2.4% for the fibers used (BCF-12), which means that a scintillation yield of 8000 photons will be produced per MeV for a mip. For instance, for tritium electron, these fibers release a maximum of around 148 photons (when tritium electron has the maximum energy, 18.6 keV), or less as electrons of these energies are not mips. The emission spectrum of the fibers employed in this work, is shown in Figure 3.5.

The scintillation light is guided to the sensitive part of the photosensor. A single photon produces a signal with some probability, called the quantum efficiency. Fibers (and scintillators in general) use the optical property of Snell's law [80] to guide their photons to the desired part (ends of the fibers). It is based on the interface created between the core and the surrounding material. When a photon hits this interface, it is refracted

---

<sup>5</sup>The MIP, Minimum Ionized Particles, is a particle that has the speed that generate minimum ionization, that's, for example, electrons with 500 keV or more

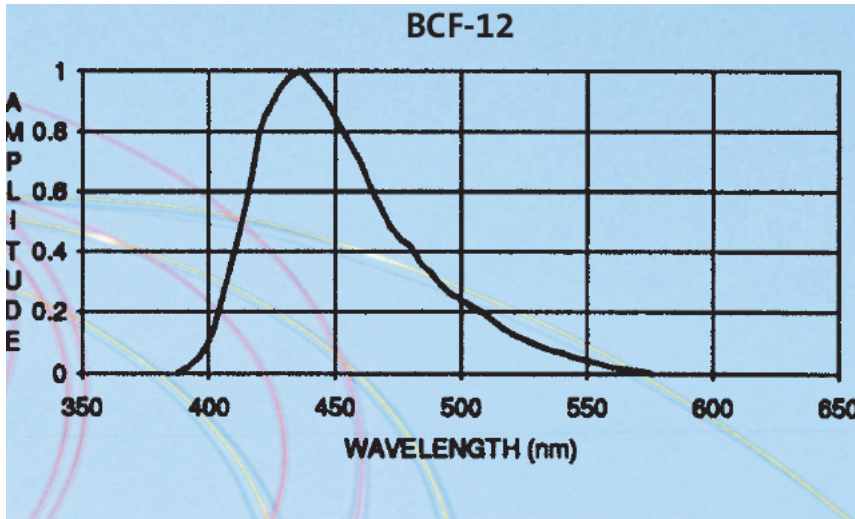


**Figura 3.5** – Emission spectrum of BCF-12 fibers of Saint-Gobain. [78]

(and therefore lost) following the Snell equation, 3.8 [80].

$$n_0 \sin(\theta_0) = n_1 \sin(\theta_1) \longrightarrow \theta_c = \arcsin\left(\frac{n_1}{n_0}\right) \quad (3.8)$$

If the surrounding material has a lower refractive index than the core of the fiber, there exist a critical angle,  $\theta_c$ , beyond which photons will be totally reflected and therefore kept within the fiber as illustrated in Figure 3.6.

The trapping efficiency or photon collection efficiency is defined as the efficiency of the scintillator to guide photons. For BCF-12 fibers with optical clad is between 3.44% and 7% per meter of fiber (depending on where the event is detected and is minimum near the fiber axis and maximum near the core-clad interface. For no clad fibers BCF-12 surrounded by water, the trapping efficiency is larger than for cladded fibers. Therefore, from the maximum of 148 photons initially created by a tritium decay electron with the maximum energy, only 41 photons (for maximum trapping efficiency)

are guided in the 25 cm fiber length used in the TRITIUM detector. Thus, the output signal is very weak and is in the range of the spectrum where electronic noise is already significant. As described in the following chapters, a great effort was made to minimize electronic noise by different techniques.

In Figure 3.6 the light collection in a fiber is illustrated.

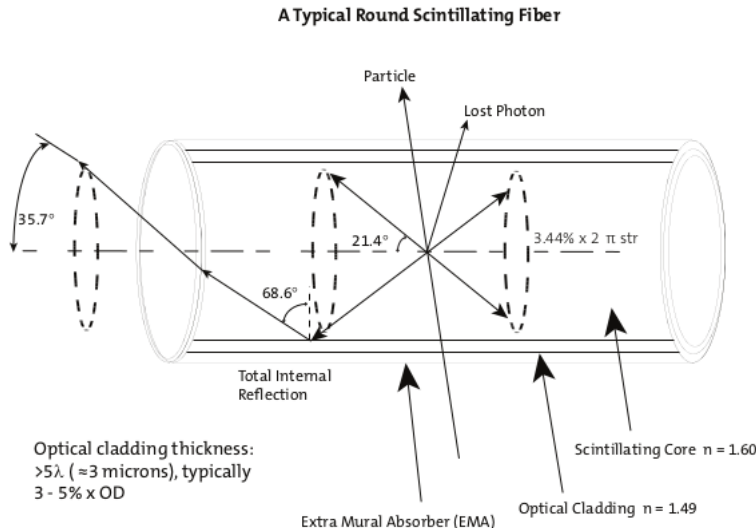


**Figura 3.6** – How photons are collected in a fiber with single clad. [78]

The cladding material is useful for protecting the core surface from dirt or aggressive external agents that may reduce the light collection but at the cost of increasing the critical angle which its corresponding loss of light. Three different cases are shown in Table 3.1, where the cladding effect is illustrated.

In the practice, it is difficult to achieve a perfect air-core or water-core interface which affects light collection. As commercial claddings are thicker (30  $\mu\text{m}$ ) than the mean free path of tritium decay electrons in water (around 5  $\mu\text{m}$ ) cladded fibers is not an option for the TRITIUM detector. Hence, special attention is needed for achieving a water-core interface good enough. To overcome this problem a special protocol was developed in the

Material	Refractive index	critical angle ( $^{\circ}$ )
Air	1	42.98
Water	1.33	62.47
Cladding of PMMA	1.49	76.26

Table 3.1: Critical angles associated to different interfaces created with polystyrene,  $n_0 = 1.6$ , and other materials

ICMOL laboratory for preparing fibers for tritium detection.

The most important parameters of scintillating fibers of TRITIUM are given in Table 3.2.

### 3.2.3 Light Detection in Photosensors

The scintillating photons created in the core of the fiber and guided to its end are detected by photosensors. Photosensors have a sensitive part that is optimized to detect photons in a range of energy (usually in the visible range) with a certain probability, called quantum efficiency. The photosensors produce an electronic signal that carries information about the detected photons such as number and detection time.

There are many available photosensors that rely on various physical processes, such as photoelectron multiplier tubes (PMTs), silicon photo-electron multiplier (SiPM) or charge-coupled device (CCD).

To optimize the efficiency of a scintillation detector is essential that the emission spectrum of the scintillator (Figure 3.5 for the fibers used) overlaps as much as possible with the detection efficiency spectrum of the photosensor chosen. The detection efficiency spectrum shows the probability of detecting photons at a function of wavelength. The efficiency of a detector is proportional to the product of both the emission and the

Core material	Polystyrene
Core refractive index	1.60
Density (g/cm <sup>3</sup> )	1.05
Cladding material	Acrylic (PMMA)
Cladding refractive index	1.49
Cladding thickness ( $\mu\text{m}$ )	30
Numerical aperture	0.58
Trapping efficiency	3.44% minimum
No. of H atoms per cc (core)	$4.82 \cdot 10^{22}$
No. of C atoms per cc (core)	$4.85 \cdot 10^{22}$
No. of electrons per cc (core)	$3.4 \cdot 10^{23}$
Radiation length (cm)	42
Emission peak (nm)	435 (Blue)
Decay Time, (ns)	3.2
1/e Length (m)	2.7
Scintillator yield (# $\gamma$ /MeV)	$\sim 8000$
Operating Temperature	$-20^\circ\text{C}$ to $50^\circ\text{C}$

Table 3.2: Properties of BCF-12 fibers from Saint-Gobain Inc. [78]

detection efficiency spectra and this is largest when both spectra match.

The proposal of TRITIUM is to use SiPM arrays because they are very fast (of the order of ns) and have a high photodetection efficiency of about 50%, high gains (multiplication factor of  $10^6$ ) and a low voltage supply. The most important reason of this choice is that SiPM arrays are able to detect a single photon with high efficiency, which is a fundamental aspect due to the low amount of photons generated by tritium decay. The PMTs, which are the conventional choice, were also tested because they have lower dark count rate than SiPM and similar properties like gain and timing.

### Photoelectron Multiplier Tubes (PMTs)

Photoelectron multiplier tube, PMT, employed as photosensors in nuclear physics during decades, detect the scintillating photons that reach its sensitive part, photocathode, and produce an electronic signal, large enough to be easily measured. In Figure 3.7 a schematic drawing of a PMT is given. The PMT consists of a vacuum tube that has a glass window through which photons can penetrate. The electrons created in the photocathode travel in vacuum.

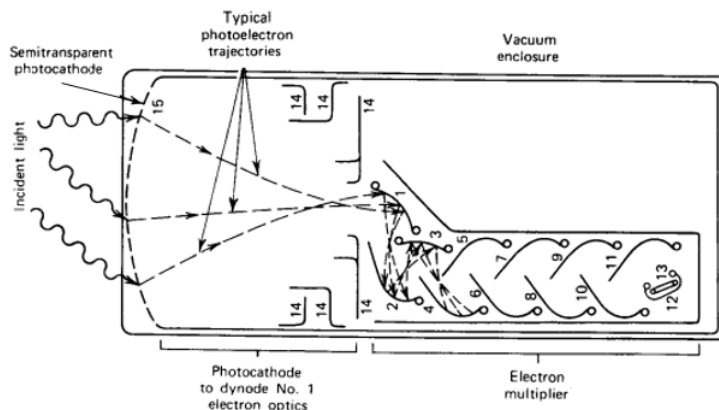


**Figura 3.7** – Scheme of a PMT. [76]

The signal production has two phases:

1. In the photoathode photons are converted in photoelectrons through photoelectric effect. The photocathode consists of a thin layer, of the order of nanometers, deposited on the inner surface of the PMT window. The material of the photocathode is chosen to optimize the probability of producing photoelectric effect with the scintillating photons. The PMTs used in TRITIUM experiment are the model R8520-406 from Hammatsu [81] and the material of their photocathode is Bialkali<sup>6</sup>.

---

<sup>6</sup>The bialkali material is based on the elements  $^{121}\text{Sb}$ ,  $^{85}\text{Rb}$  and  $^{132}\text{Cs}$

The response of the PMT at long wavelengths is limited mainly because photon energy is not enough to produce a photoelectric effect or the emitted photoelectron does not have enough energy to overcome the material-work function. The response of the PMT at short wavelengths is limited due to absorption in the window material, quartz in our case. Thus, the response of the PMT has a strong dependence on the energy of the photon and the quantum efficiency (QE) spectrum defined is given by the ratio of the number of photoelectrons produced at the cathode of the PMT and the number of photons reaching it. For PMTs used in the TRITIUM experiment, the QE is showed in Figure 3.8.

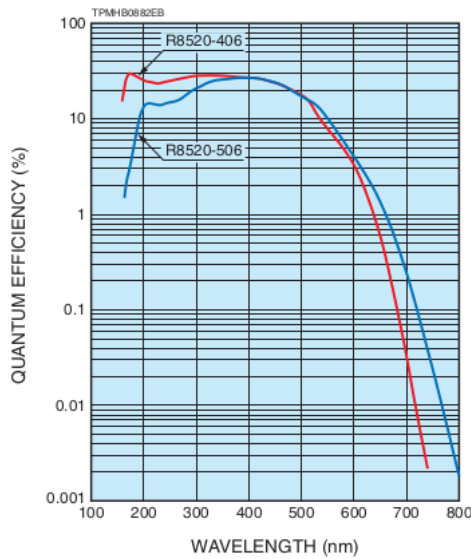


**Figura 3.8** – Quantum efficiency spectrum for the PMT used (R8520-406). [81]

The maximum values of the PMT quantum efficiency is usually between 20% and 30% [76] (a little bit less than 30% for the PMTs employed). The emission spectrum of the scintillating fibers used, Figure 3.5, matches the quantum efficiency spectrum of the PMTs used, Figure 3.8 and the position of both peaks is very close, 435 nm

for fibers and 420 nm for PMT.

2. As the number of photoelectrons produced in the photocathode is very small, an electron multiplication stage is employed to obtain an electronic signal of sufficient size to be processed by the electronic system. The amplification stage is based on three elements, focusing electrodes, dynodes and anode, which are metallic plates with a shape and position designed to optimize the collection and multiplication of electrons. A high voltage (HV) is applied to the PMT which is distributed between all this elements, including the photocathode, with the help of electronic circuit. A positive HV, grounded in the photocathode, is interesting for measuring PMT currents, and a negative HV, grounded in the anode, gives a faster response. The commercial electronic circuits of Hammatsu are shown in Figure 3.9.

Focusing electrodes guide the photoelectrons to the first dynode. They have an collection efficiency (CE) defined as the ratio of the number of photoelectrons reaching the first dynode and the number of photoelectrons leaving the photocathode and its value is around 80%. The dynodes achieve the electron multiplication. A voltage difference between adjacent dynodes accelerates the electrons and produce their multiplication. The multiplication factor of each dynode,  $\delta$ , is commonly around 5 and is strongly dependent on the HV. If all dynodes have the same gain, the overall gain of a PMT with  $N$  dynodes is [76]:

$$G = CE \cdot \delta^N \quad (3.9)$$

that give an overall gain of a PMT of the order of  $10^6$ , strongly dependent on the applied HV.

The multiplication stage adds an uncertainty in the measurement. Working without gain allows to count the number of photons that reach the PMT. This can be done by short-circuiting all the dynodes and the anode and collecting the signal directly of the photocathode. This special setup was used for fiber characterization, described in

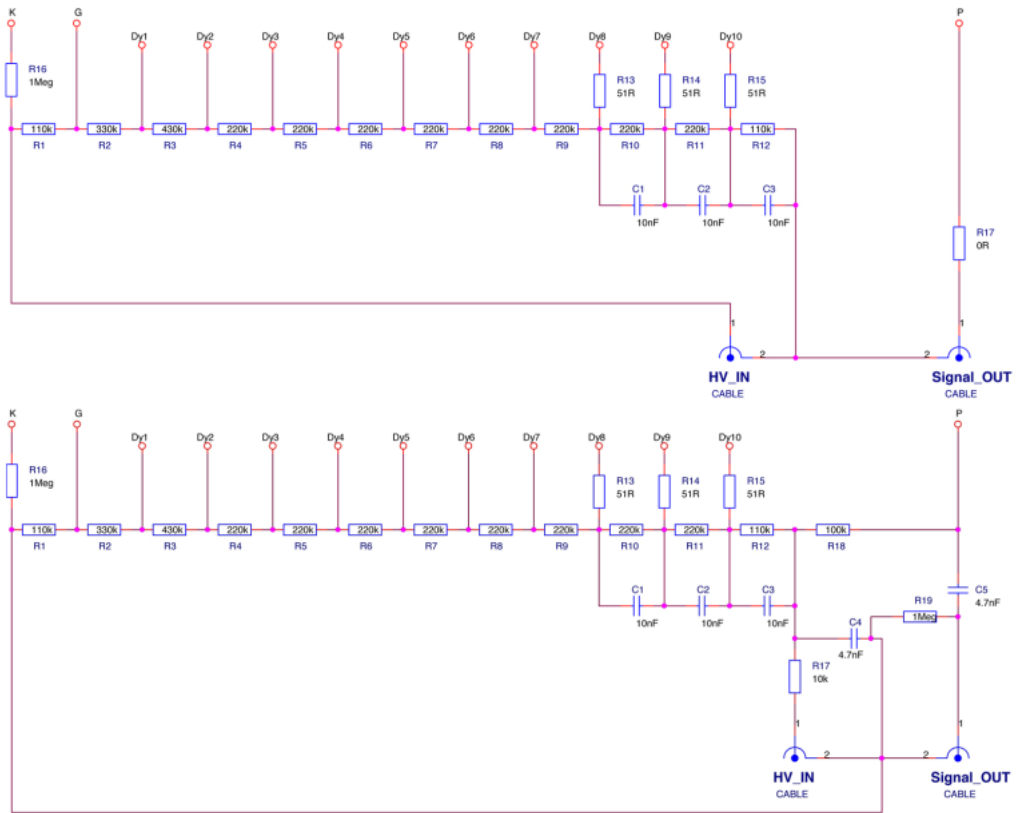


**Figura 3.9** – Hamamatsu commercial voltage divider electronic circuit. Upper circuit with negative supply and lower circuit with positive supply. [81]

#### section 4.1.3.

The output pulse of a PMT has a width of the order of tens of nanoseconds. The multiplication process can be described as a Poisson statistical process. For each electron in the first dynode, G new electrons are created with a variance of  $\sqrt{G}$ .

The output signal of a PMT is linear with the number of photons that reach its sensitive part up to a saturation limit, at which the linearity is lost. This limit depends on the PMT model.

The photocathode may emit electrons without any scintillation light. This signal is named dark current,  $I_{DC}$ , and can arise due thermoionic emission and, for the PMTs used, this value is around 2 nA according to their data sheet.

The characterization of the PMTs used for dark current, gain for several HV and quantum efficiency, was done at IFIC in the framework of NEXT experiment [82].

### Silicon Photoelectron Multiplier Array (SiPMs array)

The Silicon Photomultiplier (SiPM) are a bind of photosensor, based on semiconductor materials, developed in recent years. They are replacing progressively conventional PMTs in many experiments and applications. They achieve outstanding photon-counting capabilities with high gain and high photodetection efficiency comparing to PMT. They have convenient characteristics as insensitiveness to magnetic fields, low operating voltage and compactness.

SiPM are based on p-n junctions, made with special techniques to achieve a good contact between both surfaces.

The voltage at which the SiPM changes from proportional to geiger mode is called the breakdown voltage,  $V_{BR}$ . At a lower voltage it works in proportional mode but at a higher voltage, it switch to Geiger mode. The measurement of the breakdown voltage is one of the most important parametes to characterize the SiPM and Its determinations is described in section 4.2.

The SiPM, formed by a matrix of APDs which are photodiodes operating in Geiger mode. A scheme of an APD is shown in Figure 3.10. It has p+ and a n+ layers.

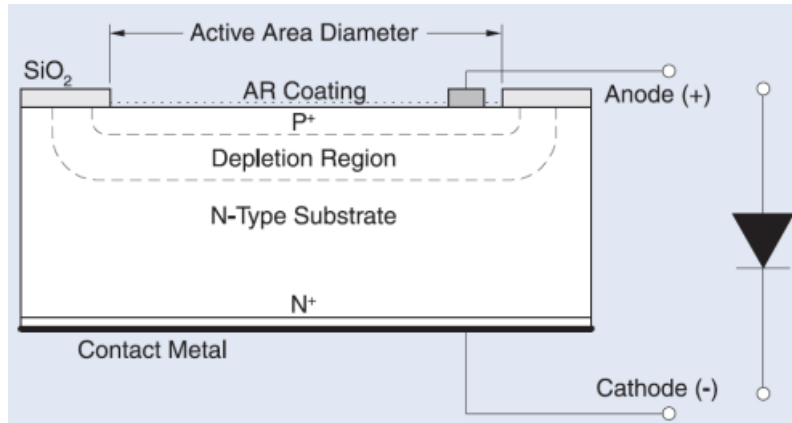


**Figura 3.10** – Scheme of a APD and electrical symbol used. [84]

These APDs, called pixels when they are part of a SiPM, are connected in parallel and the sum of all of them is read. The output signal of the pixels are quite similar regardless of the energy deposited, with some difference because of the uncertainty due to the SiPM manufacturing process and the statistical nature of the detection process. The energy deposited in each APD is not known but, as all SiPM pixels are read at the same time, the charge of the output signal when  $n$  photons are simultaneously detected is  $n$  times the charge of a single photon, as can be seen in Figure 3.11. Due to this property, after a correct calibration of SiPMs the number of detected photons we have detected is linearly related to the output signal.

As the number of scintillating photons is proportional to the deposited energy, the linearity of its output signal and the deposited energy is obtained.

On top of that, these pixels need to be so small<sup>7</sup> that, if the photon density to be detected is low enough, we only detect one photon in each pixel. If it doesn't happen, we will detect two or more photons with the same pixel but the output signal will be the same as one detected photon, so

---

<sup>7</sup>Pixel sizes for commercial SiPMs are 50 or  $75\mu\text{m}$  [85], [86]

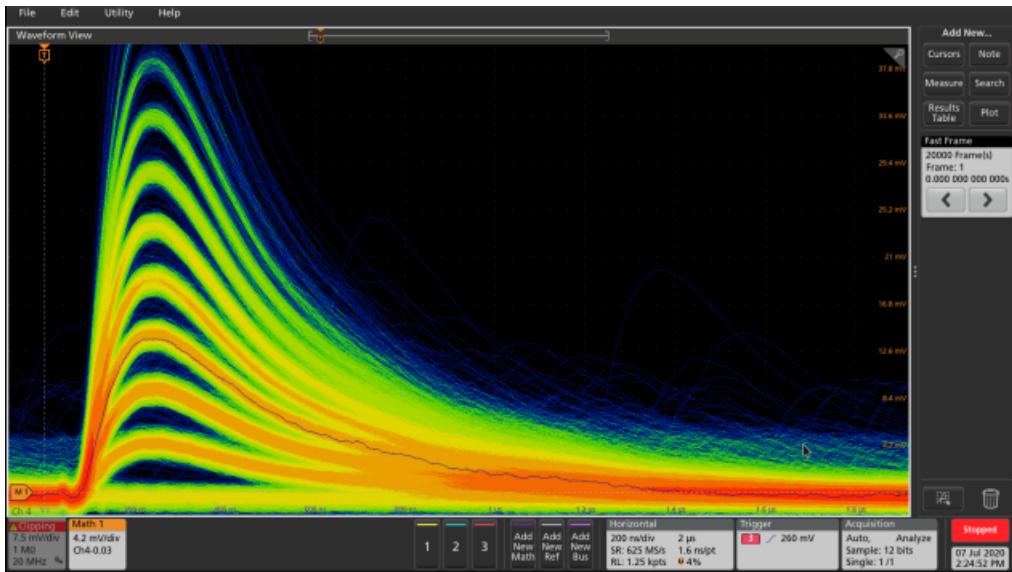


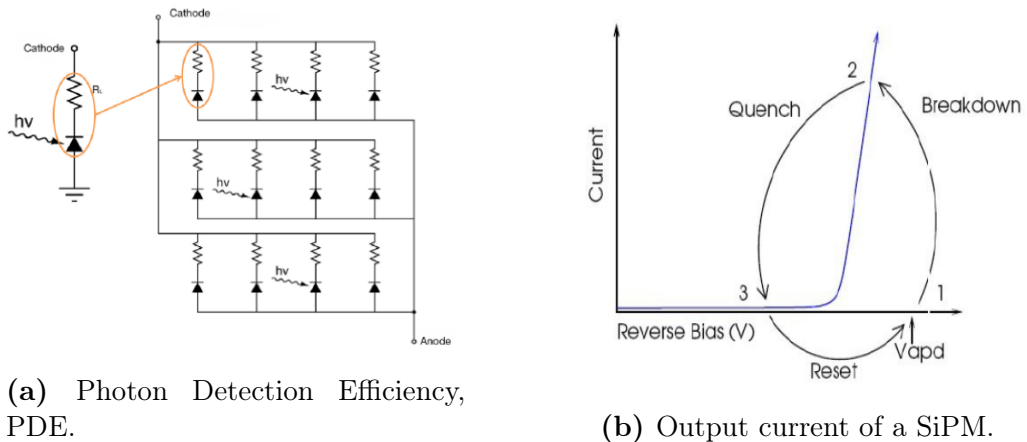
**Figura 3.11** – Using persistence on the oscilloscope to show several pulses with different heights. Each height associated with a different number of SiPM pixels lit at the same time.

we will have a loss of linearity of our output signal. This effect is known as saturation and it is important to know the photon density at which it happens for our SiPMs. The experimental measurements of this effect, which have been done for our SiPMs, is shown in section 4.2. SI LA MIDO YO PERFECTO, SI NO DECIR QUE PARA NEUSTRO CASO NO ES IMPORTANTE PORQUEU ESTAMOS MIDIENDO MUY POCOS FOTONES POR EVENTO.

Each of these pixels has a quenching resistance<sup>8</sup> in series that is used to stop the current produced when this pixel has detected a particle. It is used for limit the current drawn by the diode during breakdown and reduce the reverse voltage seen by the diode to one below the breakdown voltage. After that, the voltage seen by the diode is reset to the bias voltage and this pixel is ready to detect a new particle again. In Figure 3.12 (left)

---

<sup>8</sup>The tipical valuer of this quenching resistance for commercial SiPMs is around 500 kΩ



(a) Photon Detection Efficiency, PDE.

(b) Output current of a SiPM.

**Figura 3.12** – (Left) Electronic scheme of a SiPM and (right) output current of a SiPM as a function of the reverse voltage. It show that the quenching mechanism is essential for working with SiPMs [89].

a diagram of these chenching resistances and APDs in a SiPM and (right) how it works is shown respectively.

In this simple electrical scheme we can see that all pixels have a common cathode and anode which means that, as we said before, they are at the same bias voltage and the output is the sum of all of them.

We have a lot of names to refer to these photosensors such as SiPMs, MPPCs, G-APDs, SSPMs, MRS-ADPs or AMPDs. The candidate for TRITIUM project is S13360-6075 from Hamamatsu photonics [86] because its characteristics are the ones that best fit our objectives since this model has super low afterpulses, crosstalk and dark counts than other SiPM models from Hamamatsu. Its characteristics and properties are shown in Table 3.3.

These values, provided by Hamamatsu photonics, are only approximate for a given element so. Therefore, these parameters must be determined experimentally for each SiPM because they can vary significatively

Parameter	Numerical value
Serie	S13360
Model	6075
Pixel Pitch ( $\mu\text{m}$ )	75
Effective photosensitive area ( $\text{mm}^2$ )	$6.0 \times 6.0$
Number of pixels	6400
Fill factor	82%
Refractive index of windows material	1.55
Operating temperature range ( $^\circ\text{C}$ )	[−20, 60]
Spectral response range, $\lambda$ (nm)	[320, 900]
Peak sensitivity wavelength, $\lambda_p$ (nm)	450
PhotoDetection Efficiency, PDE, $\lambda = \lambda_p$ (%)	50
Dark counts, Typical/Maximum (kcps)	2000/6000
Terminal capacitance, $C_t$ (pF)	1280
Gain, M,	$4 \cdot 10^6$
Breakdown Voltage, $V_{BR}$ (V)	53
Cross talk probability(%)	7
Temperature coefficient $\Delta TV_{op}$ ( $\text{mV}/^\circ\text{C}$ )	54

Table 3.3: Characteristics of SiPM S13360-6075 from Hamamatsu Photonics [86].

even for SiPMs of the same model. The most important characteristics for the TRITIUM project are experimentaly measured and given in section 4.2.

Although TRITIUM detector uses whole SiPM matrices, the characterizations has been carried out at the level of a single SiPM (same model) to learn the values of the SiPM parameters and to test the gain control method.

The matrices selected are of the model "S13361-6050" from Hamamatsu, which consists of a  $4 \times 4$  SiPM matrix where the active area of each SiPM is  $6 \times 6$  mm [87] or the model "S13361-3050" from Hamamatsu, which consists of a  $8 \times 8$  SiPM where the active area is  $3 \times 3$  mm [88]. They are commercial matrices from Hamamatsu and the total active area that they cover is the same for both models,  $24 \times 24$  mm and it is approximately the same as the active area covered with the PMTs employed, described in the previous section. These matrices have a common bias voltage and ground for all SiPMs but a different output signal for each SiPM.

## Comparison of photosensors considered

The photosensors employed in TRITIUM are both, PMT and SiPM. Each kind of photosensor has his advantages and disadvantages, so both were tested to make a final choice. The output signal of both photosensors is proportional to the number of incident photons and they have a similar gain (of the order of  $10^6$ ). Both properties are essential to detect tritium events and to obtain a signal large enough to be measured and processed. Both photosensors have fast output signals, with a rise time shorter than nanoseconds, and a wide spectral sensitivity (200 – 800 ns for PMT and 300 – 900 ns for SiPM). The supply voltage necessary to work with SiPM, on the order of tens of volts, is much lower than that of PMTs, which require a high voltage, of the order of a thousand volts. The PDE at 420 nm, achieved with SiPM is higher, around 50%, than with PMT, which have a PDE about

30%. A large PDE is essential because the number of photons produced in a tritium event is very low. Furthermore PMTs, as they consist of a vacuum tube, are more bulky and fragile than SiPMs, which are compact and robust. This is an advantage for the SiPMs because TRITIUM detector should work during years. Furthermore, PMTs are rather more expensive, than SiPMs. In addition, PMTs are affected by magnetic fields, contrary to SiPMs that works correctly in intensities of magnetic field up to 7 Tesla. Moreover, due to their high uniformity, SiPMs are capable of distinguishing the exact number of photoelectrons detected and even of resolving a single photoelectron, which is not possible with PMTs due to variations in their gain.

On the other hand, the dark current of PMTs is much lower (a few counts per second) than that of SiPMs, that have a dark current between 0.1 and 1 Mcps<sup>9</sup>, depending on their size, and this happens almost entirely at the level of a single photoelectron. This prevents to separate tritium decay signals from background in the signal photon-detection zone. Another inconvenient of SiPMs is large crosstalk and afterpulses that need to be corrected.

An additional drawback of SiPMs is that their output signal depends strongly with the temperature. As TRITIUM detector will be installed in an environment with significant temperature variations, this problem is solved by a suitably changing the supply voltage to compensate temperature variations.

### 3.2.4 Electronic Readout

The electronic system is in charge of reading, processing and analyzing the output signal of photosensors and providing output information about the

---

<sup>9</sup>Mega counts per second,  $10^6$ c/s

tritium detection. This electronic system depends on the type of detector configurations employed

### Electronical system for PMTs

PMTs were used in TRITIUM experiment for two main objectives. On the one hand, to know the amount of incident photons that reached the PMT photocathode, which is important to characterize fibers, and, on the other hand, to know the energy of events, which allow us to obtain an energy spectrum and to discriminate events according to their origin.

To know the amount of photons that have reached the photocathode, the PMT should work without internal gain since it introduces a large uncertainty in the measurement. To this end, the electron multiplication stage (shown in section 3.2.3) must be bypassed. This is achieved with the help of a PCB, shown in Figure 3.13, designed, built and tested for this purpose.

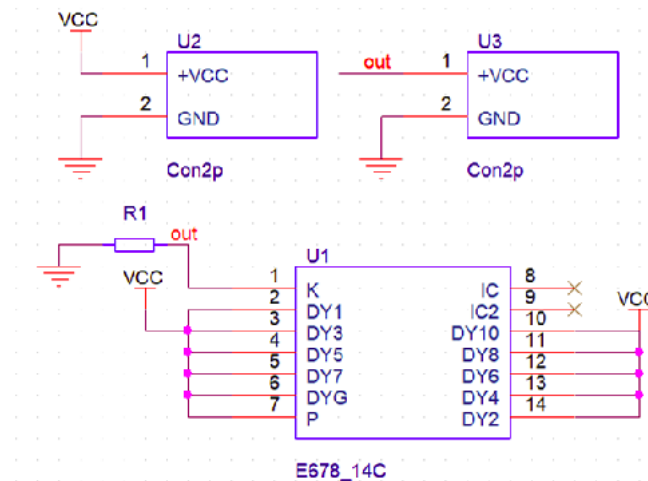


**Figura 3.13** – Electronic scheme of the electronic voltage divider circuit used for working with PMTs without its internal gain.).

This PCB short-circuit the dynodes and reads the signal directly from the photocathode. This PCB was designed to be supplied with a positive voltage smaller than usual running voltage because It is only needed to create a voltage difference between the photocathode and the first dynode. As the signal is not multiplied, the output pulse of the photosensor is very small (currents of the order of tens of nanoamperes and a special readout system is needed. The chosen system is Keithley 6487 Picoammeter/Voltage Source [90], a commercial system from Keithley. This system has some useful options such as automatic baseline correction, the ability to read currents of the order of picoamperes and the possibility of carrying out mathematical operation on the signal, such as the average of N measurements with the associated statistical error, where N is programmable by the user ( $N = 100$  in all our studies). This is the configuration set to measure the output current of our photosensors. The number of photons that has reach the photocathode is calculated from:

$$N^o \gamma / \text{sec} = \frac{(I_{PMT} - I_{DC})}{q_e \cdot QE \cdot CE} \quad (3.10)$$

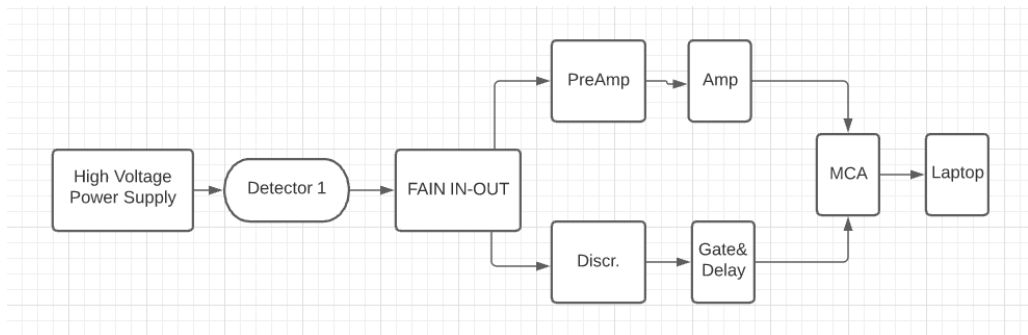
where  $I_{PMT}$  is the output current of the PMT when it detects photons and  $I_{DC}$  is the dark current. This equation takes into account the quantum efficiency of the PMT, which is close to 30%, and the capture efficiency in the dynodes, equal to 1. In addition, it is assumed that each detected photon only generates one electron, the charge of which is  $q_e$ .

To determine the energy of the events, the internal gain of the PMT has to be restablished.

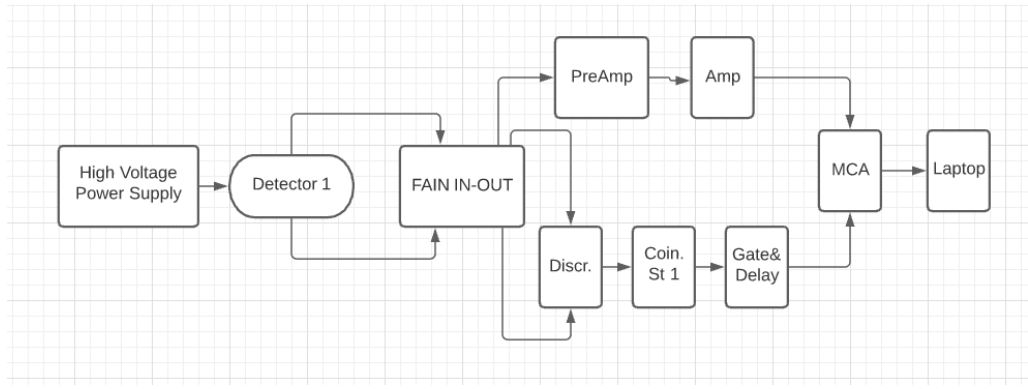
The number of PMTs used are one, two or four, depending on the measurement. A simplified scheme of the electronic chain employed in each case is shown in Figures 3.14a, 3.14b and 3.14c, based on various NIM technology modules<sup>10</sup>.

---

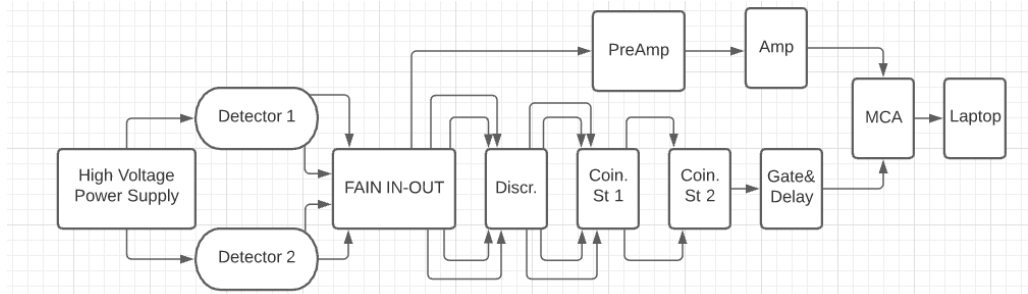
<sup>10</sup>The Nuclear Instrumentation Module (NIM) is a standard specification convention for electrical and mechanical parameters defined in electronic modules used in experi-



(a) Electronic scheme employed when only one PMTs are used in time coincidence.



(b) Electronic scheme employed when two PMTs are used in time coincidence.



(c) Electronic scheme employed when four PMTs are used in time coincidence.

**Figura 3.14** – Schemes of the different electronic for measuring with PMTs.

The PMTs are supplied in all the cases by TC 952 High Voltage Supply from Tennelec [91], which has four channels. If two or more configurations are needed, a second voltage supply HV Power Supply N 1130-4 from Wenzel Elektronik company [92] with 4 additional channels, was employed.

As it can be seen in the figures, there are two different lines followed by the PMT output signals, the amplification line and the time coincidence line. Therefore, the first module needed is an analogic FAN IN-OUT module which is used to duplicate the input signal. The module employed is the Quad linear FAN IN-OUT MODEL 740 from Philips Scintific [93], which has four channels. One output signals is used as the input for the amplification part and a second is used as the input for the time coincidence part.

1. The amplification line, which is the same for the three configurations, provides the energy information and is based on two steps:
  - (a) One of the output signals is integrated by a preamplifier, which gives an output signal with a height corresponding to the charge of the input pulse. This signal has a long tail<sup>11</sup> produced by the preamplifier capacitance. The preamplifier used is "MODEL 9326 FAST PREAMP" from ORTEC [94].
  - (b) The output signal from the preamplifier is lead to the amplifier which gives an amplified output with a shape close to a Gaussian function. The used amplifier modules are 575A and 671 from ORTEC [95, 96]. An example of the output signal for 575A module is shown in Figure 3.16, green color.
2. The time coincidence line contains the time information and gives the gate that triggers coincident signals of both PMTs. This line consists of:

---

mental nuclear and particle physics.

<sup>11</sup>The length of the tail is,  $\tau = RC$ , where R is the input resistance and C is the capacitance used. It is the typical output signal in RC circuits.

- (a) One of the output signals of the FAN IN-OUT module of each PMT is introduced into a discriminator module that gives a logic signal of  $-1.2$  V height and of  $240$  ns width when a given threshold is exceeded. The discriminators utilized are Octuple Constant-Fraction Discriminator CF8000 module from ORTEC [97] and 4 channels discriminator model 84 from CAEN [98].
- (b) Time coincidences are required to ensure that detected event comes from the scintillating fibers and to remove background like external light and dark current.

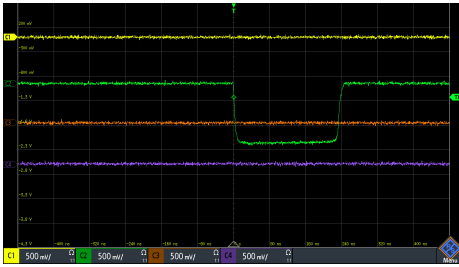
The two logic signals given by the discriminator module that come from the two PMTs in the same detector are introduced in the coincidence module which generates an output signal of  $-1.4$  V height and of  $20$  ns width, when both are in coincidence. The modules used are Coincidence Unit Model 465 from LeCroy [99] and Coincidence Type N6234 from CERN-NP [100].

- (c) Time coincidence of two different detectors (4 PMTs, configuration 3.14c was also studied, which is useful to remove background due to hard cosmic radiation.

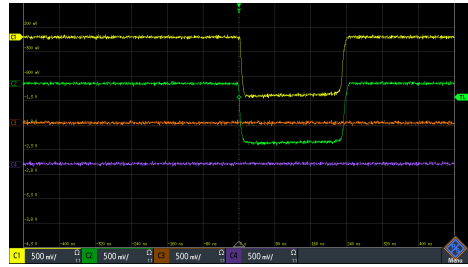
To do so, a new coincidence step similar to the previous one must be applied. The two logical output signals of the single detector coincidence are checked for coincidence.

Some examples are shown in Figure 3.15 for time coincidences of two detectors (4 PMTs). There, four logical signals are shown, two of them (channel one and two, yellow and green respectively) come from two PMTs connected to the first detector and the other two signals (channels three and four, color orange and violet respectively) come from PMTs connected to the second detector.

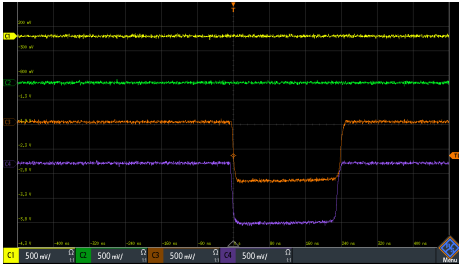
- i. In Figure 3.15a only one PMT (channel two) has detected an event. It means that the event is likely not produced in the scintillator. In this case, no output is generated.
- ii. In Figures 3.15b and 3.15c two PMT signals of the same



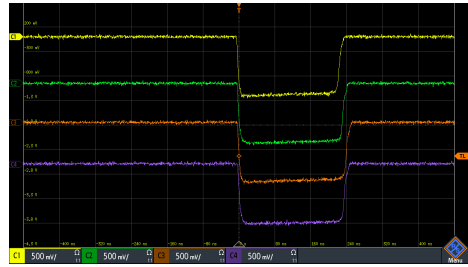
(a) Event detected in only one PMT, one detector.



(b) Event detected in two PMTs, one detector.



(c) Event detected in two PMTs, other detector.



(d) Event detected in all PMTs, both detector.

**Figura 3.15** – Different situation that can happen when time coincidences with PMTs are done.

detector are generated but the other detector gives no signal. This event is discarded.

- iii. In Figure 3.15d the four signals are detected, which means that the output signal is generated and the event is recorded.
- iv. The logical output signal, is introduced in the Gate and Delay Generator, model 416A of the company ORTEC [101], which gives a positive logical signal, shown in Figure 3.16, orange color, with a height of 8 V and width of 2  $\mu$ s.

At the end, a logical and analogical signals are obtained, shown in Figure 3.16, which are recorded by the MCA 8000D, Pocket MCA from AMPTEK [102]. The analogical signal has information about the energy of the event and this is the signal whose information we will save for analyz-

ing. On the other hand the logic signal (output from the Gate and Delay Generator module) that indicates when the amplified signal must be saved.



**Figura 3.16** – Signal amplified and logical gate (input signals of MCA).

The MCA is a module used to record the signal height as a histogram. The height of the signal (green signal) corresponds to the energy of the event and, when there is a gate (orange signal), is recorded.

### Electronical system for SiPMs

The SiPMs are used in the TRITIUM experiment in two different ways, at the level of a single SiPM and at the level of several SiPMs arranged in a matrix. Both studies were carried out to characterize the SiPM arrays used in the TRITIUM monitor.

The electronic system chosen to process and analyze the output signals of the SiPM arrays is PETsys [103], which is a commercial system prepared to work with SiPM matrices from Hamamatsu.

PETsys is a complete acquisition and digitization system that is capable of working with up to 1024 SiPM. This system consists of a basic board, which processes the signal, to which 16 different SiPM matrices can be connected with up to 64 SiPM per matrix. This number of channels is needed in the TRITIUM project because, as it is shown in section 5.3, the TRITIUM monitor consists of a large number of SiPM matrices with 16 channels (SiPMs) per matrix. The PETsys system used in TRITIUM is displayed in Figure 3.17.



**Figura 3.17** – Different parts of PETSYS system. [103]

Although the capacity provided by PETSYS should be enough for the requirements of the TRITIUM project, TRITIUM is a modular detector with scalable sensitivity. It means that, if an improvement of its limits is needed to improve its sensitivity or to further reduce the background, more photosensors would be needed. Therefore, the electronic system should be able to increase its capacity in a scalable way. This requirement is fulfilled by PETSYS since it has an additional module, called Clock and Trigger, to which up to sixteen different PETSYS basic boards can be connected. These sixteen PETsys basic boards are read in parallel, giving a total system

capacity of reading 256 SiPM matrices (16384 SiPMs<sup>12</sup>).

PETSYS is based on C++ and Python scripts that are prepared for the main tasks required, such as time coincidence options between SiPM (or even SiPM matrices) or energy discrimination. It is open source, giving the possibility to modify the current scripts or develop others with additional functions. PETsys has a time resolution of 250 ps which is one of the best time resolutions of commercial systems available and its price is around 10€/ channel, which is cheaper compared to similar electronic systems.

As described in section 4.2, the SiPM matrix temperature is an important parameter. The PETsys system has the ability to monitor the temperature of the SiPM matrices and ASICS employed to control them. Temperature monitoring is important to ensure the correct functioning of both, photosensors and system. PETsys has the possibility of developing new function scripts to implement the stability gain method reported in section 4.2.

Although the TRITIUM monitor use SiPM matrices it is important to start the characterizaton at the level of a single channel (only one SiPM) to reduce the uncertainties in the first results. In order to do so, an electronic system was designed, developed and built to read up to eight different SiPMs and to monitor their temperature.

This system is based on three different PCBs<sup>13</sup>, shown in Figure 3.18 (electronical schemes shown in the appendix A):

1. The first PCB, shown in Figure 3.18a, is used to organize the SiPMs and sensor temperature. This PCB place up to 8 different SiPMs and a temperature sensor and arrange their output signals on two HDMI connections. This PCB is placed inside a special black box, from

---

<sup>12</sup> $1024 \cdot 16 = 16384$

<sup>13</sup>PCB, Printed Circuit Board

Thorlabs company [104], that has a high degree of light tightness. This black box has a small hole of 1 mm diameter, prepared to introduce an optical fiber<sup>14</sup> to illuminate SiPMs with an incoherent light source. The light source utilized is a LED, model 430L from Thorlabs company [106], which gives an spectrum shown in Figure 3.18d. The spectrum was experimentaly measured with a spectrometer and fitted to a Gaussian function. It can be seen that the emission peak of this LED is placed at 436.3 with a FWHM<sup>15</sup> of 19.1 nm. With the help of this LED we intend to simulate the light emission of the fibers of the TRITIUM experiment to calibrate the SiPMs at the working wavelength.

2. The second PCB, shown in Figure 3.18b, sums the different signals of the SiPMs and amplify them by a factor  $G = 4187.5$  or  $G = 10761.88$ , depending on the input resistance of the oscilloscope,  $50 \Omega$  or  $1 M\Omega$ , respectively. This PCB uses a differential amplification that reduce the electronic noise of the system and is connected to the first PCB through two HDMI feedthroughs.
3. The third PCB, shown in Figure 3.18c, rearranges all the different input and output signals in an HDMI connection to avoid crosstalk between different signals. This PCB is connected to the second PCB trough a HDMI feedthrough.

The input signals are the supply voltage of the SiPMs and the supply voltage of the PCBs ( $\pm 6$  V) and the output signals are the temperature sensor signal and the summed signal of all SiPMs.

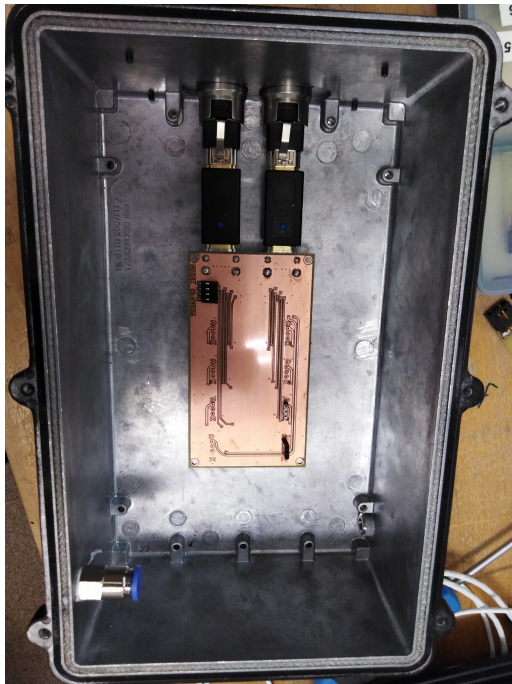
The output signal of the third PCB is connected to an oscilloscope, model ..., that records the data which are subsequently analized by ROOT<sup>16</sup>.

---

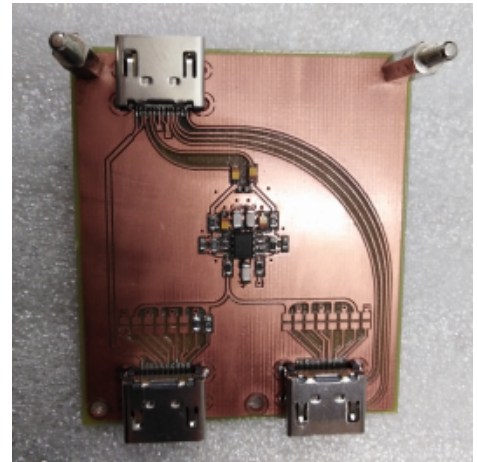
<sup>14</sup>The optical fiber used is BCF-98 from Saint-Gobain company [105]

<sup>15</sup>The FWHM parameter, Full Width at Half Maximum, of a Gaussian fit can be calculated from its sigma using the equation:  $FWHM = 2.35 \cdot \sigma$

<sup>16</sup>ROOT is a framework for data processing, based on C ++ and object-oriented



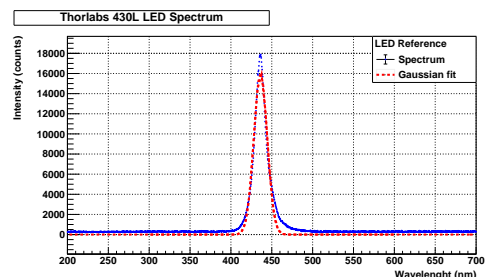
(a) PCB 1 used to arrange 8 SiPMs and black box.



(b) PCB 2 used to sum and amplify the output signals of SiPMs.



(c) PCB 3 used to rearrange the different signals of the system.



(d) Emission spectrum of the LED.

**Figura 3.18** – Three PCBs used for the SiPM characterization and LED emission spectrum.

## 3.3 Ultrapure Water System

### 3.3.1 Introduction to the Ultrapure Water System

The objective of the ultrapure water system is to purify the water sample before the measurement. This system is essential is important for two reasons:

1. The mean free path of tritium electrons in water is around  $5 \mu\text{m}$  and even less in solid materials like organic material. The electron from the tritium decay has to reach the fiber to be detected and, consequently, the detector must be kept very clean. If the analyzed water sample contains particles that may be deposited on the fibers, a layer of matter can be formed, preventing the tritium electrons from reaching the fibers and reducing drastically the tritium detection efficiency.
2. The tritium monitor does not have any spectrometric capabilities that can be used to distinguish other radioactive elements from tritium. That means that, any radioactive event in the analyzed water sample would be counted as a tritium event.

The ultrapure water system was designed to remove all particles up to a diameter of  $1 \mu\text{m}$  and organic matter, which means that the only radioactive particle that passes through it is tritium.

In summary, the ultrapure water system is used to keep our detector clean, ensuring the stability of its detection efficiency and to eliminate all radioactive particles other than tritium.

---

technology, developed at CERN and widely used in nuclear and particle physics.

### 3.3.2 Set Up of Ultrapure Water System

The requirements of this water treatment device are:

- to obtain a high degree of purification of the processed water sample, reducing its conductivity by approximately two orders of magnitude (from  $1000 \mu\text{S}/\text{cm}$  to  $10 \mu\text{S}/\text{cm}$ )
- to require of low maintenance (low cost and low manpower)
- to install a remote control device with probes and valves controlling by software.

The LARUEX laboratory in Extremadura, one of the six collaborators of the TRITIUM experiment, has designed, developed and built the ultrapure water system, a scheme of which is shown in Figure 3.19.

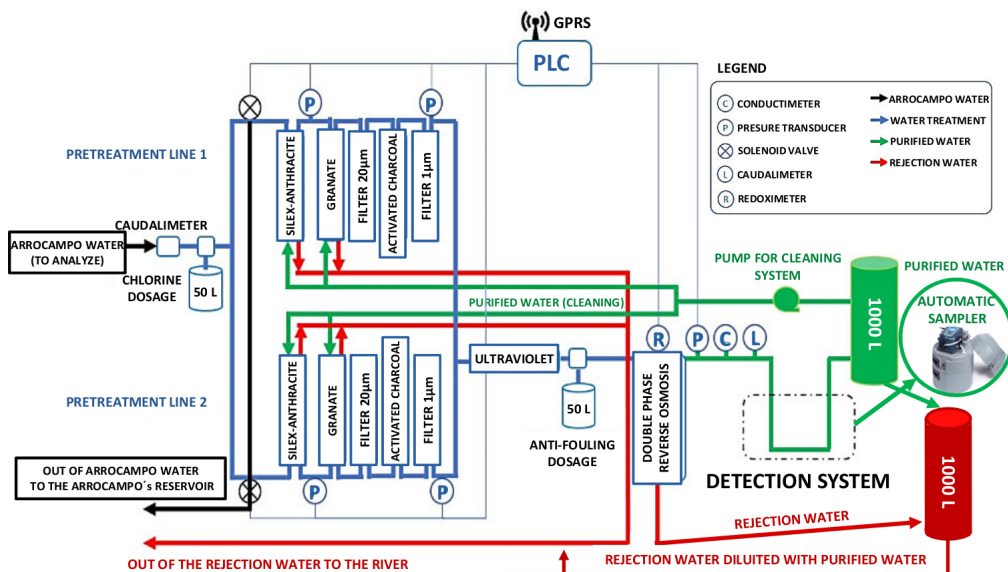


Figura 3.19 – Scheme of water purification system.

This system is installed in the Arrocampo dam and consists of four different consecutive stages:

1. The raw water from the Tagus River passes through two different filters, the first made of silex-anthracite and the second of garnet, with which a rough filtering is made (the largest particles are eliminated). This system has two parallel lines and implements self-cleaning by injecting ultrapure water in the opposite direction.
2. The outlet water sample of the first stage, called fine filtration stage, passes through a  $20\text{ }\mu\text{m}$  filter (formed by a synthetic mesh) and activated charcoal filters (one per line) that removes chlorine and iron particles.
3. The outlet water of the second stage passes through a super-fine filtering consisting of a  $1\text{ }\mu\text{m}$  filter, formed of a dense polypropylene mesh and UV lamps. The first filter removes all the particles up to diameters of  $1\text{ }\mu\text{m}$  and the UV lamps remove the organic matter present in the sample.
4. Finally, the water is introduced in the last stage, double-phase reverse osmosis, that reduces the conductivity of the water to about  $5\text{ }\mu\text{S}/\text{cm}$ . It was verified that a conductivity of  $10\text{ }\mu\text{S}/\text{cm}$  is achieved with only one module of reverse osmosis, enough for the needed conditions of tritium detector. Therefore, only one module of reverse osmosis is used for 24 h and the other, reducing the power consumption of the system.

As a result of the purification process, besides the ultrapure water that is introduced into TRITIUM detector, a rejection water, with conductivities greater than the original water containing the particles extracted from the ultrapure water is produced.

The ultrapure water system is able to process up to  $0.850 \text{ m}^3/\text{h}$  with a single line operating or  $1.480 \text{ m}^3/\text{h}$  with both, greatly overestimating the requirements of the tritium detector.

The software used for remote controlling of the ultrapure water system is Siemens PLC, that gives the information such as the state of the valves, the pressure probes or water production in real time.

The appendix B contains several pictures of different parts of this system, installed in Arrocampo dam.

### 3.4 Background Rejection System of TRITIUM Monitor

The objective of the background rejection system is to reduce the TRITIUM radioactive background. The TRITIUM project follows the ALARA principle for the tritium activity measurement, that is, to measure tritium activity "as low as reasonably achievable". The detection limit of tritium activity is set by the uncertainty in the activity of the radioactive background since tritium activities below this uncertainty cannot be distinguished from the background. Therefore, the background uncertainty must be reduced as much as possible.

The total uncertainty is a quadratic sum of all the different uncertainties related to the measurement, i. e., the statistical uncertainty<sup>17</sup>,  $\sigma_{st}$ , the systematic uncertainty<sup>18</sup>,  $\sigma_{si}$ .

The background rejection system of TRITIUM monitor minimizes the statistical component. Because of the Poissonian nature of the process,

---

<sup>17</sup>Uncertainty due to the statistical nature of the radioactivity process

<sup>18</sup>uncertainty due to the manufacture of the detectors

the statistical uncertainty corresponds to the square root of the measured activity,  $A_m$ , which can be reduced by minimizing detected background events.

$$\sigma_T^2 = \sigma_{st}^2 + \sigma_{si}^2; \quad \sigma_{st;bak} = \sqrt{A_{m;bak}} \quad (3.11)$$

The background of TRITIUM is due to natural radioactivity and has two different sources. On the one hand, radioactive elements that are present in the crust of Earth, mainly  $^{40}K$  and elements from the four different natural radioactive series, shown in Table 3.4. On the other hand, the cosmic ray radiation. The primary cosmic radiation is composed of high-energy particles, mainly protons and  $\alpha$ , but, after interacting with the Earth's atmosphere, they generate a shower mainly composed by muons, electrons, photons and neutrons mainly.

Mass Num.	Series	Prim. el.	Half life (y)	Final isotope
4n	Thorium	$^{232}\text{Th}$	$1.41 \cdot 10^{10}$	$^{208}\text{Pb}$
4n+1	Neptunium	$^{237}\text{Np}$	$2.14 \cdot 10^6$	$^{209}\text{Pb}$
4n+2	Uranium-Radium	$^{238}\text{U}$	$4.51 \cdot 10^9$	$^{206}\text{Pb}$
4n+3	Uranium-Actinium	$^{235}\text{U}$	$7.18 \cdot 10^8$	$^{204}\text{Pb}$

Table 3.4: Classification of natural radioactive series [107, 108].

Cosmic radiation depends on several parameter like the altitude and latitude of the Earth, the altitude, sea level in our case, and the solar activity cycle. The spatial distribution of cosmic rays, mainly muons, follows a  $\cos^2(\theta)$  distribution with the zenith angle.

To remove the effect of background two different techniques are employed:

- On the one hand, the weak radiation, which is any radiation with

energy below 200 MeV/nucleon is stopped by a lead castle, described in section 3.4.1,

- On the other hand, the hard radiation, that is any radiation of energy greater than 200 MeV/nucleon, is much more difficult to stop and the technique used is a cosmic veto, reported in section 3.4.2 in anti-coincidence with the TRITIUM detector.

### 3.4.1 Passive Shield (Lead)

Weak radiation is suppressed by a lead shielding inside which the TRITIUM detector is placed. This lead shielding is effective for particle energies below 200 MeV/nucleon, which is due to the Earth's natural radioactivity and to the weak component of cosmic radiation. This lead shielding consists of 158 lead bricks with ultra-low intrinsic radioactivity, 25 mm thick. They are chevron shaped, shown in Figure 3.20a, specially designed for a perfect fit and easy assembly. As can be seen in Figures 3.20b and 3.20c, these lead bricks are arranged in two layers to a total thickness of 50 mm. The junction of the inner layer lead bricks is shielded by a lead brick of the outer layer to avoid any leak of radiation.

Special aluminum structure was designed by mechanical engineering department of CENBG, shown in Figure 3.21, to support the total weight of the lead bricks, 2.4 tons.

The internal room of the lead shielding is divided in two parts, as exhibited in Figure 3.20. The larger one has internal dimensions of  $90.5 \cdot 41 \cdot 51$  cm<sup>3</sup> and is used to place the TRITIUM detector. The smaller one, of dimensions of  $33 \cdot 41 \cdot 51$  cm<sup>3</sup>, contains the DAQ system. The external dimensions of the lead shielding are  $148 \cdot 60 \cdot 70$  cm<sup>3</sup> and it weighs 2.5 tons.

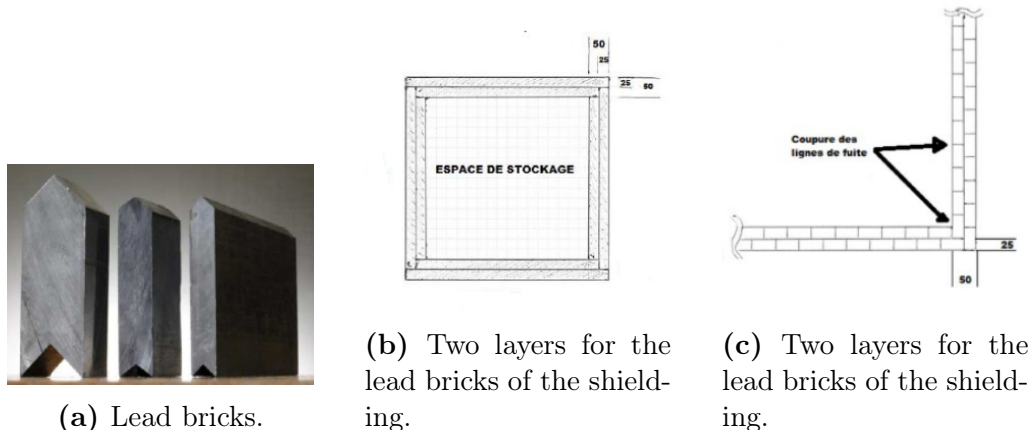


**Figura 3.20** – Lead Bricks and their arrangement in the lead shielding.

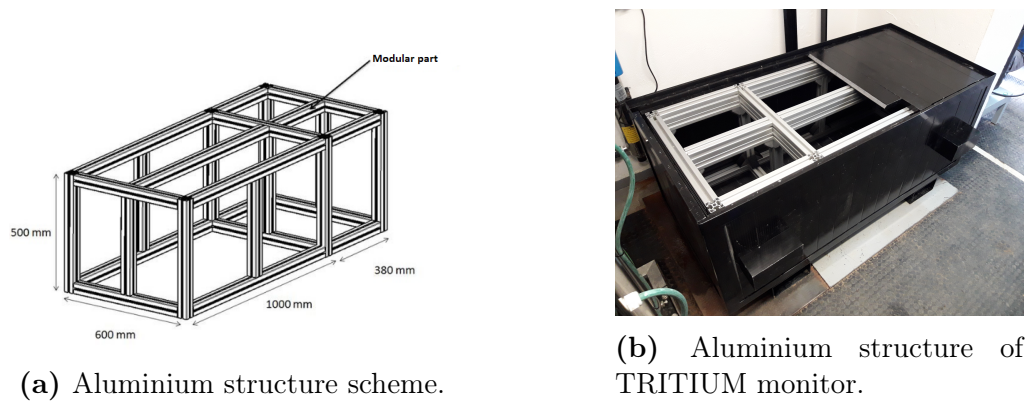


**Figura 3.21** – Lead Bricks and their arrangement in the lead shielding.

### 3.4.2 Active Shield (Cosmic Veto)

As hard radiation cannot be stopped by a moderate lead thickness cosmic vetos are employed.

A cosmic veto consists of at least two complementary detectors in coincidence that reject simultaneous events in both.

As shown in Figure 3.22, the two complementary detectors were placed one above and the other below the TRITIUM detector. The distance between both detectors, 34.2 cm for our latest prototype developed, is set by the TRITIUM prototype to be placed between both.

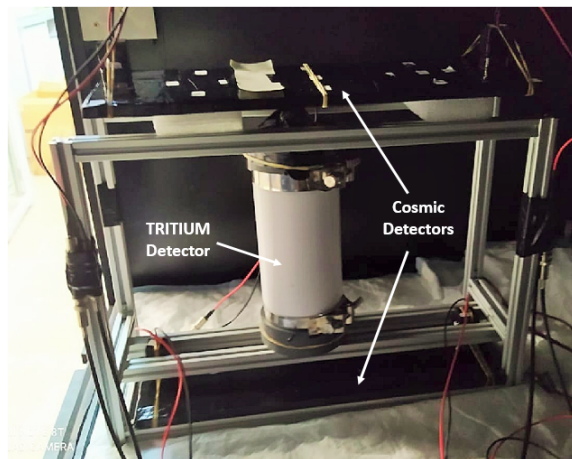


**Figura 3.22** – Cosmic veto and Tritium-IFIC 2 prototype in an aluminum mechanical structure developed by IFIC’s mechanical engineering department.

A hard cosmic events simultaneous through both cosmic detectors is displayed in figure 3.23a. Each cosmic detector has two photosensors. Hard cosmic events are rejected when both detectors are in coincidence with the electronic configuration given in Figure 3.14c.

The TRITIUM detector is read out in anti-coincidence with the

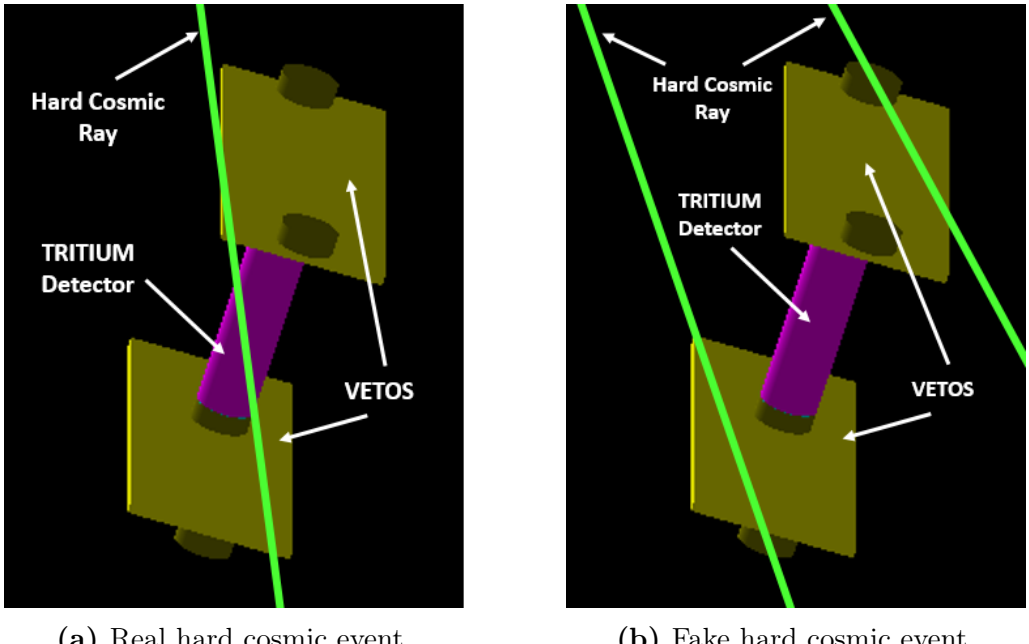


**Figura 3.23** – Hard cosmic events detected with the cosmic veto of TRIUM: a) Affecting to the tritium measurement, b) Does not affecting to the tritium measurement.

cosmic veto. Random coincidence from cosmic two different hard cosmic events, one in each detector, shown in Figure 3.23b are negligible. The expected hard cosmic rate at sea level for muons, main contributor, is  $70 \text{ m}^{-2}\text{s}^{-1}\text{sr}^{-1}$  [109, 110], that is  $7^{-3} \text{ cm}^{-2}\text{s}^{-1}\text{sr}^{-1}$ , shown in the cosmic rate plot of Figure 3.24. As time coincidences are triggered by logical gates of about 10 ns, the probability of recording two different hard cosmic events in temporal coincidence is less than  $10^{-9}$  which is not worth considering.

The vetos are made of a plastic scintillator block from Epic-Crystal [112]. Its properties are given in Table 3.5 and its energy emission spectrum is displayed in Figure 3.25.

The energy spectrum has a peak very close to that of the scintillating fibers used, so the same photosensors are used to read out them. The

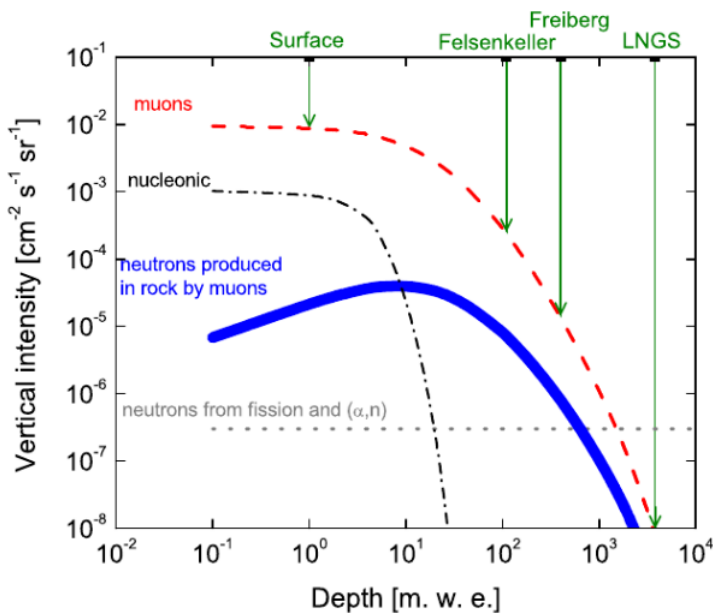


**Figura 3.24** – Hard cosmic muon rate [111].

dimensions of the scintillator block are  $45 \cdot 171 \text{ cm}^3$  and they are three foil wrapped by a layer of teflon, aluminum and black tape, exhibited in Figure 3.26. These layers prevent external photons from reaching the scintillator plastic and avoid photons generated by the scintillator plastic from escaping before reaching the photosensor. Two  $2.5 \cdot 2.5 \text{ cm}^2$  windows are made on the wrapping to allow reading by the photosensors.

As previously mentioned, the expected hard cosmic rate at sea level is  $7 \cdot 10^{-3} \text{ cm}^{-2} \text{s}^{-1} \text{sr}^{-1}$ . As the solid angle of our detectors is  $\omega = 0.5434$ , calculated by integrating the solid angle of one scintillator on the other, and the area of the veto is  $765 \text{ cm}^2$ , the expected hard cosmic rate on our cosmic vetos should be 2,909 event/s. Thus is important to determine the efficiency of the cosmic veto.

Base material	Polystyrene
Growth method	Polymeric
Density (g/cm <sup>3</sup> )	1.05
Refractive index	1.58
Soften temperature (°)	75-80
Light output (Anthracene)	50-60%
H/C ratio	1.1
Emission peak (nm)	415 (Blue)
Decay Time, (ns)	2.4
Hygroscopic	No

Table 3.5: Properties of plastic scintillators from Epic-Crystals. [112]

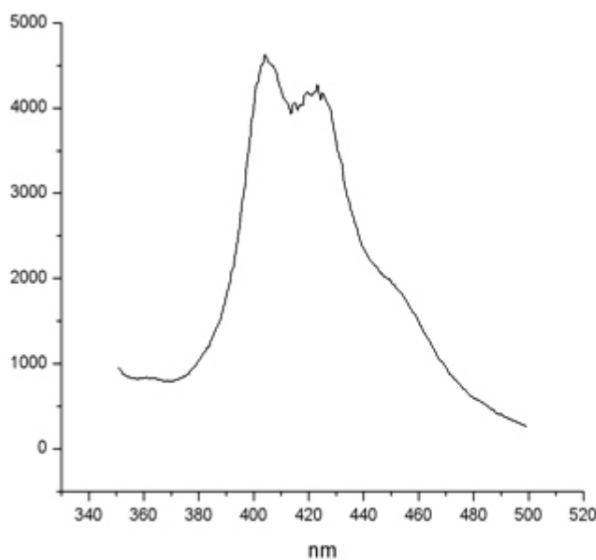
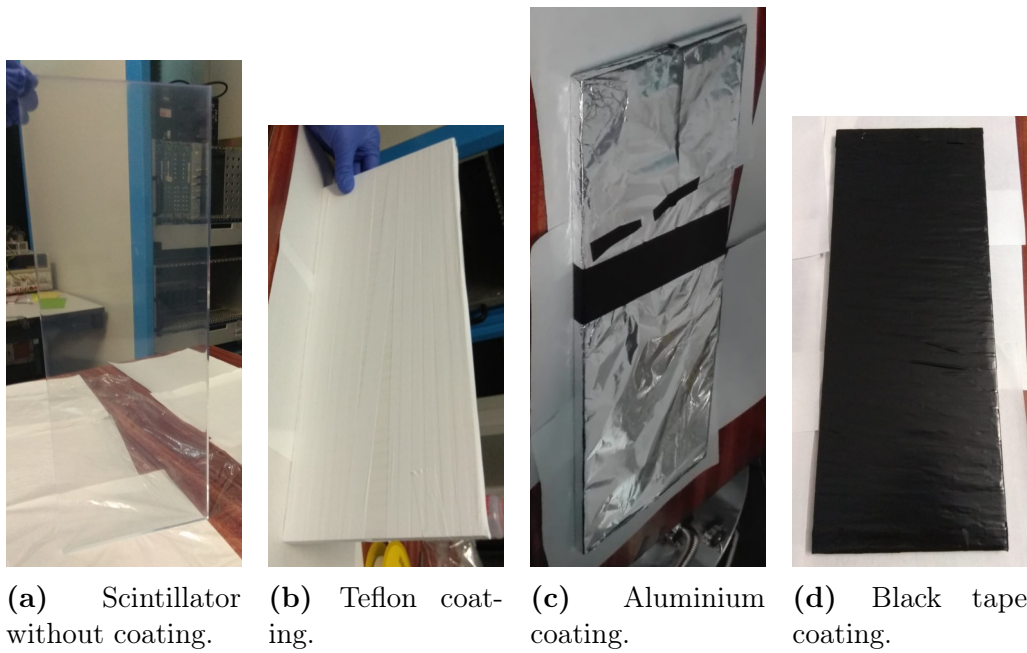


**Figura 3.25** – Emission energy spectrum of the plastic scintillation used for the cosmic vetos. [112]



(a) Scintillator without coating. (b) Teflon coating. (c) Aluminium coating. (d) Black tape coating.

**Figura 3.26** – Different layers used to cover of the cosmic veto.

# Chapter 4

## Research & Development on Detector Design and Components

This chapter describes the characterization of the different parts of the TRITIUM monitor, including scintillating fibers, SiPMs (at the individual SiPM level and at the matrix level), the ultrapure water system and the background rejection system. This characterization is crucial to understand their behaviour and the results of the monitor. Furthermore, several developments were made to improve fundamental parameters of the TRITIUM monitor components to enhance its sensitivity. All these studies were carried out inside a special light-tight box, black box, to ensure that the photons we are detecting come from the sources used, either LEDs or scintillators. In addition, as the energy response of plastic scintillators has a rather large uncertainty, most of the energy spectra are shown in ADC<sup>1</sup> channels, which are linearly proportional to energy.

---

<sup>1</sup>ADC units are the internal units, called channels, in which an analog signal is digitized after an Analog-to-Digital Converter. The number of available channels depends on the bits used in its digitization.

## 4.1 Characterization and R&D on Scintillating Fibers

This section reports experimental measurements of the scintillating fiber parameters that most affect the tritium detection, such as collection efficiency and conditioning uncertainty. Errors are included in all graphs displayed in this section but they are too small to be visible. Thousands of scintillating fibers are used in TRITIUM detector which were prepared and conditioned prior to characterization studies or tritium detection. Therefore, various mechanical and electronical devices were developed to automatically prepare many fibers at the same time.

### 4.1.1 Scintillating Fiber Conditioning Process.

The first step in TRITIUM design was to choose the optimal fiber length at which the signal of tritium events is optimal. On the one hand, long fibers are interesting because the efficiency of TRITIUM detector is proportional to the fiber length, but, on the other hand, in long fibers, scintillating photons are reflected on the fiber walls more times before reaching the photosensors, and, as some photons are lost in each reflection, the detector signal is deteriorated.

Several simulations were carried out using Geant4 [75], a particle and nuclear physics simulation package based on C++, to determine the optimal length. The result of these simulations, described in section 6.2.3, and displayed in section 8.1.3, Figure 8.7, was that it is preferable to work with short fibers.

The fiber length for the TRITIUM prototypes developed in Valencia, was 20 cm, which was also the length used for most of the experiments conducted in the framework of the TRITIUM experiment. As Saint-Gobain

commercial fibers are 1 meter long, an effective scintillator cutting technique had to be developed with strict requirements on the cutting quality of the fiber ends since this greatly affect the transmission of photons and, consequently, the efficiency of TRITIUM monitor. This cut must be perpendicular to the fiber and with very low uncertainty in the cutting position to achieve a good coupling of the fiber with the surface of the photosensor. It is also important that the fiber integrity be preserved, without cracks or deformations that contribute to the loss of photons.

Cutting the end faces of polymer fibers is one of current challenges. There are many different techniques such as milling, laser cutting, focused-ion-beam, blade cutting, etc. The blade cleaving technique was chosen for TRITIUM experiment because of its mechanical simplicity.

Many commercial devices based on blade cleaving, such as the one provided by thorlabs with a diamond tipped blade [113] or others similar to guillotine designed for industrial fiber optics [114], were tested in an extensive study with unsuccessful results [79]. As it can be seen in Figures 4.1, Commercial techniques produce deformations, cracks and imperfections so they do not fulfill the requirements previously imposed.

The microscope model PB 4161 from EUROMEX and the Digital Microscope from Jiusion company were used to check the results in the fiber ends.

Because commercial devices do not work for our scintillating fibers, a cutting device, shown in Figure 4.2, was designed, built and tested.

This device consists of fourteen rails to which the fibers are hold and a thin blade, fixed on a mobile piece, which is used to cut them. The perpendicular cut, which is one of the requirements, can be ensured since the moving piece, to which the blades are fixed, is set perpendicular to the fibers. The blade used is a typical commercial razor blade, of 0.1 mm thickness, which is the thickness that gave the best results. The blade was

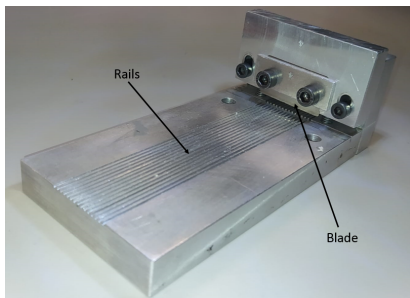


(a) Fiber end deformation.

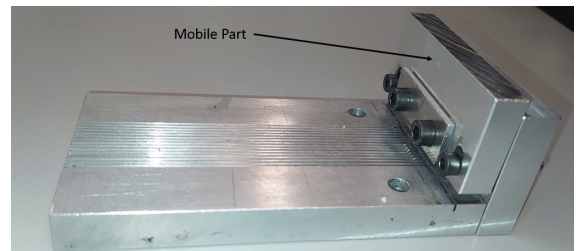


(b) Fiber end cracks.

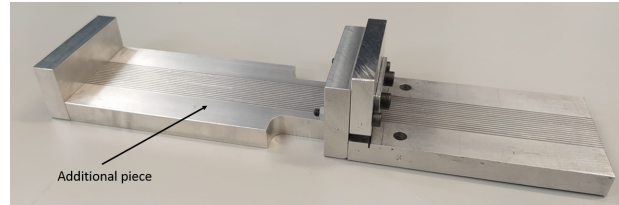
**Figura 4.1** – Unsuccessful results of using commercial techniques to cut fibers.



(a) TRITIUM Cutting device.



(b) TRITIUM Cutting device.



(c) Additional piece of TRITIUM cutting device.

**Figura 4.2** – Cutting device developed in the TRITIUM experiment and additional part to make precise measurements of fiber length.

adjusted with 5° tilt, with respect to the horizontal axis since it was found in several studies that this helps to obtain a less aggressive and cleaner cut [115, 116]. As it can be seen in Figure 4.3a, with this cutting device it was obtained fiber ends without breaks or deformation.

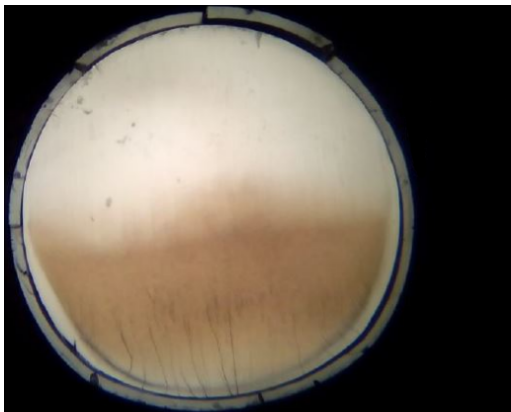
An additional parameter that could affect the cutting quality of the fiber ends is the temperature of both, the fiber and the blade. In a study in which both were subjected to different temperatures from room temperature to 110 degrees no significant conclusions were obtained [79]. Thus, the cutting process was carried out at room temperature to make the cutting easier.

To fix the fiber length to measure the fiber, which is the last requirement, an additional piece was designed and built, shown in Figure 4.2c. With the help of this piece an uncertainty in the fiber length of less than 1 millimeter was achieved. With the designed cutting fiber device we have fulfill all requirements imposed, obtaining fibers with optimal light transmission.

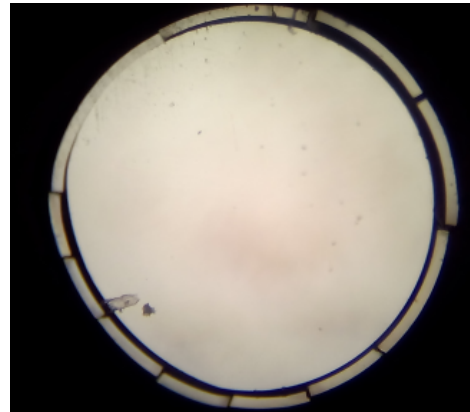
The fiber end after cutting is shown in Figure 4.3a. The slightly darkened zone at the bottom of the fiber is an inavoidable effect of the cutting process and, to reduce this flaw, a polishing process developed by Thorlabs was applied [113].

Five different polishing papers, with a decreasing grain size, 30  $\mu\text{m}$ , 20  $\mu\text{m}$ , 12  $\mu\text{m}$ , 5  $\mu\text{m}$  and 0.3  $\mu\text{m}$  respectively, were rubbed during two minutes with the fiber describing on the the paper a shape of 8 (approximately 120 movements).

The result obtained after polishing is shown in Figure 4.3b, where it can be noted that the darkened zone has completely disappeared and the fiber end is completely clear without any damage or imperfection. Therefore, both tasks, cutting and polishing, are necessary.



(a) Fiber end after cutting with Tritium device.



(b) Fiber end after cutting and polishing.

**Figura 4.3** – Result of the polishing process. a) Fiber end after cutting b) Fiber end after cutting and polishing with Thorlabs technique.

#### 4.1.2 Automatic Polishing Machine for Scintillating Fibers

As mentioned above, tens of thousands of fibers need to be prepared and conditioned for the TRITIUM monitor<sup>2</sup>, section 5.3. Although this amount of fibers was not a problem for cutting, which is very fast, the polishing process is quite time consuming. It takes more than ten minutes to polish each fiber, that would result in an unaffordable amount of time to prepare the needed amount of fibers. Therefore, an automatic polishing machine for scintillating fibers was designed, built and tested. This polishing machine is able to polish up to one hundred scintillating fibers at the same time and automatically. Furthermore, it is easily scalable to larger capacity.

This automatic polishing machine, displayed in Figure 4.4, consists of two parts: 1) A polishing table, where the fibers are polished 2) The electronics, based on Arduino technology, that operates the movement of the polishing table:

---

<sup>2</sup>Tritium prototype will be a module of TRITIUM monitor, based on dozens of modules.

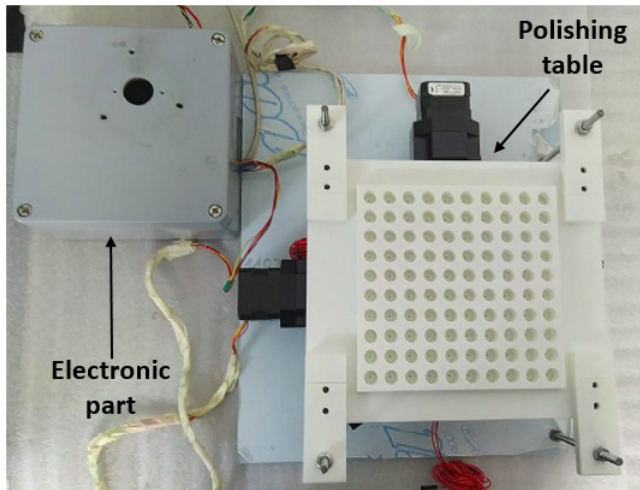


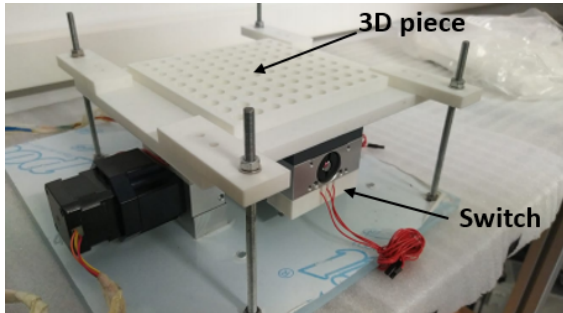
**Figura 4.4** – Polishing machine developed in TRITIUM experiment.

1. The polishing table, shown in Figure 4.5a, is divided in two parts: the static part, where the fibers are fixed, and the movable part, where the polishing papers are fixed. It was decided to set the polishing papers on the movable part because they are lighter and less fragile than fibers.

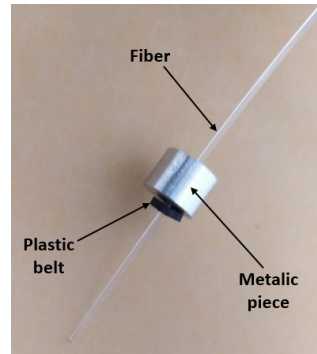
The static part consists of a piece, shown in Figure 4.5a, built with a 3D printer and fixed to the system by four vertical screws. On each screw there are two nuts to set the relative height and the inclination of fibers to the polishing papers. This piece contains one hundred holes in which the fibers are placed.

The own weight of fibers press the polishing paper. As they are too light (0.16 g), a plastic belt and a piece of metal with a weight of around 1.5 g, shown in Figure 4.5b, is employed to increase their weight (in the same way as in Thorlabs polishing process).

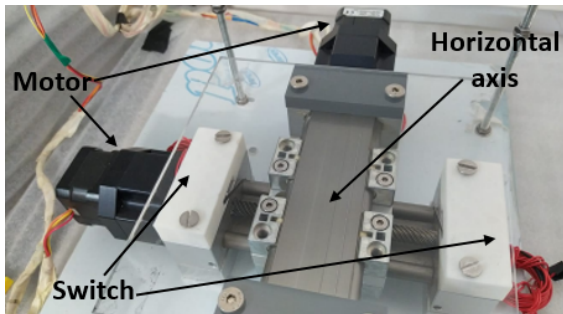
The movable part consists of a flat PMMA plate of  $18 \times 18 \text{ cm}^2$  to which the polishing paper is attached. This part is locked to two horizontal screws, perpendicular to each other that are used to set its position in the XY plane (horizontal plane), as shown in Figure 4.5c.



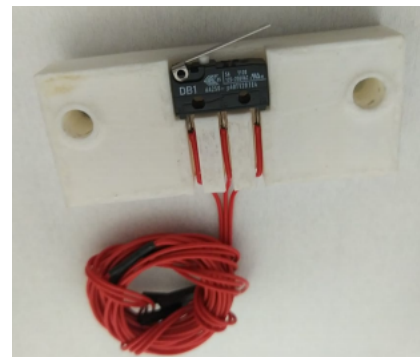
(a) Polishing table.



(b) Fiber with metal piece.



(c) Horizontal screws and PMMA plate.



(d) Piece to hold switches.

**Figura 4.5 – Polishing table of the polishing machine**

The polishing system contains several switches, mounted on a piece made by a 3D printer, shown in Figures 4.5a, 4.5c and 4.5d, which are used to find the origin of coordinates when the system is reinitiated and to stop the movable part when the end of the path is reached.

2. The electronics, shown in Figure 4.6, is based on Arduino technology which controls the automatic movement of the polishing paper.

The electronics consists of two stepper motors, model NEMA ST4209S1404-A [117], which move the horizontal screws on which the polishing paper is attached. These motors are controlled by an Arduino UNO [118] that uses a CNC shield [119] in which two different drivers are

connected to control the stepper motors, one driver for each stepper motor.

Drivers are controllers that allow to manage stepper motors in a simple way. It is very important to choose the correct controller for the system because the controller limits the supply power to the motors, avoiding burning of the motors in the worst case. Instead of using the Pololu A4988 drivers [120], which is one of the most widely used drivers, the first choice was the DRV8825 driver [121]. DRV8825 allows to power the motor with higher voltage and intensities (45 V and 2.5 A) than A4988 (35 V and 2 A). Also, the DRV8825 controller includes a new microstepping mode (1/32) compared to the A4988 (1/16) with which we get more accurate and smooth movements. Finally the drivers were replaced by the TMC2208 [122], much less noisy since it includes the *StealthChop* function with which the noise is practically eliminated. Furthermore, this controller is much more accurate as it has a microstepping mode of 1/256. The voltage and current used to power the motors are 35 V and 2 A which is sufficient for the whole system since the current of the motors is limited to 1.33 A. The excess current will be transformed into heat that has to be dissipated from the system. Overheating of the drivers may cause loss of steps, producing different movements from those programmed or even destroying the driver. Therefore, a cooling system is needed to ensure the correct operation of the polishing system. The cooling system, shown in Figure 4.6, consists of a copper piece<sup>3</sup> in contact with both controllers and a fan, used to prevent heat accumulation inside the electronics box. The cooling power can be improved by using a PELTIER cell.

This polishing machine is controlled by a computer using the Universal G-code Sender software (a grafical interface based on the GRBL package). There are several useful pre-programmed functions such as "HOME"

---

<sup>3</sup>The copper is one of the best thermal conductor at STP

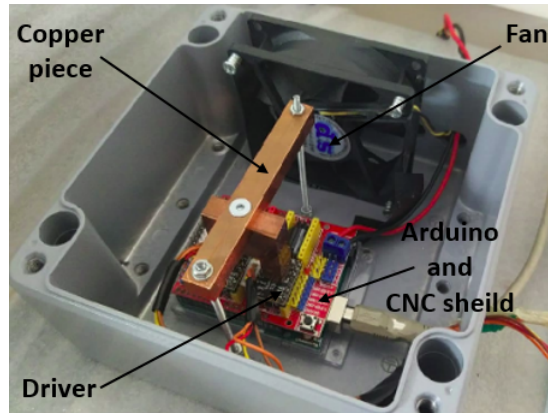


**Figura 4.6** – Electronic system of Polishing machine.

with which the system, using the switches, finds its origin coordinate every time the system is turned on.

The software also has the possibility of loading a file containing the g-code to be executed, In the TRITIUM, the 120 movements required for each polishing paper are loaded in this way.

This machine was tested with twenty fibers of 15 cm length arranged in a bundle. The fibers were fixed to the structure shown in Figure 4.7 and two PMTs located at the bundle ends, read in coincidence as described in section 3.2.4, Figure 3.14b.

Two different measurements were taken using two different radioactive sources, a  $^{60}\text{Co}$  gamma source of 715 Bq activity, and a  $^{90}\text{Sr}$  beta source of 17.8 kBq activity. After, the fiber bundle was polished and the test was repeated.

The energy spectra recorded for both radioactive source are exhibited in Figure 4.8. The sources were placed in the middle of the fiber bundle, at 7.5 cm from each PMT.

As it can be seen in Figure 4.8, both energy spectra are shifted to

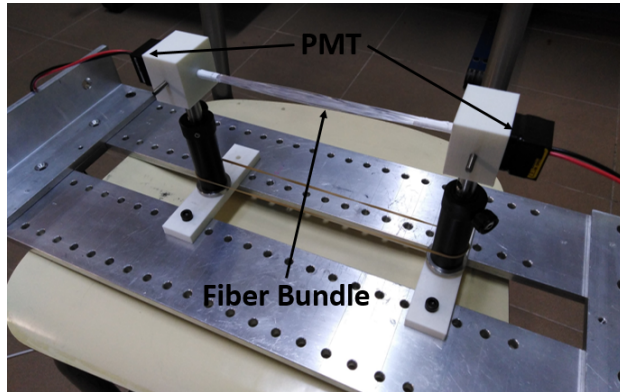


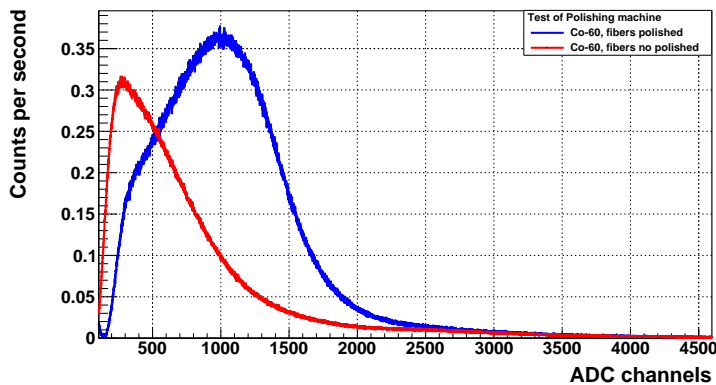
**Figura 4.7** – Set up used to test the effect of the polishing machine.

the right after polishing fibers, which means that the detected events have more energy (more photons per event reach the PMTs). This energy increase was more than 40% ( $(42 \pm 4.6)\%$  for gamma source and  $(49 \pm 8.4)\%$  for beta source) with respect the unpolished fiber. In summary, with the polishing machine, the photon collection efficiency of the fibers was improved (mainly due to the improvement of the interface between fibers and PMTs). It is very important to achieve a high detection efficiency as the expected number of photons per tritium event is quite low.

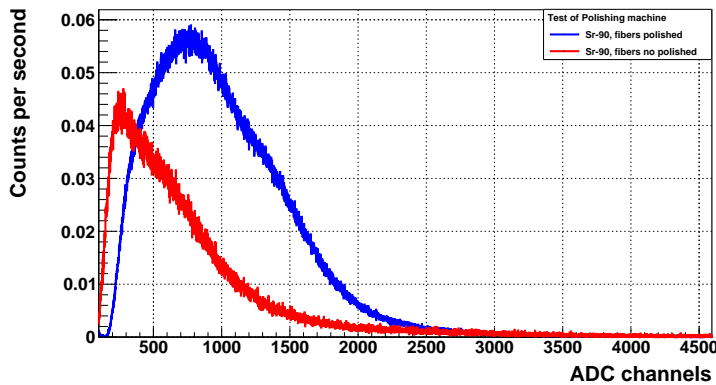
#### 4.1.3 Characterization of Scintillating Fibers

This section describes the characterization of uncoated BCF-12 fibers, called no-clad fibers, from Saint-Gobain, which are the fibers selected for the TRITIUM experiment. These fibers are compared to single clad and multiclaid BCF-12 fibers to quantify the influence of the clad in the relevant parameters of the scintillating fibers.

Although commercial clads are too thick for the TRITIUM experiment, the necessary low thickness clads could be developed. For example, clads with a thickness of the order of tens of nanometers can be achieved



(a) Energy spectrum recorded for the Co-60 source.



(b) Energy spectrum recorded for the Sr-90 source.

**Figura 4.8** – Energy spectrums used to test the effect of the Polishing machine

by electrodeposition techniques.

The difference between these three types of fibers is that no clad fibers only consist of a polystyrene core with a refractive index of 1.60 whereas, single clad fibers, have an acrylic clad (PMMA) of 30  $\mu\text{m}$  thickness and a refractive index of 1.49 and, multiclad fibers, have a second fluor-acrylic clad of 10  $\mu\text{m}$  thickness and a refractive index of 1.42.

This characterization was carried out for a single scintillating fiber. The parameters measured for each fiber type were the fiber collection efficiency and the uncertainty of the fiber response due to the conditioning process. The reference magnitude employed for the characterization is the rate of photons that reach the active area of the photosensor. To measure this magnitude, a calibrated R8520-06SEL PMT was used, whose quantum efficiency at the working wavelength, 29.76%, was measured by Hamamatsu. The PCB described in section 3.2.4 worked without the PMT internal gain and the PMT output current was measured by a Keithley 6487 Picoammeter/Voltage Source. The photons rate was obtained from the current measurement using the equation 3.10 with  $QE = 0.2976$  and  $CE = 1$ . A simplified scheme of the used set up is shown in Figure 4.9.

This setup consists of an optical structure in which a LED and a PMT are fixed to a user set distance between them. A LED435-03 LED from Roithner LaserTechnik GmbH [123], simulated the light emission by the fibers. The emission spectrum of the LED, given in Figure 4.10, was experimentaly measured by a spectrometer and fitted to a Gaussian function. The LED emission peak is at 433.9 nm with a FWHM of 18.4 nm.

The fiber was fixed between the LED and the PMT. The length of the fiber was 20 cm. Optical grease [125] was used for optimal coupling between the fiber and the PMT. Two collimators were used to ensure that only photons detected from the LED were detected in the PMT. Two FH-

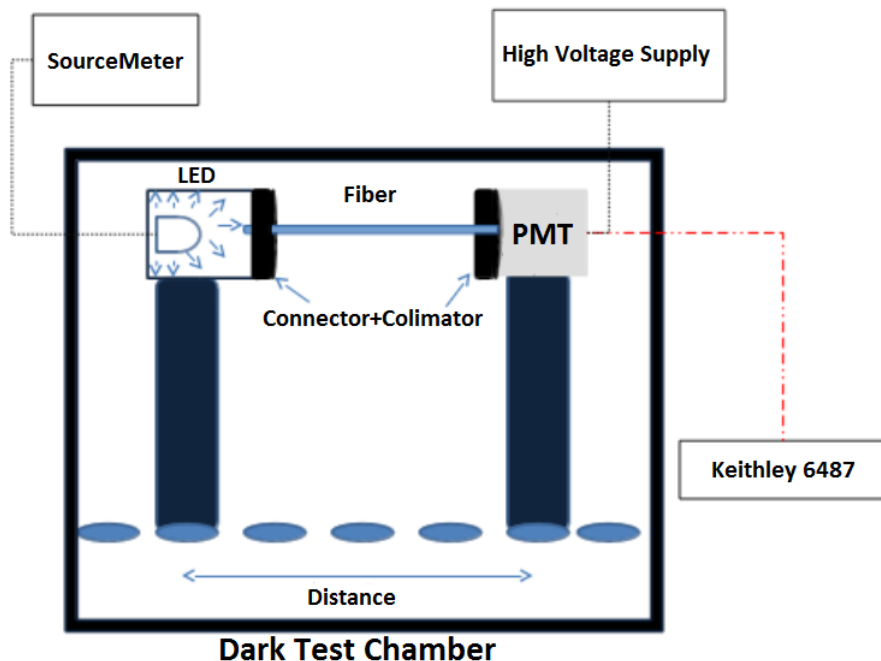


**Figura 4.9** – Set up used for fiber characterization.

ST<sup>4</sup> connectors from RoHS company [], were used to fix the fiber to the system.

### Preparation of the Characterization System.

Before characterizing a fiber several tasks had to be performed to check that the black box was light-tight and the PMT response was lineal.

A light leak in the black box would produce a background larger than the signal. To check the light-tightness a no-clad fiber of 20 cm length was fixed in the previous assembly. The LED was fed with four different intensities (0.05 mA, 0.1 mA, 0.15 mA and 0.2 mA) and the PMT response was measured with and without a special black blanket from Thorlabs [126],

---

<sup>4</sup>FH-ST is a quick assembly connector for 1 mm POF

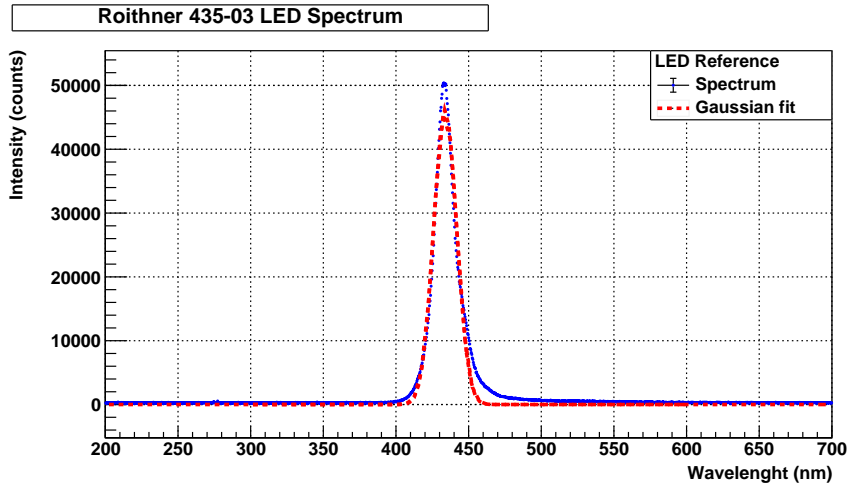


**Figura 4.10** – Emission spectrum measured for the LED model 435-03 from Roithner LaserTechnik GmbH Company.

that prevents external photons to reach the system.

This test was repeated for three different fibers and the mean and standard deviation of the light output were calculated by:

$$\bar{x} = \frac{\sum_{i=0}^N x_i}{N}; \quad \sigma = \frac{\sqrt{\sum_{i=0}^N (x_i - \bar{x})^2}}{N-1}; \quad (4.1)$$

The difference of the PMT responses in both cases is presented in Figure 4.11. As it can be seen in this figure, there are no statistically relevant differences between covered and uncovered fiber. Therefore, the light tightness of the black box is sufficient for this study.

The optimal voltage of the PCB without the internal gain was obtained by finding the voltage plateau in which the electron collection efficiency in the first dynode was practically 100%. The LED was fed at 1 mA intensity without any fiber and the PMT output current was measured for different PMT supply voltages, between 0 and 500 V. The number of

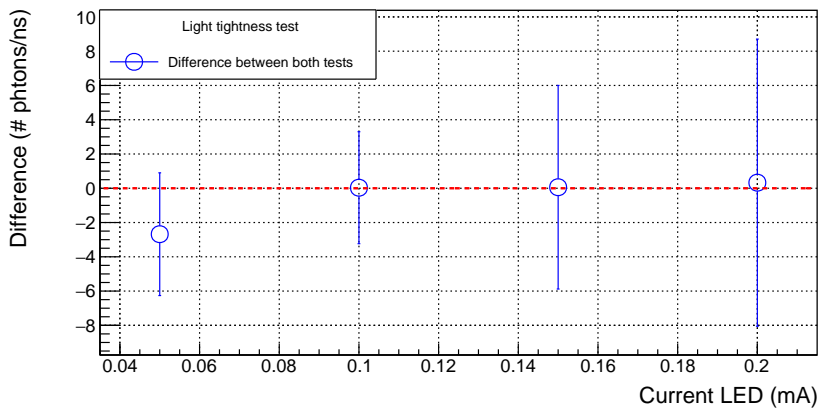


**Figura 4.11** – Difference between the results obtained in both tests carried out to check the light-tight quality of the system.

photons detected by the PMT is plotted in Figure 4.12. As it can be seen, the plateau is located at voltages higher than 150 V, where the PMT output response is stable. The chosen voltage at which the characterization was carried out was 250 V.

Finally, the linearity of the PMT was verified. The LED was powered with intensities ranging from 0 to 10 mA (LED linearity range) to check that the LED emission light do not saturate. The linearity was tested in the range of the number of photons expected in a tritium event (a few tens of photons per tritium event, tens of photons per nanosecond) and in the range of up to two thousand five hundred photons per nanosecond.

To test the linearity of the PMT in the range of tritium events, the set up described above was used without any fiber and one of the connectors but the collimators was kept to make sure that the active area of the PMT is the same as the use in the characterization study.

To test the linearity of the PMT at the level of more than a thousand photons per nanosecond, we removed the remaining connector in order

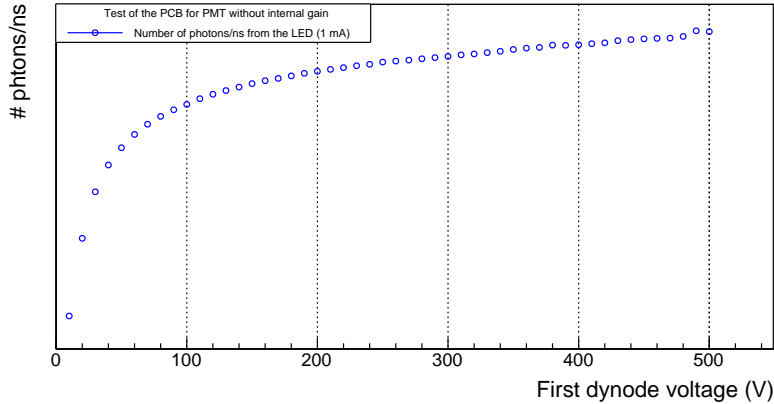


**Figura 4.12** – Response of the PMT as a function of its high voltage using the designed PCB with which no internal gain of the PMT is obtained.

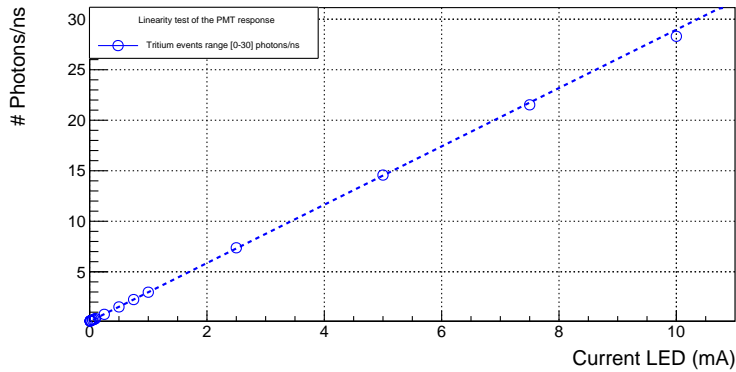
to increase the photons that reach the photosensor and the collimators was also kept.

The results for both intensity ranges are shown in Figures 4.13. As it can be seen, the PMT output current is linear in both intensity ranges.

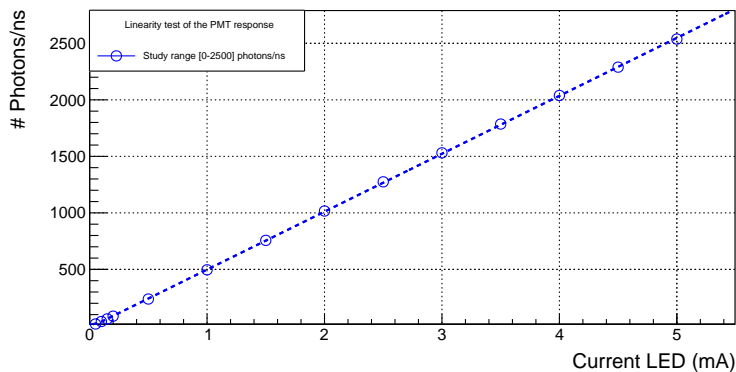
## Results of the Characterization of Scintillating Fibers

The conditioning process, consisting of cutting and polishing the fibers, is an individual task that generates a small dispersion in the response of each individual fiber,  $\sigma_{con}$ . This is an uncertainty that will be present in the tritium measurement of the monitor.

To measure this dispersion, it has to be taken into account that the position of the connectors that lock the fiber in the experimental setup produce an additional uncertainty,  $\sigma_{pos}$ , in the measurement. Since both uncertainties are independent, the total uncertainty is given by:



- (a) Response of the PMT in the intensity range of tritium events. Error bars are smaller than the point size.



- (b) Response of the PMT in the range  $[0 - 2500]$   $\gamma/\text{ns}$ . Error bars are smaller than the point size.

**Figura 4.13** – Linearity tests of the PMT response

$$\sigma_t = \sqrt{\sigma_{pos}^2 + \sigma_{con}^2} \quad (4.2)$$

The uncertainty due to the fiber position has to be quantified to extract from the total uncertainty. Two different experiments were designed, the first with only the uncertainty in the fiber position ( $\sigma_t = \sigma_{pos}$ ), and the second with both uncertainties. The conditioning uncertainty is given by:

$$\sigma_{con} = \sqrt{\sigma_{tot}^2 - \sigma_{pos}^2} \quad (4.3)$$

The test designed to measure  $\sigma_{pos}$  consisted of preparing one fiber of each type (uncladded, single clad and multiclad) by the conditioning process reported above. Each fiber was locked in the set up, and a measurement by feeding the LED with an intensity of 0.1 mA was done. These measurements were repeated ten times with the same fiber. Ten different measurements for each fiber type was obtained. The standard deviation of the set of measurements is only due to the position uncertainty. The results are shown in Table 4.1.

$$\sigma_{pos}^{rel} = \frac{\sigma_{pos}}{\bar{x}} \quad (4.4)$$

Fiber type	Mean ( $\gamma/\text{ns}$ )	$\sigma_{pos}$ ( $\gamma/\text{ns}$ )	$\sigma_{pos}^{rel}$ (%)
Uncladded	$524.088 \pm 0.010$	17.65	3.37
Single Clad	$1071.696 \pm 0.01$	9.07	0.85
Multiclad	$949.930 \pm 0.026$	9.91	1.04

Table 4.1: Mean and standard deviation (due to fiber position in the setup) of photons per nanosecond that reach the PMT for 0.1 mA LED intensity.

As it can be seen, the clad reduces the position uncertainty, which means that it improves the uniformity of the fiber response. It was also

found that the clad markedly improves the light collection efficiency of the fibers. The reason could be because photons are mainly collected in the core of the fiber and the interface of core and is better defined in the case of a single clad or multiclads fibers than for uncladded fibers. In the latter case, the interface is provided by the environment (air or water in the case of TRITIUM), and external conditions, as dirt, may produce noticeable interface fluctuations.

It is also seen that a second clad slightly reduce the collection efficiency. The reason could be that a second clad layer reduces the fiber core proportionally.

Concerning the error of the measurement, the error of the Keithley device was three orders of magnitude smaller than the standard deviation, and it was not taken into account.

To determinate the whole uncertainty, ten different samples of each fiber type were prepared and each fiber was measured under the same conditions as the previous test. This measurement was done for four different LED emission intensities (0.05, 0.1, 0.15 and 0.2 mA) to reduce possible mistakes. The results of uncladded fibers are plotted in Figure 4.14, where it can be seen that, although each fiber shows a very linear trend with the amount of collected photons, a dispersion in the fiber response is clearly seen. Similar results were obtained for single clad and multiclads fibers, displayed in figures 4.15b and 4.15c respectively.

The average number of collected photons versus LED intensity for each type of fiber is given in Tables 4.2, 4.3 and 4.4 and represented in Figure 4.16, where they can be compared.

As it can be noticed in Figures 4.14 and 4.15 the fiber response is quite linear and that single clad and multiclads fibers have stronger signals than uncladded fibers, which means that the clad has a significant effect on the fiber collection efficiency. Also, it was found that single-clad fibers have

Led Int. (mA)	Average ( $\gamma/\text{ns}$ )	Std. Des. ( $\gamma/\text{ns}$ )	Rel. Std. Des. (%)
0.05	243.46	9.82	4.03
0.1	540.62	33.51	6.20
0.15	902.74	36.83	4.08
0.2	1252.62	50.48	4.03

Table 4.2: Number of the collected photons versus LED intensity for 10 different samples of uncladded fibers.

Led Int. (mA)	Average ( $\gamma/\text{ns}$ )	Std. Des. ( $\gamma/\text{ns}$ )	Rel. Std. Des. (%)
0.05	383.81	33.23	8.66
0.1	922.68	73.97	8.02
0.15	1485.10	119.90	8.07
0.2	2053.78	166.39	8.10

Table 4.3: Number of the collected photons versus LED intensity for 10 different samples of single clad fibers.

Led Int. (mA)	Average ( $\gamma/\text{ns}$ )	Std. Des. ( $\gamma/\text{ns}$ )	Rel. Std. Des. (%)
0.05	376.68	14.96	3.97
0.1	870.87	34.58	3.97
0.15	1396.60	55.24	3.95
0.2	1932.57	76.02	3.93

Table 4.4: Number of the collected photons versus LED intensity for 10 different samples of multi clad fibers.

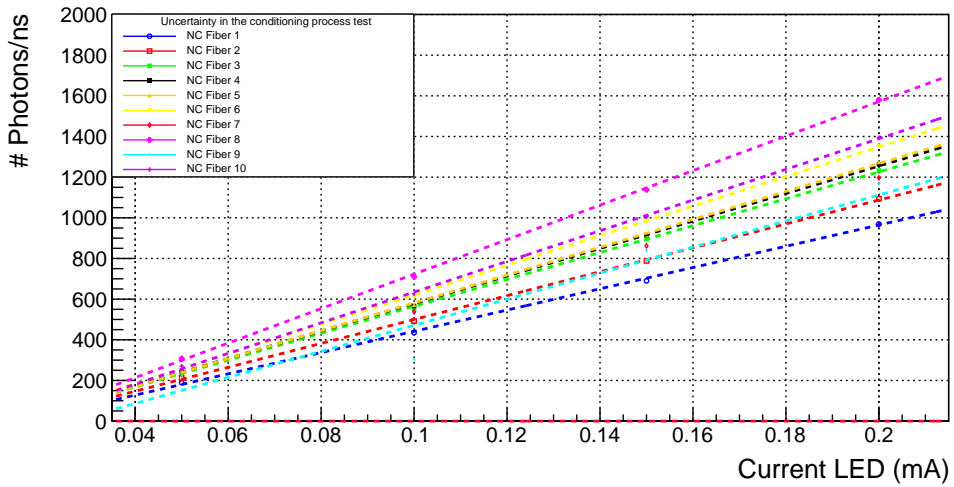


**Figura 4.14** – Number of photons/ns reaching the PMT for Uncladded fibers.

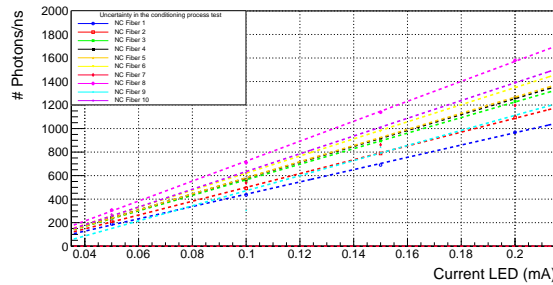
higher collection efficiency than multicladi fibers. It can also be remarked in Table ?? that the relative standard deviation,  $\sigma_{pos}^{rel}$ , does not vary with the LED intensity.

An average of the uncertainty due to the fiber position and the conditioning process are given in Table 4.5.

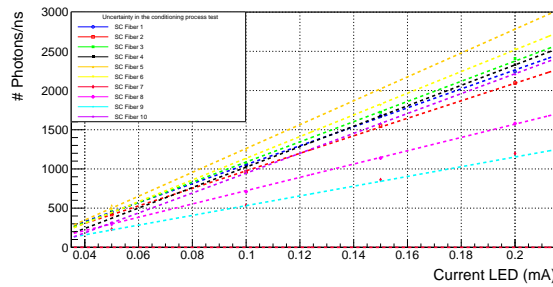
Fiber type	$\sigma_t$ (%)	$\sigma_{pos}$ (%)	$\sigma_{con}$ (%)
Uncladded	4.01	3.37	2.17
Single Clad	8.21	2.17	7.92
Multicladi	3.96	1.04	3.82

Table 4.5: Relative standard deviations ( $\sigma_t$ ,  $\sigma_{pos}$  and  $\sigma_{con}$ ) measured in this test.

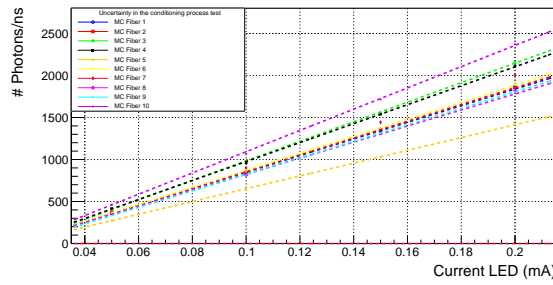
As it can be seen, the smallest uncertainty in the conditioning process was found in the uncladded fibers, which means that the damage



(a) Number of photons/ns reaching the PMT for unclad fibers.



(b) Number of photons/ns reaching the PMT for Single Clad fibers.



(c) Number of photons/ns reaching the PMT for MultiClad fibers.

**Figura 4.15** – Number of photons/ns reaching the PMT for ten samples of each fibers type.

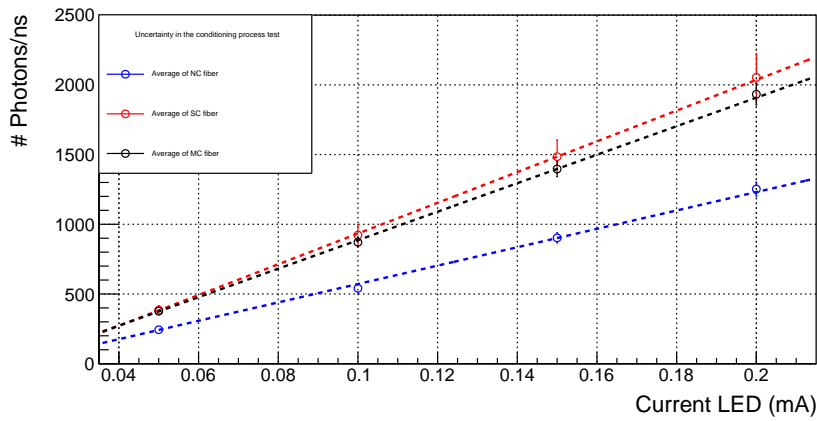


**Figura 4.16** – Average of 10 samples for each fiber type (unclad, single clad and multiclad fibers).

from this process occurs mainly in the fiber clad, as can be checked in Figure 4.3. It was checked under the microscope that this damage only occurs at the end of the fiber. Also, the largest relative standard deviation in this process is measured for single clad fibers, which means that the second clad increases the resistance of the fiber to the conditioning process.

In summary, this study has shown that the use of fiber clad improves the photon collection efficiency. The relative statistical deviation due to the fiber conditioning process was quantified for the different fiber types. It was found that the damage of the conditioning process is produced mainly in the fiber clad. Thus, if a method to build a clad for fibers is developed, it should be applied after the fiber conditioning process.

Finally, the measurement of the photon collection efficiency of each type of fiber is shown. The collection efficiency is the percentage of photons collected along the fibers. It is usually given by 1 m fiber length,  $CE_{100}$ .

To measure the collection efficiency,  $CE_{100}$ , ten different samples 10 cm length was prepared for each fiber type. The results are given in

Table 4.6.

Led Int. (mA)	Uncladded ( $\gamma/\text{ns}$ )	Single clad ( $\gamma/\text{ns}$ )	MultiClad ( $\gamma/\text{ns}$ )
0.05	$318.35 \pm 61.34$	$549.62 \pm 70.79$	$480.35 \pm 83.72$
0.1	$735.65 \pm 143.02$	$1269.91 \pm 164.32$	$1110.66 \pm 193.44$
0.15	$1183.91 \pm 232.07$	$1983.93 \pm 230.97$	$1777.40 \pm 307.19$
0.2	$1645.18 \pm 323.76$	$2506.97 \pm 208.01$	$2338.43 \pm 350.24$

Table 4.6: Number of the collected photons versus LED intesntity for 10 different fibers of 10 cm length.

The collection efficiency in 10 cm fiber length,  $CE_{10}$ , was calculated by comparing these tests with those performed for a fiber length of 20 cm and the collection efficiency,  $CE_{100}$ , was calculated from  $CE_{10}$  by assuming a linear deppendance on length.

Fiber type	$CE_{10}$ (%)	$CE_{100}$ (%)
UnCladded	$75.97 \pm 7.61$	$7.597 \pm 0.761$
Single Clad	$77.96 \pm 5.66$	$7.796 \pm 0.566$
Multiclad	$82.60 \pm 7.24$	$8.260 \pm 0.724$

Table 4.7: Collection efficiencies  $CE_{10}$  and  $CE_{100}$ .

The collection efficiency,  $CE_{100}$ , given by the manufacturer Saint-Gobain is between 7% and 3.44% [78]. As collimated photons were used in this study, the fact that our results are in the best side is justified. As it can be seen in Table 4.7, our measured values are very close to those provided by the manufacturer.

#### 4.1.4 Cleaning Process for Scintillating Fibers

The tritium events detected in the fibers produce a few photons, so it is very important to conserve as many photons as possible. As it was shown

in the fiber characterization study, the quality of the interface between the core of unclad fibers and the environment (tritiated water in the case of TRITIUM detector) conspicuously affects the photon collection efficiency. To improve the quality of the interface a fiber cleaning process, ALGO to remove external particles deposited on the fibers, such as dust and fat that worsen the photon collection efficiency. Through this cleaning process, the wetting property of the fibers, illustrated in Figure 4.17, is improved, preventing air molecules from attaching to the fiber and achieving a uniform water clad around the fibers, which results in an improvement of their collection efficiency.

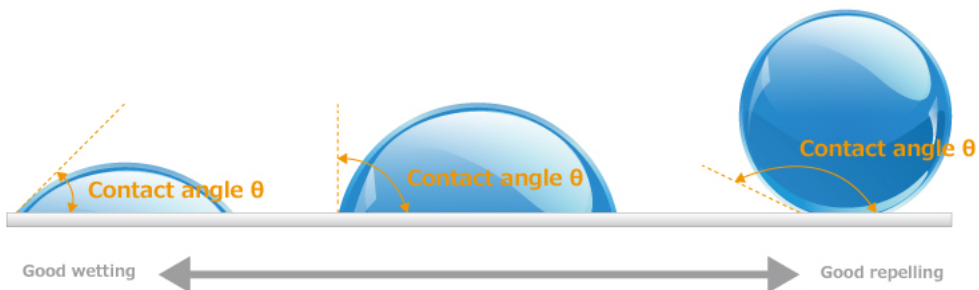


**Figura 4.17** – Wetting property produced by the cleaning process. [127]

This cleaning process was developed and carried out in the clean room of ICMOL laboratory<sup>5</sup>. It consists of filling three different glass beakers, one with alkaline soap, another with millipore water<sup>6</sup> and the last one with isopropanol. First, the fibers are rubbed for 5 minutes with alkaline soap and then placed in the first beaker for sonication for 3 minutes. Then, the fibers are cleaned with a constant flow of water for 5 minutes. Second, the fibers are placed in the second beaker for sonication for another 3 minutes. Third, the fibers are placed in the third beaker for sonication

<sup>5</sup>ICMOL, Institute of Molecular Science, is a research institute located in the Science Park of the University of Valencia.

<sup>6</sup>The millipore water is water in which all the ions were removed, producing a very low conductivity of it-self, on the order of  $10 \mu\text{Sv}/\text{cm}^2$

for another 3 minutes. Finally the fibers are dried with an N<sub>2</sub> air gun and introduced inside of the prototype.

The improvement in fiber response was verified using a bundle of twenty fibers of 15 cm length that was prepared with the conditioning process described. This bundle of fibers was arranged in the setup described in section 4.1.2, Figure 4.7, and several energy spectra were taken using different radioactive sources. Then, these fibers were cleaned with the fiber cleaning process and these measurement was repeated in the same conditions.

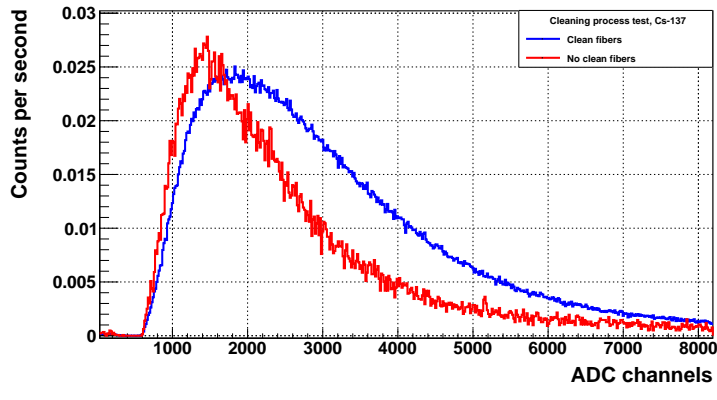
Two radioactive sources were used in this study, the <sup>90</sup>Sr beta source, used in the polishing machine test, and the <sup>137</sup>Cs gamma source, of 500 Bq activity. The results are shown in Figures 4.18, where a shift of the spectrum to higher energies can be noticed.

This improvement was estimated by:

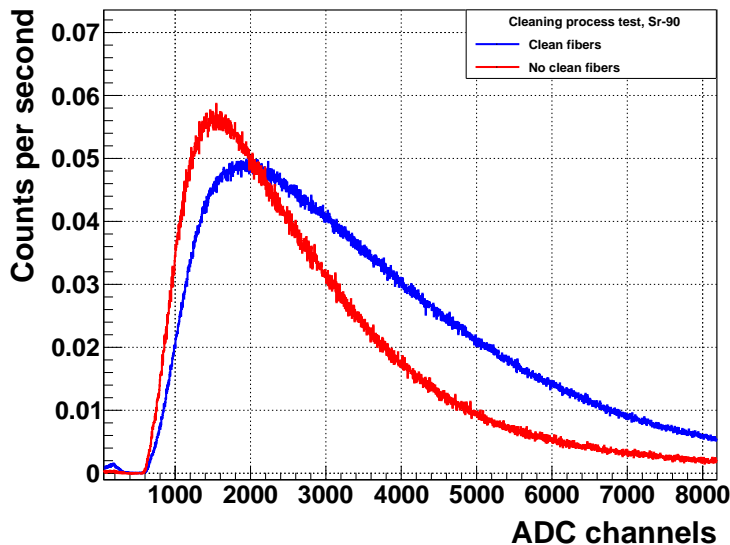
$$F = \frac{A_C - A_{NC}}{A_C} \quad (4.5)$$

where  $A_C$  is the integral of the energy spectrum measured after the cleaning process and  $A_{NC}$  is the integral of the energy spectrum measured before the cleaning process.

The F obtained is about 21% for both radioactive sources. Nevertheless, it should be taken into account that this test was carried out in air which may give somewhat different results than in water.



(a) Energy spectra recorded for the Cs-137 source.



(b) Energy spectra recorded for the Sr-90 source.

**Figura 4.18** – Energy spectra obtained before and after the cleaning process

## 4.2 Characterization and R&D on SiPM

### 4.3 Characterization of the Ultrapure Water System

This section describes the characterization of the ultrapure water system, employed to ensure that the quality of the water sample used to be measured fulfills the requirements of the TRITIUM detector. There are three different requirements that this ultrapure water system must satisfy:

1. A quite low conductivity<sup>7</sup> of the water, around  $10 \mu\text{Sv}/\text{cm}$ , to avoid that external particles dissolved in the water be deposited on the fibers, drastically reducing the detector efficiency.
2. The radioactive particles (other than tritium isotope) from the water sample should be removed because tritium cannot be separated from other radioactive isotopes.
3. Lastly, the tritium activity should not be affected by the water purification process.

To verify that these requirements are complied with, a characterization of the water sample for both, raw water and purified water, was done. This characterization consisted of measuring the water sample conductivity and the activity of the different radioactive element present in the sample. The turbidity and the chemical components of the water sample were also measured. The sample of the raw water was taken at 40 meters from the ultrapure water system and two meters deep in the river. Variations of up

---

<sup>7</sup>Conductivity is the ability of a material to conduct electrical current. In liquids, conductivity is related to the presence of salts (presence of positive and negative ions)

to 25% in the tritium activity was measured between both points (due to the diffusion of tritium along the river).

The chemical composition of the water was measured before the ultra-purification process by a physico-chemical analysis, shown in Table 4.8.

Chemical components	Concentration (mg/L)
$\text{CO}_3\text{H}^-$	154
Mg	46
Ca	105
$\text{NO}_3^-$	16
$\text{Cl}^-$	196
$\text{NO}_2^-$	0.03
K	11
Na	173
$\text{SO}_4^-$	217
Dry Residue	1029

Table 4.8: Chemical components and turbidity measured in the raw water sample.

The water sample contains a number of components given in the Table, that must be removed to prevent their deposition on the scintillating fibers of the detector, that would reduce their sensitivity to tritium activity.

The water turbidity<sup>8</sup> was measured using the Hanna Hi 9829 portable multiparameter system from Hanna Instruments [128], obtaining a value of 29 NTU, much higher than the WHO recommended limit of 5 NTU.

The water conductivity was measured for both, raw and purified water. The same system, the Hanna Hi 9829, was employed. The results of

---

<sup>8</sup>The turbidity of water is the loss of transparency due to dissolved particles, normally measured in Nephelometric Units of Turbidity, NTU, as the intensity of scattered light at 90 degrees.

these measurements, together with the measurement of the conductivity of rejected water, described in section 3.3.2, are presented in Table 4.9.

Date	Raw ( $\mu\text{Sv}/\text{cm}$ )	Pure ( $\mu\text{Sv}/\text{cm}$ )	Reject ( $\mu\text{Sv}/\text{cm}$ )
1/8/18	970	11.85	1442
7/8/18	958	11.8	1632
14/8/18	966	12.04	1725
22/8/18	980	12.54	1702
28/8/18	987	9.9	1692
5/9/18	1009	12.02	1645

Table 4.9: Measurements of the conductivity for several samples of water.

As it can be seen in the first column, the raw water sample has high values of conductivity, due to its content of ions, as shown in Table 4.8. It can be noticed in the second column of the table that the conductivity of pure water was reduced by almost two orders of magnitude, to values close to  $10 \mu\text{Sv}/\text{cm}$ , fulfilling the requirement. In the third column, it can be remarked that the rejected water conductivity is higher than that of raw water, because this water contains the removed ions from pure water.

The gamma radioactive elements present in both, raw water and purified water, were identified and their activities measured by a HPGe, high purity germanium detector. A gamma analysis was carried out to determine the emitters with long enough lifetime to be measured. The radioactive isotopes found in the raw water sample with measurable activities were  $^{40}\text{K}$  and  $^{226}\text{Ra}$  which were completely removed in the purified water.

The tritium activity was measured by liquid scintillation counting (LSC) to find its modification by the ultra-purification process. The raw water was filtered at 0.45 microns to remove any particles that could cause the extinction of the scintillation signal. Table 4.10 show several measurements of the tritium activity for different water samples before and after purification. As it is see, tritium activity is not affected by the purification

process.

Date	Raw (Bq/L)	Pure (Bq/L)
7/8/18	$24 \pm 3$	$26 \pm 4$
11/12/19	$13.2 \pm 2.1$	$13.85 \pm 2.2$
15/01/20	$30.6 \pm 4.2$	$30 \pm 4$

Table 4.10: Measurements of the tritium activity for several samples of both, raw and pure water.

## 4.4 Characterization of the TRITIUM Cosmic Veto

This last section reports on the characterization of the active shield (cosmic veto), which was carried out using PMTs as photosensors. Measurements of the cosmic veto using SiPM arrays has already started and their replacement will be as soon as possible.

The veto coverage, shown in Figure 3.26, was verified. This study was done at the level of one detector so the configuration of the electronics is the one shown in Figure 3.14c. The surface of the veto was divided in 9 parts, shown in Figure 4.19, in which a gamma source was placed.

Two different tests were made for this task:

1. The first test was used to quantify the improvement of the veto signal due to its coverage. A  $^{137}\text{Cs}$  source was placed at point 2 and a energy spectrum was measured with the veto uncovered. Next, the measurement was repeated with the veto covered. The result is shown in Figure 4.20.

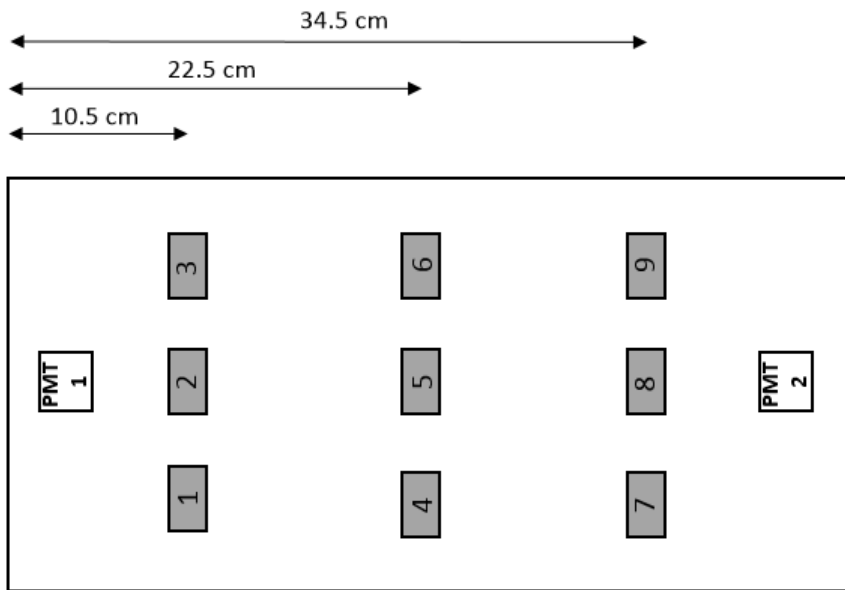


**Figura 4.19** – Reference points used for veto mapping.

The spectrum is shifted to the right, which means that more photons have been collected per event. No improvement was obtained in the number of events detected, only in the collection efficiency.

2. The second test was done to verify the spatial uniformity of the signal in the covered veto. For this task, a mapping was carried out, which consisted of placing a  $^{60}\text{Co}$  source at each point and measuring the number of events detected in the same time window. This test was done for two different veto modules and the energy spectrum obtained was integrated. The count rate obtained in each point is displayed in Table 4.11 for both vetos. The values are plotted in Figures 4.21a and 4.21b, respectively.

It can be observed that the veto signal has a uniform response on its surface, giving a fairly similar counting rate in all the points considered.

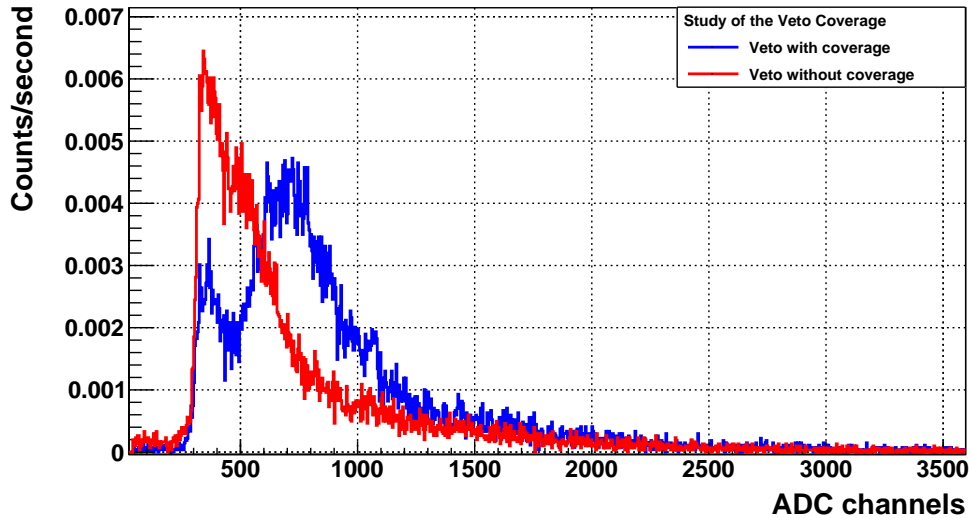
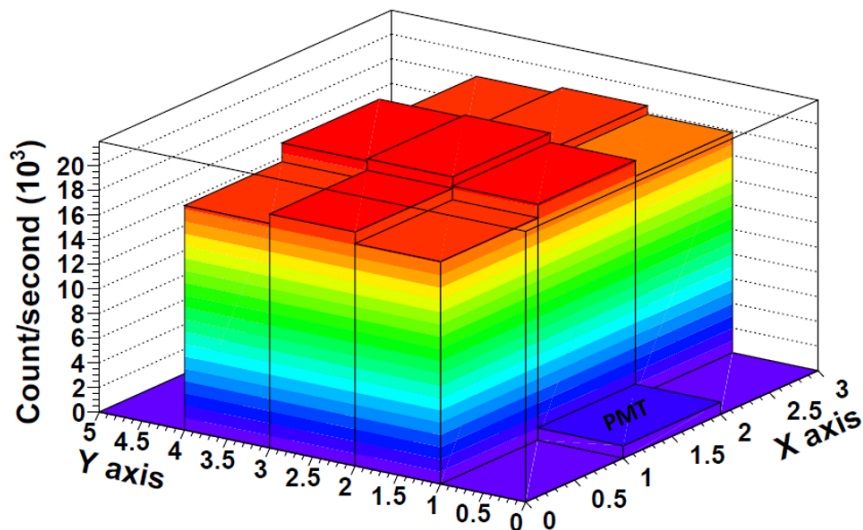


**Figura 4.20** – Measurement of a radioactive source  $^{137}\text{Cs}$  with the TRI-TIUM cosmic detector with and without its coverage.

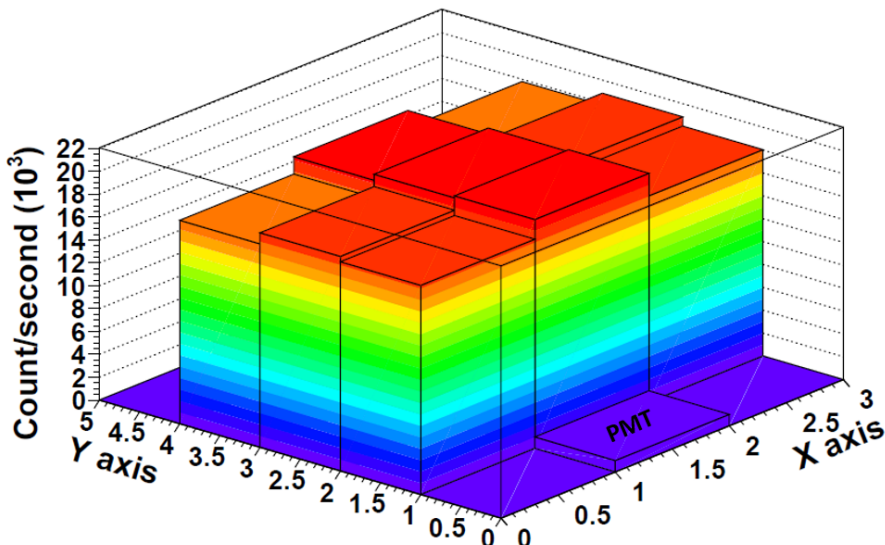
The following studies of this section were done at the level of a cosmic veto (both detectors in coincidence), so the configuration of the electronics was that of Figure 3.14c. The following step is to find the conditions in which the detection of cosmic events is optimized. This optimization consists of, on the one hand, finding the minimum high voltage of PMTs for which their efficiency is stable, and, on the other hand, finding the maximum threshold of the discriminator<sup>9</sup> at which this starts to loss cosmic events. For a higher high voltage and a smaller threshold, a plateau of the counting rate should be found.

The counting rate was measured for several high voltages at fixed threshold and for several thresholds at fixed high voltage. Both measurements are shown in Figure 4.22. To find the optimal conditions the amplification line of the configuration of the electronics 3.14c was eliminated and

<sup>9</sup>The threshold is the voltage value that the PMT output signals must exceed to contribute to the cosmic detection



(a) Mapping of the first TRITIUM cosmic detector.



(b) Mapping of the second TRITIUM cosmic detector.

**Figura 4.21** – Bidimensional graph of the count rate (Mapping) measured with two different TRITIUM cosmic detectors using a radioactive source of  $^{60}\text{Co}$ .

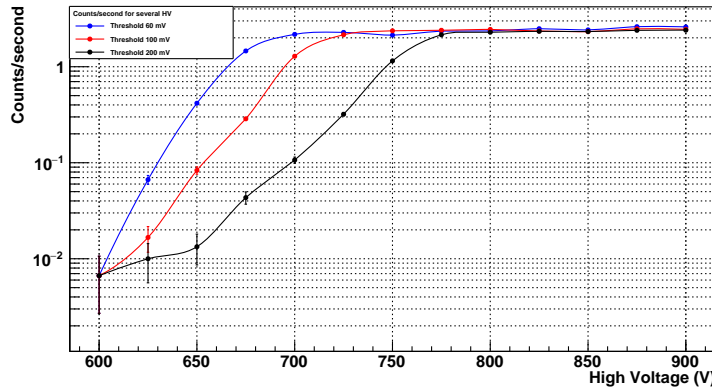
Point	Veto 1 (counts/s)	Veto 2 (counts/s)
1	$18028 \pm 3$	$18293 \pm 1.5$
2	$19133 \pm 5$	$20014 \pm 4$
3	$17858 \pm 4$	$18843 \pm 4$
4	$18969 \pm 5$	$18761 \pm 5$
5	$19893 \pm 4$	$19841 \pm 3$
6	$18573 \pm 4$	$18850 \pm 5$
7	$18200 \pm 4$	$17790 \pm 4$
8	$19725 \pm 4$	$19312 \pm 4$
9	$18030 \pm 5$	$17804 \pm 5$

Table 4.11: Count rate measured with two different cosmic detectors using a radioactive source  $^{60}\text{Co}$ .

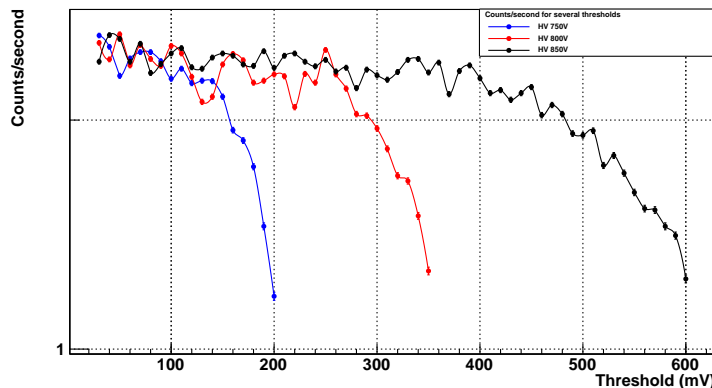
the output signal of the coincidence module was connected to a CAEN Quad Scaler And Preset Counter-Timer module, N. 1145, [129]. The counting rate was measured in a time window of 300 s.

In Figure 4.22a, the measurements at several high voltage is exhibited, which was done for three different thresholds, 60 mV, 100 mV and 200 mV. As it can be observed, there is a minimum high voltage for each threshold, 700 V, 730 V and 780 V respectively, at which the plateau start. This minimum voltage is higher when the value of the threshold is increased, as it should happen. The voltage chosen was 800 V since it is on the plateau for the three thresholds. Analogously, the counting rate for several thresholds and fixed high voltage was measured for three different high voltages, 750 V, 800 V and 850 V, which is plotted in Figure 4.22b. There is a maximum threshold for every high voltage used, 140 mV, 270 mV and 450 mV respectively, at which the plateau ends. This maximum threshold increases with high voltage, as it should happen. The threshold chosen was 200 mV which is on the plateau for the selected high voltage, 800 V.

Next, the energy spectrum of cosmic events was measured, which



(a) Counting rate as a function of high voltage for three different thresholds.



(b) Counting rate as a function of threshold for three different high voltage.

**Figura 4.22** – Counting rate as a function of high voltage for fixed thresholds and as a function of thresholds for fixed high voltage.

is shown in Figure 4.23. For this task, the configuration of the electronics is given in Figure 3.14c for 800 V and 200 mV of HV and threshold, respectively.

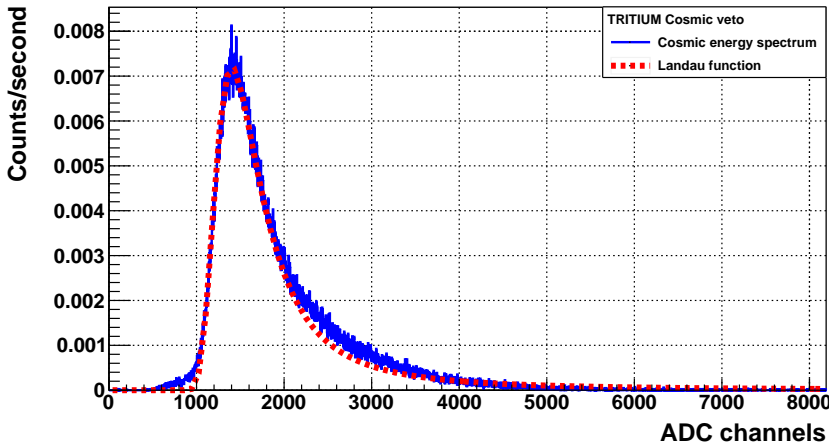
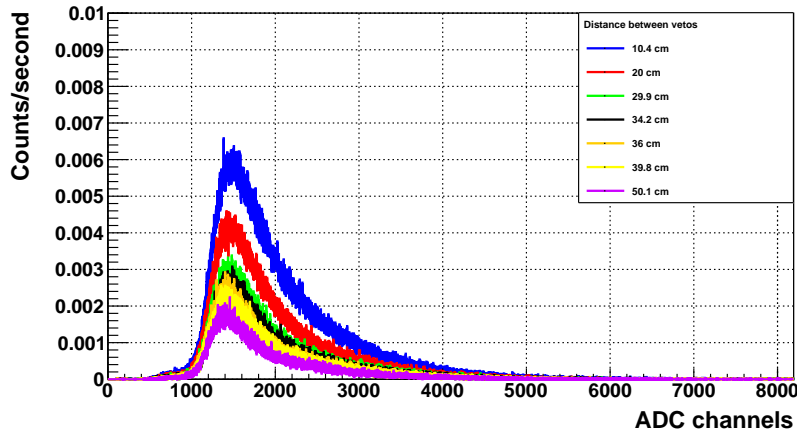


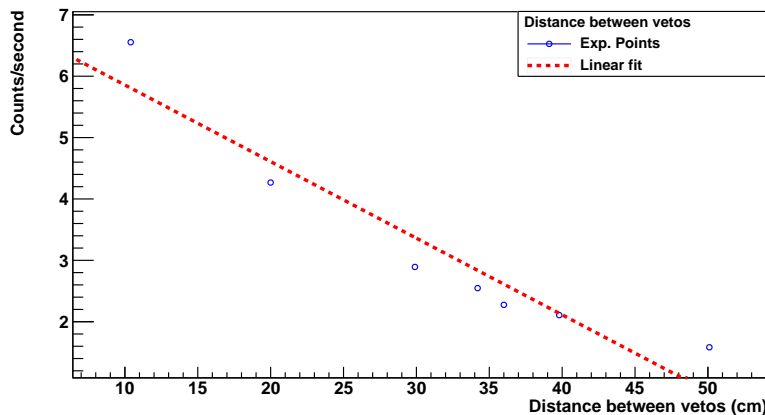
**Figura 4.23** – Energy spectrum measured with the cosmic veto.

As it is expected, this energy spectrum fits well to a landau function. The cosmic ray rate can be determined from the area of this spectrum, which is 2,5 event/s. The expected cosmic rate, calculated in section 3.4.2, is 2,9 event/s, so the efficiency of the active veto developed in TRITIUM experiment for cosmic events detection is 85%, which is a usual value for the efficiency of plastic detectors.

Finally the relationship between the detected cosmic ray rate and the distance between the two plastics of the cosmic veto was obtained. The energy spectrum was measured for five different distances, namely 10 cm, 20 cm, 36 cm, 40 cm and 50 cm. The spectra are plotted in Figure 4.24a. The energy spectrum of Figure 4.23 was also included. As can be seen, the counting rate decreases with the distance but the spectrum shape remains the same. The integrated spectra as a function of distance, plotted in Figure 4.24b, show an approximately LINEAR behaviour. This LINEAR fit allows to estimate the cosmic rate if the veto distance is changed.



(a) Energy spectrum of the cosmic veto for several distance.



(b) Linear fit of counts per second measured with the cosmic veto for several distance.

**Figura 4.24** – Measurement of the cosmic veto for several distances between its cosmic detectors.



# Chapter 5

## TRITIUM Monitor Prototypes

This chapter describes the different prototypes that was developed in the framework of the TRITIUM experiment, which are TRITIUM-IFIC 0, TRITIUM-IFIC 1, TRITIUM Aveiro 0 and TRITIUM-IFIC 2, listed in chronological order of their construction.

The first two prototypes built are preliminary prototypes used to learn about tritium detection and to detect and solve problems in their designs.

The other two prototypes built are prototypes with a well-defined design in which no problems were found. They were built to check more subtle effects.

Each prototype was designed and built in the laboratories of the university (IFIC, Valencia or Aveiro, Portugal) and it was filled with tritiated water following a protocol specially developed for this task, described in appendix C. Several water tightness and filling tests were carried out in each prototype to guarantee its radiosecurity.

Finally, the final monitor of TRITIUM detector will be explained.

It is based on modular detection units for easy scalability, where each module is the chosen prototype (the one with the best results).

## 5.1 Preliminary IFIC prototypes, TRITIUM-IFIC 0 and TRITIUM-IFIC 1

Two preliminary prototypes, TRITIUM-IFIC 0 and TRITIUM-IFIC 1, are shown in this section, which were designed, developed and built at the IFIC workshop.

These prototypes were thought to be a small scale of the final TRITIUM detector module and they were used to learn about tritium detection, to detect possible problems in their designs and to verify the improvements applied to them.

### 5.1.1 TRITIUM-IFIC 0

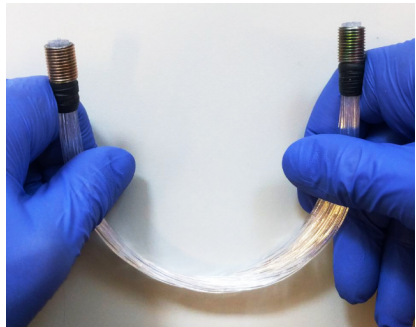
The TRITIUM-IFIC 0 prototype was the first prototype developed in TRITIUM experiment and it was used to check the feasibility of the technology proposed by TRITIUM, that's, to verify that it is possible to detect tritium in water using scintillating fibers.

Due to the problems that arise when liquid radioactive sources are used, the design of this first prototype paid special attention to radiation safety, rather than in detecting tritium efficiency.

The TRITIUM-IFIC 0 consists of bundle of 35 fibers, shown in Figure 5.1, with a length of 20 cm, which were cut and polished with the techniques explained in section 4.1.1. This bundle has a metallic pieze located in both ends, shown in Figure 5.1a, which are used to fix it to the



(a) Metallic piece of the fiber bundle.



(b) Fiber bundle in a position similar to the prototype.



(c) Bundle of fibers in a straight position.

**Figura 5.1** – Bundle of 35 fibers, the length of which is 20 cm, used in TRITIUM-IFIC 0 prototype

prototype.

This bundle is placed inside of a vessel, whose material is PVC<sup>1</sup> since it is a safe material widely used. This vessel, shown in Figure 5.2, was designed in a U-shape to improve the radiological safety, although this shape worsen the efficiency of tritium detection.

As can be seen in Figure 5.2, a piece of methacrylate and steel was designed and built to hold the detector and two calibrated PMTs were optically coupled directly to the fiber bundle ends using optical grease [125].

The employed PMTs were the model R8520-460 from Hamamatsu company [81], whose reference number are ZB2771 and ZB2773, and the electronic circuit, shown in figure 3.9, was used to distributed the high voltage between the dynodes. The employed high voltage was  $-800$  V, at

---

<sup>1</sup>Polyvinyl Chloride, PVC

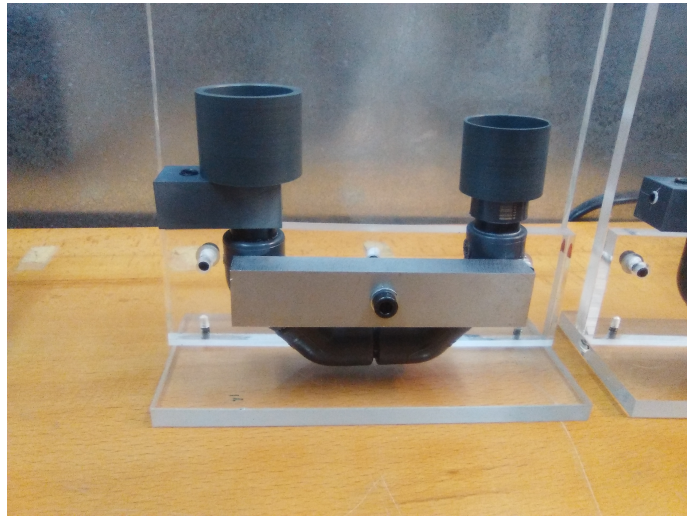


**Figura 5.2 – TRITIUM-IFIC 0 Prototype.**

which their gain are  $1.26 \cdot 10^6$  and  $1.01 \cdot 10^6$  and their quantum efficiency are 29.76% and 28.66% respectively. Their signals were precessed and analyzed using the electronic configuration shown in Figure 3.14b.

Two identical prototypes were built and filled following the same protocol but using different liquid solutions. The first prototype, called TRITIUM-IFIC 0 Background, was filled only with ultrapure water (39 mL, uncertainty of 0.05%) and it was used to measure the radioactive background of the detector whereas the other prototype, called TRITIUM-IFIC 0 Signal, was filled with a radioactive liquid source of tritium, the preparation of which is explained in the appendix C. The specific activity of the liquid source employed was 99.696 kBq/L (uncertainty of 2.24%) and the volume used to fill this prototype was the same as the other, 39 mL (uncertainty of 0.05%). Therefore, the total activity of this tritiated water sample is approximately  $3.888 \pm 0.087$  kBq.

This second prototype was used to measure the signal of the detector (tritium + background) and the measured tritium activity can be known by extracting the background (measurement of TRITIUM-IFIC 0

Background) to the signal (measurement of TRITIUM-IFIC 0 Signal).

A statistically significant amount of time coincident events was not found in both PMTs, so the measurement of time coincidence was not possible.

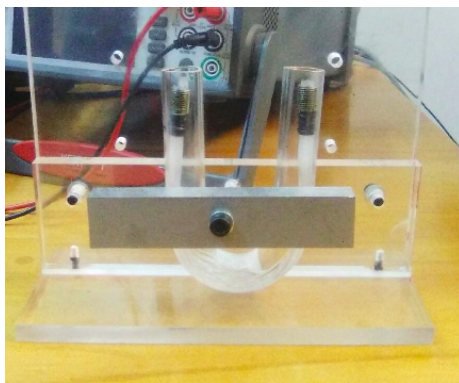
The loss of photons could be caused for several reasons, such as the poor quality of the tritiated water-fiber interface or the excessive curvature in the fiber bundle due to the U-shape of TRITIUM-IFIC 0 prototype, causing that too many photons escape from the fibers. The cleaning process explained in section 4.1.4 was motivated by this result.

To avoid this problem and obtain some results with this prototype, a measurement was performed with a single PMT. For this task, the electronic configuration shown in Figure 3.14a was used. The results of these measurements are shown in section 7.1.1, where they are discussed.

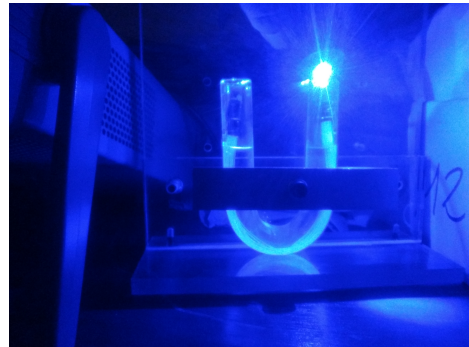
In addition, a test was carried out to explain why it was not possible to measure both PMTs in time coincidence. For this task a transparent PMMA vessel, shown in Figure 5.3a, was built in a similar shape to that of the TRITIUM-IFIC 0 prototype vessel to check the effect of the fiber bundle curve.

The LED shown in section 4.1.3 was used to verify the reduction in photocollection efficiency of the fiber bundle due to this curve.

As can be seen visually in Figure 5.3b, a large percentage of the photons are lost due to the curve, which can be easily solved by using a straight fiber arrangement in next prototypes.



(a) PMMA vessel.



(b) Test performed to check the lost photons.

**Figura 5.3** – PMMA vessel used to check photon loss due to fiber bundle curve.

### 5.1.2 TRITIUM-IFIC 1

The next prototype, TRITIUM-IFIC 1, was intended to overcome the problems and limitations found in the previous one, TRITIUM-IFIC 0, section 5.1.1. To do so, some improvements were applied on it:

1. The fiber bundle is arranged straight to optimize the photon collection efficiency of the fibers.
2. A special fiber cleaning protocol, explained in section 4.1.4, was applied on the fibers. It was used to improve the interfaces between fiber and tritiated water, creating a better wetting property of the fiber, which will result in more tritium events detected and a larger photon collection efficiency.
3. Teflon vessel was using in the Tritium prototypes to reduce the effect of the small photon collection efficiency of the fibers, measured in section 4.1.3, which is an innerent characteristic of the fiber which cannot be changed.

Teflon is an interesting material for its optical properties, specifically its reflection factor, which is very close to 100% at the working wavelength.

The TRITIUM-IFIC 1 prototype consists of 64 scintillating fibers, with a length of 20 cm, that are arranged in a straight position using a teflon structure, shown in Figure 5.4. The fibers are fixed in an  $8 \cdot 8$  square matrix.

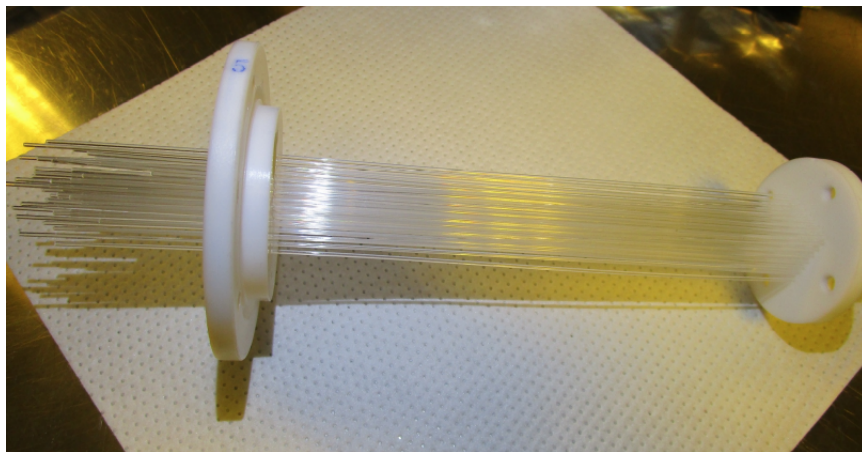


**Figura 5.4** – Teflon structure used to arrange the fibers of TRITIUM-IFIC 1 prototype in a matrix of  $8 \cdot 8$ .

A new teflon vessel was designed and built, shown in Figure 5.5. It has a cylindrical hole whose internal diameter and length are 48 mm and 200 mm respectively, where the fiber structure will be placed.

In addition to cutting and polishing the scintillating fibers, a cleaning process, described in section 4.1.4, was applied to them to achieve a better tritiated water-fiber interface.

A piece of PVC was used to fix the photosensor on the prototype and prevent the photosensor from being affected by external light. A general

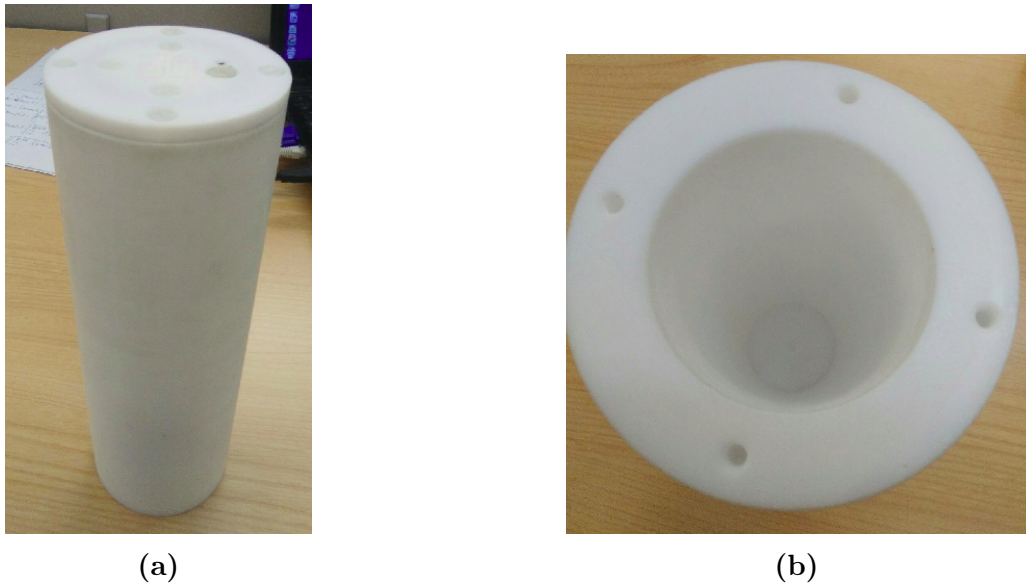


**Figura 5.5** – Teflon vessel of TRITIUM-IFIC 1 prototype

view of this prototype is shown in Figure 5.6, which, for radioactivity safety reasons, will be read using only one PMT.

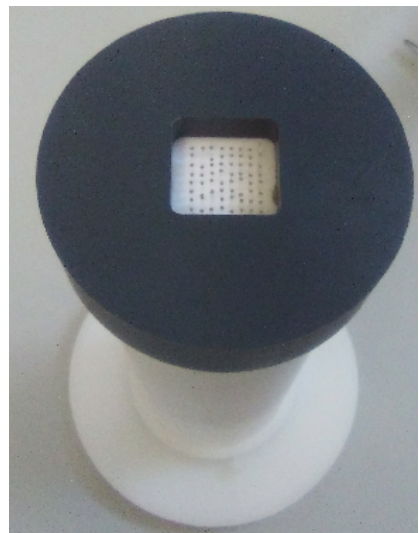
The PMT used was the model R8520-460, from Hamamatsu Photonics company [81] and it was coupled directly to the fiber bundle using optical grease [125]. The electronic circuit, shown in figure 3.9, was used to distributed the high voltage between the dynodes. The employed high voltage was  $-800$  V, at which, its quantum efficiency is 28.66%.

The signal from this PMT was processed and analyzed using the same electronic configuration as that used for the TRITIUM-IFIC 0 prototype, shown in Figure 3.14a.

Unlike the previous prototype, only one TRITIUM-IFIC 1 was built. First, it was filled with ultrapure water (118 mL, uncertainty of 0.05%) and several background measurements were taken over a week. Then, it was emptied and refilled using 118 mL (uncertainty of 0.05%)



(a)



(b)

**Figura 5.6** – A general view of TRITIUM-IFIC 1 prototype

of the radioactive liquid source of tritium explained in appendix C.

The results of these measurements are shown in section 7.1.2, where they are discussed and compared with the result obtained with the previous prototype, TRITIUM-IFIC 0.

## 5.2 Latest TRITIUM Prototypes

This section shows the last prototypes, TRITIUM-Aveiro 0 and TRITIUM-IFIC 2, in which the problems previously found are solved and a well-defined design is developed for them.

A different design was employed in both prototypes so that they can allow the reading of a large number of fibers arranged in a straight position with two photosensors in time coincidence, in a safe way.

Particular attention to tritium detection efficiency was paid in these prototypes, which is the reason why they use many more fibers than the preliminary prototypes and a time coincidence reading of these fibers is done using two photosensors.

Furthermore, the activity of the radioactive liquid source of tritium, which is used to fill these prototypes, is lower since the interesting parameter to be measured is their low detection level, LDL.

The design of both prototypes is very similar and their objective is to test the subtle effects caused by the little difference, such as the diameter of the fibers used, and to choose the one with the best results which will be included in the final design of the TRITIUM monitor.

### 5.2.1 TRITIUM-Aveiro 0

The third prototype built and the first thought to be the final version of the TRITIUM detector module was TRITIUM-Aveiro 0, shown in Figure 5.7, which was designed and built in the Aveiro workshop.

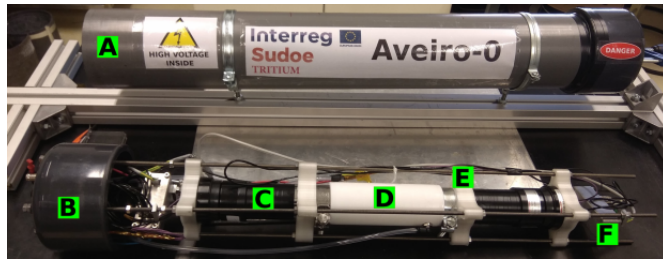


**Figura 5.7** – TRITIUM-Aveiro prototype.

It consists of a teflon vessel (D of Figure 5.7), shown in Figure 5.8, which has an internal cylindrical hole the diameter and length of which are 43 mm and 180 mm respectively.



**Figura 5.8** – Teflon structure and fiber bundle used in TRITIUM-Aveiro 0 prototype.

This vessel contains 360 no-clad scintillating fibers with a length of 180 mm. The model of the used fibers is BCF-10 from Saint-Gobain company [131], which have practically the same characteristics than the

others used up to now (BCF-12 fibers) and their most important difference is the diameter, which is the double, 2 mm.

A larger diameter could be interesting because it facilitates the flow of water around the fibers, reducing the problems related to surface tension and ensuring that the entire active volume of the fibers is used for tritium detection. In addition, it increase the resistance of the fibers, which is very important since the water is flow around them. However, it could be detrimental since this worsens the signal-to-background ratio. The detector active volume for 2 mm fibers in the same space is smaller, producing a smaller tritium signal and the part of the fibers where no tritium events reach (they only contribute to the background) is larger, producing a larger background.

In order to quantify the importance of the fiber diameter effect, the measurements were compared with similar measurements performed with TRITIUM-IFIC 2 prototype, shown in section 5.2.2, based on a similar configuration with 1 mm fibers (BCF-12 model).

The amount of fibers used in TRITIUM-Aveiro 0 prototype is the maximum which allows the water to flow around the fibers and a structure was not feasible to use to fix them due to the large amount of them used. These fibers were cut with the fiber cutting device developed by TRITIUM but they were neither polished nor cleaned. The reason for this is that the automatic polishing machine was not yet developed and it was not feasible to polish 360 fibers by hand. In fact, the automatic polishing machine was motivated by the amount of fibers used in the last TRITIUM prototypes.

To ensure the radiosecurity of this prototype, the teflon vessel is totally closed and a water inlet/outlet were installed in its Teflon vessel to allow a constant water flux through it. Two PMMA windows was used to read the fibers, whose thick is 10 mm, which was located at both ends of the fiber bundle. Two clamps are used to press the Teflon walls against the

PMMA windows to ensure the water tightness of the prototype. PMMA was chosen for its optical properties, especially its transmission coefficient, which was measured for visible light range in the ICMOL laboratories, shown in Figure 5.9.

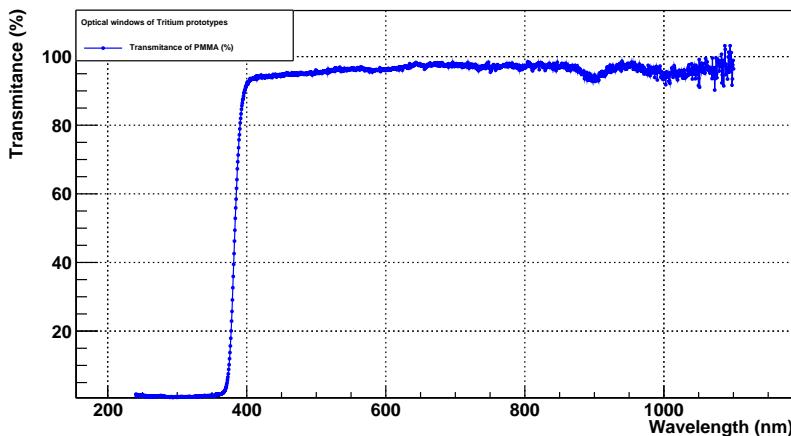


**Figura 5.9** – Transmission spectrum of light (in the visible range) in a piece of PMMA of X thickness measured in the ICMOL laboratory.

As can be seen, its transmission coefficient is approximately 95% for the working wavelength (435 nm). Slightly better transmission coefficients can be achieved with other materials such as quartz or sapphire but they are much more expensive.

Two PMTs (C of Figure 5.7) are used to read this prototype in time coincidence, which are powered at  $-1500$  V, at which the quantum efficiency is 26%. They are fixed to both fiber bundle ends of the prototype using two pieces (E of Figure 5.7) which was designed and built with a 3D printer. Both PMTs are optically coupled to the PMMA windows using optical grease [125].

The PMTs used are the model R2154-02 2" from Hamamatsu company [132], whose characteristics, specially its gain and efficiency, are quite

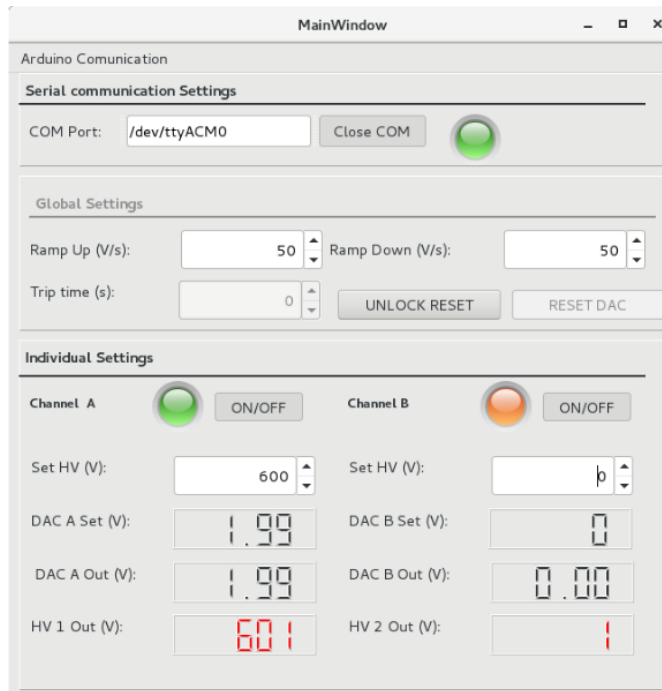
similar to the PMTs used in the other prototypes.

All these different parts, together with the electronic system (F of Figure 5.7), is arranged in a structure, shown in Figure 5.7, which is based on several nuts located on four long stainless-steel screws. These screws are fixed to an external PVC structure, A and B of Figure 5.7, which is used to protect the prototype from physical damage and provide a light-tight operation environment. This PVC structure is equipped with several high voltage power, low voltage power and signals feed-through connectors.

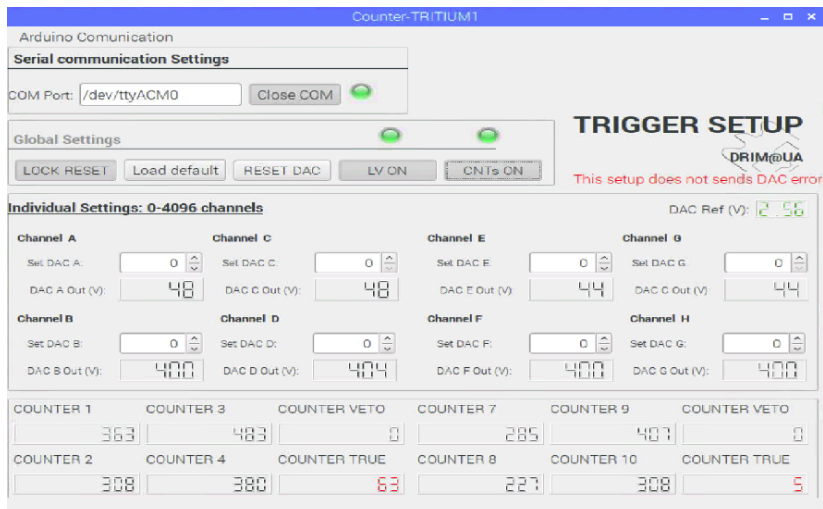
Only one prototype was built, which was designed to be installed in the Arrocampo dam and an electronic chain, based on several PCBs, was specially designed, developed, built and tested to process and analyze the signals of this system, shown in appendix D.

Two interfaces were developed, one to control the power supply to the PMTs, shown in Figure 5.10a, and the other to control the different options of the electronic reading chain, such as thresholds, shown in Figure 5.10b.

First some measurements were taken in the laboratory, which were used to characterize the detector. For this task it was firstly filled with ultrapure water, which was used to measure the background of the detector, and then, with a radioactive liquid tritium solution with an activity of 30 kBq/L, which were used to measure the efficiency and the low detection level, LDL, of the prototype. The volume of ultrapure water and tritium solution used in TRITIUM-Aveiro 0 prototype is 57.82 mL. Later, it was installed in the arrocampo dam to test its functionality and to begin with the tritium level monitoring. The laboratory and Arrocampo measurements, both, are shown in section 7.1.3, where they are discussed and compared with the measurements of the previous prototypes.



(a) Graphical user interface to manage the power supply voltage of PMTs.



(b) Graphical user interface used to manage the counter system.

**Figura 5.10** – Graphical User Interface developed to control the TRITIUM-Aveiro prototype.

### 5.2.2 Advanced IFIC prototype, Tritium-IFIC 2

The last prototype developed in TRITIUM experiment and the second thought to be the final versión of the TRITIUM detector module was TRITIUM-IFIC 2, which is shown in Figure 5.11, A.

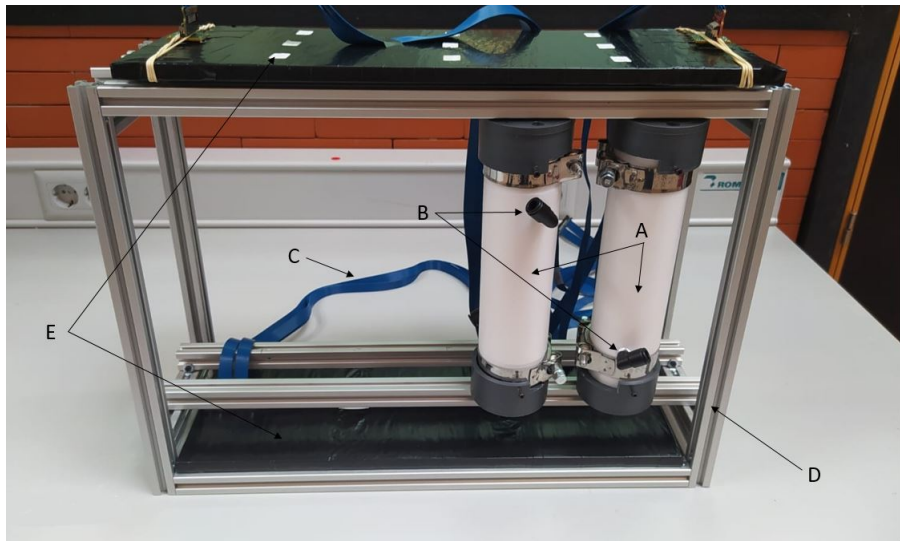


**Figura 5.11 – TRITIUM-IFIC 2 prototype.**

This prototype was designed and built in the IFIC workshop and it consists of a cylindrical teflon vessel, shown in Figure 5.12, the shape of which is similar to the one used in TRITIUM-Aveiro 0 prototype. The internal length and diameter of the teflon vessel are 200 mm and 36 mm respectively.

This prototype contains 800 no-clad scintillating fibers, model BCF-12, with a length of 200 mm, a larger number of fibers than the TRITIUM-Aveiro 0 prototype which are arranged in less volume.

The fibers used are cut, polished and cleaned with the conditioning processes previously shown in section 4.1 since, during the construction of the prototype, the development of the automatic polishing machine was



(a) TRITIUM-IFIC 2 vessel.



(b) TRITIUM-IFIC 2 vessel with PVC caps.

**Figura 5.12** – TRITIUM-IFIC 2 teflon vessel.

completed.

These fibers are freely arranged, with a density that allows water to flow through the fibers and two PMMA windows located at the ends of the fiber bundle were used to read this system, similar to the TRITIUM-Aveiro 0 prototype.

The width of the PMMA optical windows used is 5 mm, which is sufficient to guarantee radiosecurity since the detector works at very low water pressure and two clamps are used to ensure the watertightness of the prototype, similar to the TRITIUM-Aveiro 0 prototype. The transmission coefficient, shown in Figure 5.9, is practically unaffected by the little difference of the PMMA width used in both prototypes.

As can be seen in Figure 5.11, B, and Figure 5.12, a water inlet/outlet was installed in the teflon vessel to allow a constant water flux

through it, similar to the TRITIUM-Aveiro 0 prototype.

For the first laboratory measurements, two PMTs were used, model R8520-460 from the Hamamatsu Photonics company [81], which is useful to understand the results and compare them with the results obtained with the previous prototypes. However, measurements with SiPM arrays have already started the output signal of which is connected to PETSYS system through flat wires as can be seen in Figure 5.11, C.

As SiPM arrays readout by the PETSYS system will be employed in the TRITIUM-IFIC 2 prototype that will be installed in Arrocampo dam, it is not necessary to develop a electronics chain to process and analyze the PMT signals of this prototype.

Like the TRITIUM-Aveiro 0 prototype, although PETSYS has a graphical user interface, shown in Figure 5.13, which allows controlling all the different options such as the voltage with which the SiPM arrays is fed, the thresholds used, etc., normally it will be controlled remotely via computer terminal.

Two PVC caps, located at both ends of the prototype, Figure 5.12b, were used to work with the SiPMs in a light-tight environment and an aluminum structure, shown in Figure 5.11, was designed and built to house up to 10 TRITIUM-IFIC 2 modules and two cosmic vetos, shown in Figure 5.11, E.

The available space of the lead shielding, explained in section 3.4.1 is enough to accommodate up to 5 structures like the one shown in Figure 5.11. It means that the final TRITIUM module has the capacity to contains 50 TRITIUM-IFIC 2 modules and 10 different cosmic vetos. As the sensibility of the TRITIUM monitor scales with the number of TRITIUM modules used, the results obtained with the TRITIUM monitor can improve the results obtained with the TRITIUM-IFIC 2 prototype by a factor of N, where N is the number of cells used.

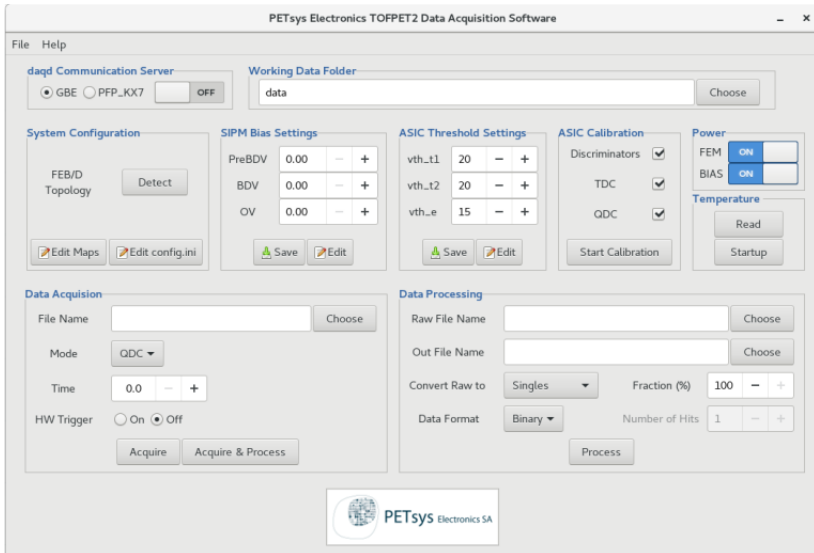


**Figura 5.13** – Graphical User Interface (GUI) of PETSYS.

Two identical TRITIUM-IFIC 2 prototypes were built, similar to the TRITIUM-IFIC 0 prototype, one of them was filled with ultrapure water and used to measure the background and the other was filled with a radioactive liquid source of tritium and used to measure the signal. The volume used in both cases was 82 mL (uncertainty of 0.05%).

The activity of the tritium source used for this prototype is 10 kBq/L (uncertainty of 2.24%), which was prepared by diluting a sample of tritiated water explained in appendix C with ultrapure water until the desired activity was achieved.

The results of this prototype is shown in section 7.1.4, where they are compared with the results of the previous prototypes and, specially, with TRITIUM-Aveiro 0 prototype.

## 5.3 Modular TRITIUM Detector for In-Situ Tritium Monitoring

Lastly, this section presents the final TRITIUM monitor, a schematic design of which is shown in Figure 5.14.

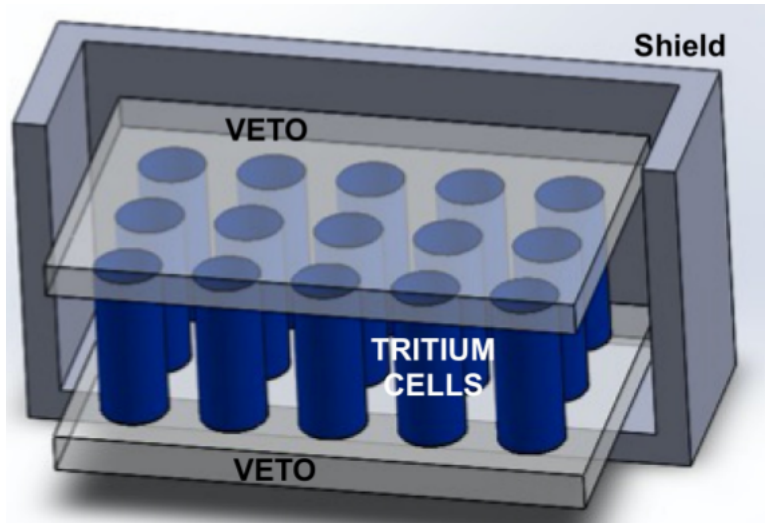


**Figura 5.14** – A schematic design of the TRITIUM detector.

It consists of several TRITIUM modules, shown in Figure 5.14, which are read in parallel. Each module will be the prototypes that achieves better results, TRITIUM-Aveiro 0 (section 5.2.1) or TRITIUM-IFIC 2 (section 5.2.2).

These modules are isolated from environmental radioactivity using three different techniques.

1. First, an external lead shielding, explained in section 3.4.1, a part of which is shown in Figure 5.14. This is used to stop the environmental radioactivity which increase the radioactive background measurement of the TRITIUM monitor

2. Second, several active vetos, explained in section 3.4.2 and characterized in section 4.4, which is shown in Figure 5.14, placed below and above the TRITIUM modules. These active vetos are read in anti-coincidence to eliminate the effect of the high energy events of the background, mainly cosmic events, on the TRITIUM measurement.
3. Finally, the radioactive elements present in the water samples, introduced into TRITIUM modules to be measured, are eliminated using an ultrapure water system, shown in section 3.3 and appendix B and characterized in section 4.3.

The ultrapure water system, lead shielding and a TRITIUM-Aveiro 0 prototype are installed and currently in operation at the Arrocampo dam. This entire system was used to successfully monitor the tritium levels in Arrocampo dam during three months. Furthermore, two TRITIUM-Aveiro 0 prototypes and four active vetos are currently under manufacturing to be installed, which are measured in parallel with the current prototype installed.

The RaspberryPi, in which the counter electronic system of TRITIUM-Aveiro prototype is based, has some counting limitations if multiple modules are used. To overcome this problem, it must be replaced with an FPGA-based counter board to ensure reliable counting.

At the same time, three TRITIUM-IFIC 2 prototypes and an active veto have already been built, the installation of which at the Arrocampo dam was delayed due to the coronavirus pandemic restrictions imposed in Spain. They will be installed as soon as possible.

One of the most important points of the TRITIUM detector is its modular design, with which an scalability can be achieved to reach the required sensitivity, 100 Bq/L. If this sensitivity goal is not reached with the three modules that will be installed, only some additional modules need to be installed to improve it.

The only scalability restriction is the available space, which is fixed by the lead shield already built and installed (it is also fixed by the available space in the house where the lead shield is installed). Taking into account the currently available space, five different structures designed for TRITIUM-IFIC 2, one of which is shown in Figure 5.15, can be used, where ten different modules (grey) and an active veto (black) can be accommodated in any of them.

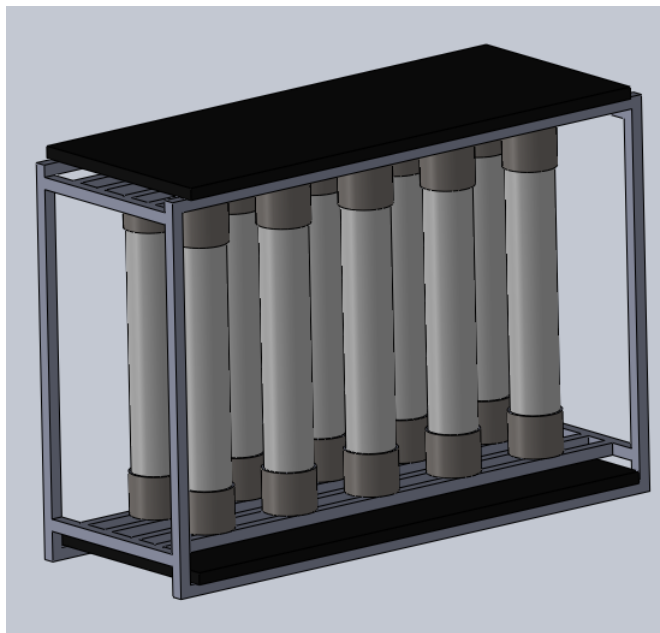


**Figura 5.15** – A TRITIUM detector design based on the TRITIUM-IFIC 2 prototype.

It means that up to 50 TRITIUM-IFIC 2 modules can be used in parallel, reducing the TRITIUM detector sensitivity by a factor of fifty. In light of the results obtained with these prototypes, it is not expected to use more than one structure like the one shown in Figure 5.15 (ten modules) to reach the target sensitivity.

# Chapter 6

## Simulations

This chapter details the Monte Carlo simulations that were performed in the TRITIUM experiment. Their goal were to choose the best design for the TRITIUM detector, understand its behavior and find its limitaitons. The simulation environment used for this task is Geant4 [75, 141].

### 6.1 Geant4 Environment

Geant4 is a software toolkit for the simulation of the passage of particles through matter. It is a package developed at CERN that is based on object-oriented technology implemented in the C ++ programming language.

It includes the definition of all the different aspects of the simulation process such as detector geometry, materials used, particles of interest, physics processes that handle particle and matter interactions, response of sensitive detectors, generation, storage and analysis of event data and visualization.

Geant4 simulates particle-by-particle physics. It means that the tritium events are initialized one by one, whose energy, moment, position, etc. are determined. Then, the propagation and interaction of each tritium event with the scintillator is simulated, in which optical photons are created. The propagation of these optical photons are also simulated one by one and the simulation ends when all tritium events have been simulated and the created optical photons have been absorbed by either the sensitive detector or other materials present in the simulation.

A physics list used for these simulations is Livermore, G4EmLivermorePhysics, which is specially designed to work with low energy particles. This list includes the most important electromagnetic process at low energies such as Bremsstrahlung, Coulomb scattering, atomic de-excitation (fluorescence) and other related effects.

The materials used in these simulations were water (to simulate the tritiated water source), PMMA (to simulate the optical windows of the prototype), polystyrene (to simulate the core of scintillating fibers), teflon (to simulate the prototype vessel), silicone (to simulate the optical grease), silicate glass (to simulate the optical windows of the PMTs) and bialkali (to simulate the photocathode material of the PMT).

The properties of water, teflon, polystyrene were taken from the Geant4 NIST database and the other materials were built by specifying their atoms. Optical properties was added to these materials:

1. First, the spectrum of the refractive index and the light attenuation were added to the water which was obtained from the reference [144]. Furthermore, an electron emission, uniformly distributed in the volume, was added to the water, the energy of which was calculated using the tritium energy spectrum. This emission of electrons simulates the disintegration of the dissolved tritium particles in the water sample. The used data was obtained from the reference [145].

2. Second, the spectrums of the refractive index, the light attenuation and the photon emission were added to the polystyrene, which was obtained from the data sheet of scintillating fibers, [78]. Also the scintillation yield and the decay time was included.
3. Third, the quantum efficiency spectrum was included to the photocathode material of the PMTs, the data of which was obtained from their data sheet, [81] and a refraction index of 1.46 was used for the optical grease, also obtained from its data sheet, [125].
4. Finally, the optical data for the remaining materials, PMMA windows, teflon and silicate glass, were taken from the reference [146].

It is important to note that this chapter is focused on the Tritium-IFIC 2 prototype since these were the simulations I was primarily working on, but a similar simulation was performed for the Tritium-Aveiro prototype, some of their most important results are shown in chapter 8. In addition, other smaller simulations are shown used to choose the best design of the TRITIUM detector.

## 6.2 Description of the Simulations Performed

Several simulations was designed and run during the life of the TRITIUM project to quantify how different values of interesting parameters affect to the tritium measurement and to understand the behaviour of the different TRITIUM prototype built which are shown in the following sections.

### 6.2.1 Tritiated Water Source

First of all the shape of the simulated tritiated water source was optimized.

The mean free path of tritium electrons in water are only around  $5 \mu\text{m}$ , so there are many electrons that don't reach the scintillating fibers, electrons that don't provide useful information and only contribute to being time consuming and reducing available computing resources.

To optimize the simulation, the dimensions of the simulated tritium source was studied. The goal of this study was to minimizes the tritium events that do not reach the scintillating fibers avoiding losing the tritium events that reach them.

This simulation test consists of a scintillating fiber with a length of 20 cm and a diameter of 2 mm and a surrounding tritiated water source with the same length and a thickness of 0.5 mm (100 times greater than the mean free path of tritium electrons) to ensure that this study take into account all possible tritium electrons that can reach to the scintillating fiber.

The dimensions of the fiber are not important in this study since only the energy deposition of tritium electrons in the fiber were simulated. That is, this simulation doesn't include the following steps such as photon generation, propagation of these photons, etc. in which the shape of the scintillating fiber becomes important.

The results of this simulation are shown in section 8.1.1, where they are discussed.

### 6.2.2 Energy deposition and light output of scintillating fibers

The scintillation yield provided by the manufacturer, 8000 phot./MeV only works for Minimum Ionizing Particles (MIP). As tritium electron energies are far from being MIP particles, the output light generated by the scintillating fibers was studied. For this task, the energy deposition of tritium

electrons on scintillating fibers was added to the simulation.

The proportionality between the output light per unit of path length,  $\frac{dL}{dx}$ , and the energy deposited per unit of path length  $\frac{dE}{dx}$  is affected by the light quenching through the so-called Birks coefficient, following equation [147]

$$\frac{dL}{dx} = S \frac{\frac{dE}{dx}}{1 + k_B \frac{dE}{dx}} \quad (6.1)$$

where  $S$  is the scintillation yield, provided by the manufacturer. A value of  $k_B = 0.126$  mm/MeV was considered for the Birk's coefficient which is the one used for scintillators based on polystyrene [148]. The effect of this correction is shown and discussed in section 8.1.2.

### 6.2.3 Fiber Length Optimization

Another test was performed to find the fiber length that optimizes the tritium detection efficiency. Two different lengths of the scintillating fiber were considered in this study, 1 m and 25 cm.

As the active area of the detector is related with its tritium detection efficiency, the advantage to use a longer fibers is that the same active area can be achieved with a less number of cells, considerably reducing the number of used photosensors and, as a consequence, the price of the TRITIUM monitor. However, smaller length of scintillating fibers reduce de photon absorption produced in the fibers, increasing the tritium detection efficiency for the same active area.

For this task, the Tritium-Aveiro prototype was simulated, consisting of a similar design of TRITIUM-IFIC 2 prototype but using 360 scintillating fibers of 2 mm diameter and readout by two different photosensors, model R2154-02 2" from Hamamatsu company [132]. All optical

properties mentioned in section 6.1 were included in this study.

The results of this study are shown in section 8.1.3, where they are discussed.

### 6.2.4 Fiber Diameter Effect

A third test was carried out to check the effect of the fiber diameter in the tritium measurement. For this test, the same simulation explained in section 6.2.3 was used, where a fiber length of 20 cm was chosen. Two different diameters were taken into account in this study, 1 mm and 2 mm, which are the commercial options given by Saint-Gobain company.

It doesn't have sense to test it with the tritium source since its efficiency will scale with the active surface of the scintillating fiber. However, an interesting study can be performed to check how the fiber diameter affect to the cosmic detection in the fiber. It is an important result as the background-signal ratio is mainly affected by the cosmic ray events.

For this task, the tritiated water source was replaced by a cosmic ray source, which was generated using the CRY library<sup>1</sup> [142], [143]. The CRY library is a package based on object-oriented technology and implemented in the C++ programming language. This library is used to generate cosmic-ray shower distributions for different particles (muons, neutrons, protons, electrons, photons and pions) with several options that can be varied like several altitude.

The cosmic sources shape used in this simulation is a horizontal square of  $1 \cdot 1 \text{ m}^2$  located at a height of 35 cm (above the detector) with the typical distribution of cosmic particles at sea level.

---

<sup>1</sup>CRY library, Cosmic-Ray Shower library

The result of this simulation are shown in section 8.1.4, where they are discussed.

### 6.2.5 Simulation of the Tritium-IFIC 2 Prototype

The Tritium-IFIC 2 prototype simulation was the last prototype simulation developed in the TRITIUM experiment and this was the one I mainly focused on. It consists of 800 equispaced fibers distributed in sixteen different circles with increasing radius, which are shown in Figure 6.1. The fibers simulated has a diameter of 1 mm and the optical properties, mentioned in section 6.1, was included.

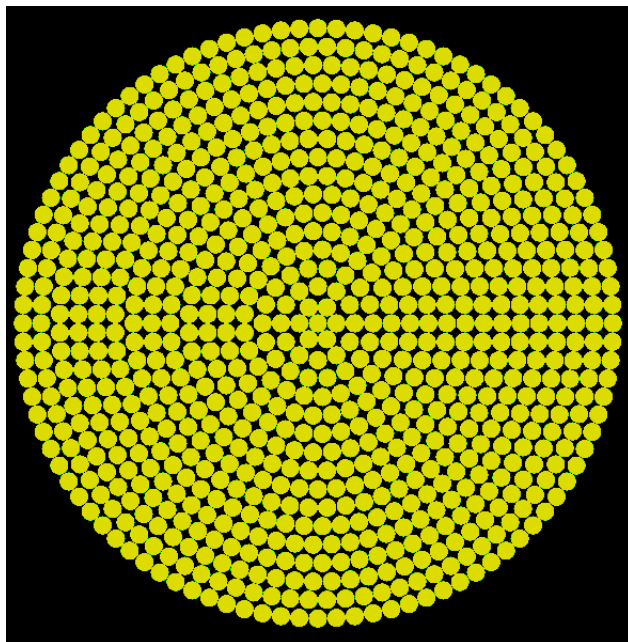


**Figura 6.1** – Distribution of the scintillating fibers in the simualtion of Tritium-IFIC 2 prototype.

The tritiated water source used consists of a tritiated water volume with a thickness of 5  $\mu\text{m}$  around each scintillating fiber.

Scintillator fibers are located inside of a teflon vessel, which was simulated with the dimensions mentioned in section 5.2.2. Two PMMA windows with a thickness of 5 mm were simulated and located in both fiber ends and a optical grease layer with a thickness of 0.5 mm was included in each PMMA windows.

Finally, two PMTs, model R8520-460 from Hamamatsu company [81], were simulated in both ends.

The optical properties used for the tritiated water, teflon vessel, PMMA windows and the optical grease are exactly the same as those used for the Tritium-Aveiro 0 prototype simulation.

The simulation of TRITIUM-IFIC 2 is shown in Figure 6.2 in which can be appreciated the PMTs (black), the optical grease (blue), PMMA windows (white), tritiated water (green) and scintillating fibers (yellow). In this image, the Teflon container was not drawn to allow its interior to be seen and several volumes of tritiated water were also not included to allow several scintillation fibers to be seen.

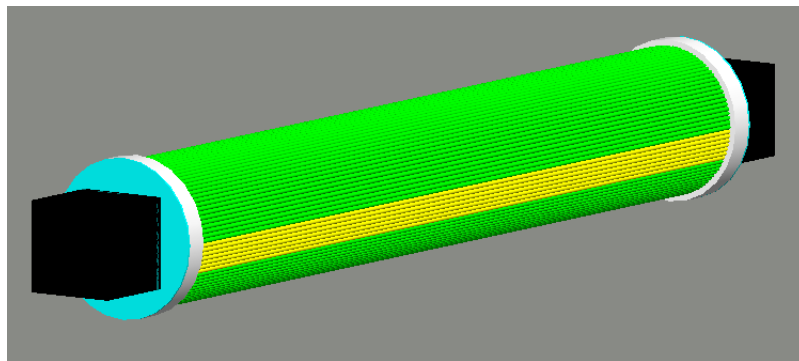


**Figura 6.2** – Simualtion of Tritium-IFIC 2 prototype. PMTs (black), the optical grease (blue), PMMA windows (white), tritiated water (green) and scintillating fibers (yellow)

As can be seen in this figure, the used PMTs don't cover the entire active area formed by the scintillating fiber bundle. It's not a problem for

the Tritium detector since its final version will not include this photosensors. The final version of Tritium-IFIC 2 prototype will use SiPM arrays and the PMTs model used in the Tritium-Aveiro 0 prototype are circular PMTs with which the full active area is covered.

The simulation of the Tritium-Aveiro 0 prototype is similar to this since the design of both detectors are quite similar. There are two main difference between both simulated prototypes:

1. The diameter of the fibers used, which is 1 mm for Tritium-IFIC 2 prototype and 2 mm for Tritium-Aveiro 0 prototype. As the internal volume of the teflon vessel is filled, this difference imply a difference number of the scintillating fibers used, causing a difference in the signal-background ratio.
2. The photosensors used since, although both are PMTs, the model of the used PMTs is different and it cause a different active area readout, affecting to the tritium detection efficiency.

The results obtained with the simulation of the TRITIUM-IFIC 2 prototype are shown in section 8.2.1, where they are discussed.

### 6.2.6 Simulation of the Lead Shielding and Cosmic Veto

Finally the lead shielding and active vetos, detailed in section 6.2.5, were included in the simulation of the Tritium-IFIC 2 prototype. The objective of these simulations was to demonstrate its need, quantifying its effect in reducing the cosmic events detected by the prototype.

For this task, similar to that done in section 6.2.4, the tritium source was replaced by the cosmic events source, which was simulated through the CRY library.

As can be seen in Figures 3.23a and 3.23b, two plastic scintillators were simulated with the dimensions mentioned in section 3.4.2 and located above and below of the Tritium-IFIC 2 prototype simulated.

The optical properties included to this plastic scintillators are the refractive index, the light attenuation spectrum and energy emission spectrum, the values of which were obtained from their data sheet provided by the manufacturer [112].

As shown in this figure, two PMTs, model R8520-460 from Hamamatsu company, were simulated to read each plastic scintillator, similar to that presented in section 3.4.2.

Finally, a lead shielding was simulated, whose properties were taken from the Geant4 NIST database. The dimensions of the simulated lead shielding were  $60 \cdot 60 \cdot 70$  cm<sup>3</sup>, which is the minimum needed to accommodate the active vetos and Tritium detector module inside. The length of the simulated lead castle, 60 cm, is smaller than real dimension, 148 cm. The reason for this is that only one tritium detector module was simulated, so the dimension of the lead shielding can be reduced to optimize simulation time and computing resources.

The results of these simulation are shown in section 8.2.2, where they are discussed.

# Chapter 7

## TRITIUM Monitor Results and Discussion

This chapter shows and discusses the experimental results obtained with the different prototypes developed in the TRITIUM experiment. This is divided into two sections, according to the place where they were carried out. The first section shows the measurements obtained at the University Laboratories, where external atmospheric conditions affecting the measurement, such as temperature, can be controlled. The second section shows the measurements obtained at the Arrocampo dam, the final TRITIUM monitor emplacement, where the control of external atmospheric conditions is less precise.

Additionally, an estimation of the results to be obtained with the TRITIUM monitor based on various TRITIUM-IFIC 2 prototypes are also presented in the last section.

## 7.1 Results from Laboratory measurements

This section shows, compares and discusses the experimental results obtained with the different prototypes developed in the TRITIUM experiment during their installation in the laboratory. The facilities used for this task were the Nuclear Radiation Laboratory, at the IFIC, Valencia, the DRIM<sup>1</sup>, at the University of Aveiro, and the LARUEX<sup>2</sup> laboratory in Extremadura.

### 7.1.1 Experimental Results of TRITIUM-IFIC 0 Prototype

This section shows the measurements obtained with the TRITIUM-IFIC 0 prototype during its installation in the Nuclear Radiation Laboratory at IFIC, the design of which was explained in section 5.1.1.

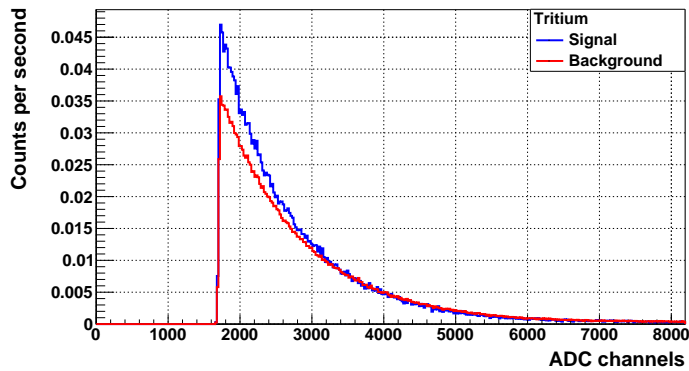
As stated in section 5.1.1, a statistically significant number of events was not obtained when the prototype was read with two PMTs in time coincidence. To overcome this problem, a single PMT measurement was taken using the electronic chain configuration shown in figure 3.14a. The energy spectra were measured for both, the signal and background prototypes, which are shown in Figure 7.1a. As it was mentioned in section 5.1.1, the signal prototype was filled with a tritiated water solution with an activity of 99.696 kBq/L and the background prototype was filled with ultrapure water.

In this figure, a difference between both energy spectra is clearly visible, which correspond to the energy spectrum of tritium, Figure 7.1b. A number of counts per second of  $2.27 \pm 0.06$  and  $2.06 \pm 0.06$  was obtained

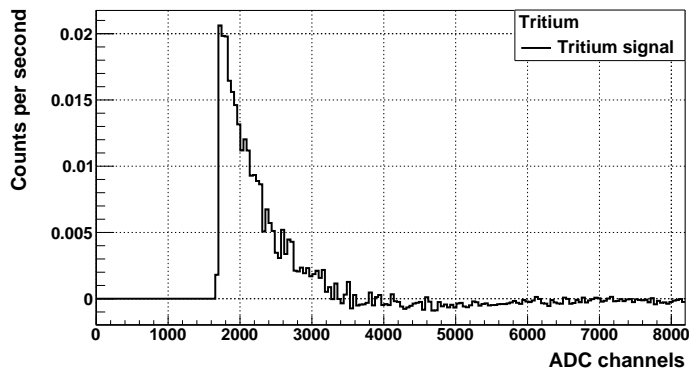
---

<sup>1</sup>Deteção da Radiação e Laboratorio Imagem Médica laboratoire (Laboratory for Radiation Detection and Medical Imaging)

<sup>2</sup>Laboratorio de Radiactividad Ambiental de la Universidad de Extremadura



(a) Signal and background energy spectra.



(b) Tritium energy spectrum.

**Figura 7.1** – Energy spectra experimentally measured with TRITIUM-IFIC 0 prototype.

for the both measurements, signal and background, respectively. Therefore,  $0.21 \pm 0.085$  counts per second was obtained for the tritiated water source used.

The tritium detection efficiency obtained for this prototype is  $(2.11 \pm 0.85) \cdot 10^{-3} \frac{\text{c/s}}{\text{kBq/L}}$ , which is calculated from the quotient of both, the counts per second measured and the specific activity of the tritium liquid source used.

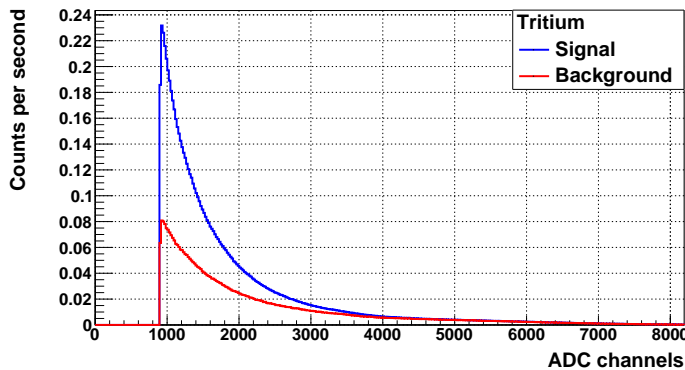
Comparing with the detectors developed so far by other experiments, Table 2.2 the efficiency obtained is of the order of the detectors the worst results, obtained by Moghissi and Muramatsu.

As we explained in section 2.1, the efficiency of scintillating detectors scales with the active area of the scintillator used. Therefore, to compare the efficiency with other detectors and with other prototypes developed in TRITIUM experiment, the specific efficiency of this prototype is calculated, the value of which is  $(9.59 \pm 3.88) \cdot 10^{-6} \frac{\text{c/s}}{\text{kBq/L cm}^2}$ .

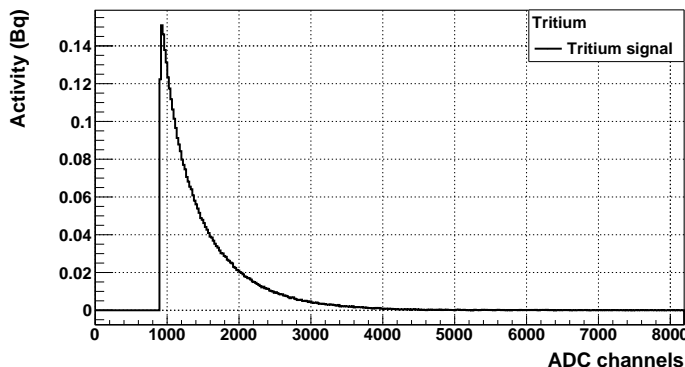
As can be seen in the Table 2.2 the specific efficiency is a little bit larger than the detectors with the worsen specific efficiency developed up to now, Muramatsu and Moghissi. This fact can be explained with the loss of photons produced in the curve of the fiber bunch, discussed and experimentally demonstrated in section 5.1.1.

### 7.1.2 Experimental Results of TRITIUM-IFIC 1 Prototype

This section shows the results obtained with the TRITIUM-IFIC 1 prototype during its installation in the Nuclear Radiation Laboratory at IFIC. Its design is explained in section 5.1.2, which includes several improvements, such as a teflon vesel and new straight arrangement of scintillating fibers,



(a) Signal and background energy spectra.



(b) Tritium energy spectrum.

**Figura 7.2** – Energy spectra experimentally measured with TRITIUM-IFIC 1 prototype.

which were found to be a problems in the previous prototype, reducing its efficiency.

The energy spectra of both, signal and background, were measured with TRITIUM-IFIC 1 prototype, which is shown in Figure 7.2a. As it was mentioned in section 5.1.2, to measure the signal, the prototype was filled with a tritiated water solution with an activity of 99.696 kBq/L and, to measure the background, the prototype was filled with ultrapure water.

As can be see, the difference between both energy spectra is clearly visible, which corresponds to the tritium energy spectrum, Figura 7.2b. Furthermore, compared to the energy spectra obtained with the previous prototype, Figure 7.1a, the difference between both is larger, which implies that the tritium detection efficiency of this prototype was improved.

This efficiency improvement can be quantified using similar calculations than those used in the previous section. The number of counts per second measured for signal and background, both, are  $7.82 \pm 0.11$  and  $3.99 \pm 0.08$  respectively. Therefore,  $3.83 \pm 0.13$  counts per second were obtained for the tritiated water source used.

The tritium detection efficiency of TRITIUM-IFIC 1 is  $(3.84 \pm 0.16) \cdot 10^{-2} \frac{\text{c/s}}{\text{kBq/L}}$ , which is calculated using the same quotient explained in the previous section. As can be seen, the efficiency obtained for this prototype is larger than that obtained for the previous prototype, TRITIUM-IFIC 0. It is an expected result since this prototype uses a larger active area. The specific efficiency is calculated to eliminate the effect of different active areas between both prototypes and quantify the improvement in the efficiency due to modifications in the design. The specific efficiency obtained is  $(9.56 \pm 0.40) \cdot 10^{-5} \frac{\text{c/s}}{\text{kBq/L cm}^2}$ .

Therefore it was verified that the specific efficiency of this prototype was improved by a factor of ten due to the modifications applied to its design which confirms and quantifies the usefulness of these modifications. Furthermore, compared with scintillating detectors developed in other experiments, table 2.2, on the one hand, the efficiency of this prototype is very close to the best result, obtained for Singh, and, on the other hand, the specific efficiency, which is a most relevant value to compare, is almost 5 times larger than the best results, obtained for Hofstetter.

It must be taken into account that in the first two prototypes the Low Detection Level, LDL, was not studied, since their objective was to

improve its design and find the problems that reduced their efficiency. In fact, it can be seen in Figure 7.2 that the activity used is further to be the LDL of the TRITIUM-IFIC 1 prototype. The LDL was only studied in the final prototypes.

### 7.1.3 Experimental Results of TRITIUM-Aveiro 0 prototype

This section shows the results obtained with the TRITIUM-Aveiro 0 prototype during its installation in Aveiro and Extremadura laboratories. The design of this prototype is shown in section 5.2.1.

This prototype was first installed in the DRIM laboratory, at the University of Aveiro, where the first measurements were taken. These measurements were used to find and solve the problems, learn about low energy detection and develop a functional scintillation prototype for TRITIUM.

First, the energy distribution of a single photon was measured from the self-emission of PMTs (dark current). To avoid the environmental light detection, the TRITIUM-Aveiro prototype was removed and the measurement was carried out only with the PMTs used, the windows of which were covered with black caps. The output signals of the PMTs were digitalized, shaped and pulse-height measured by a CAEN V1724 digitalizer [149].

The single-photon energy distribution of both PMTs is shown in Figure 7.3 in which a gaussian function was fitted. Due to the electrical noise of the PMT, an extrapolation (dashed line) was needed to be applied.

As can be seen, the distribution obtained with PMT1 deviates from the Gaussian function due to the higher noise in the low energy channels. It could be interesting to use PMT with very low background for future prototypes.

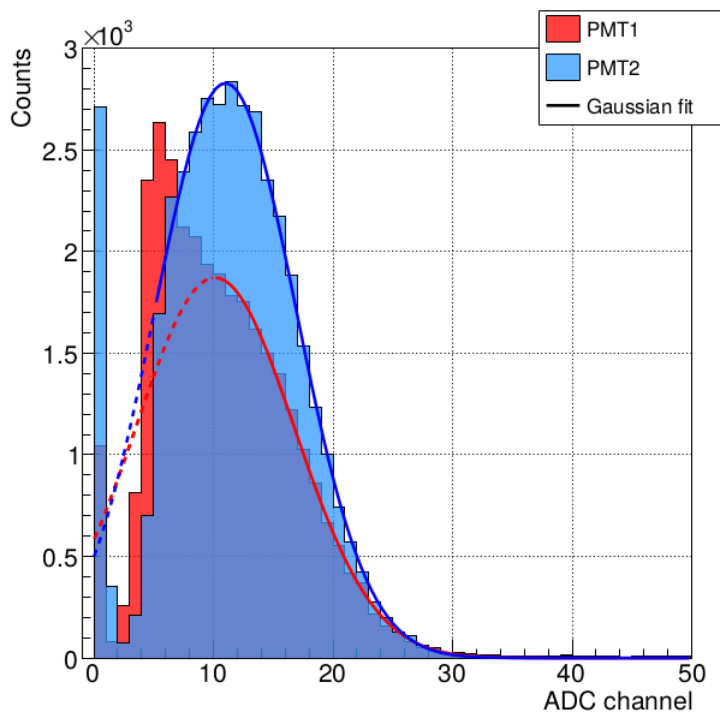


**Figura 7.3** – The single-photon energy distribution of both PMTs used in the TRITIUM-Aveiro 0 prototype and their sum [151].

As DRIM laboratory was not equipped to work with liquid radioactive source such as tritiated water, the first measurements were taken with a  $^{55}\text{Fe}$  radioactive source since its  $\gamma$  emission, 5.9 keV, is very close to the energy of tritium electrons. To do so, the TRITIUM-Aveiro 0 prototype was coupled to both PMTs using optical grease and, due to its low mean free path in solid materials, the radioactive source was placed inside the teflon vessel. This prototype was not filled with water because of the presence of the radioactive source. This measurement is shown in Figure 7.4.

A shift to the right side is observed for the PMT2 data, which is produced because this PMT has a higher gain and the radioactive source was placed closer to it, reducing the attenuation of the photons.

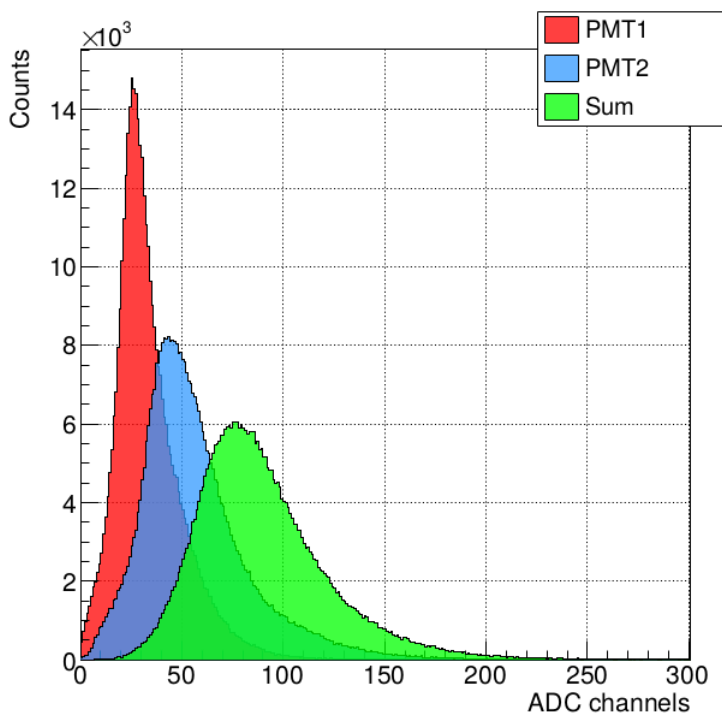


**Figura 7.4** – Measurement of a  $^{55}\text{Fe}$  radioactive source with the TRITIUM-Aveiro 0 prototype [151].

Lastly, a passive shield test was performed in the DRIM laboratory to quantify the attenuation of the background produced by lead. To do so, the  $^{55}\text{Fe}$  radioactive source was removed and the electronical chain explained in appendix D was used in counting mode for this test.

The measurements, shown in Figure 7.5, were carried out in three different situations. The first, region A, in which the measurement was performed without using any lead foil, the second, region B, in which lead foil with a thickness of 2.5 mm was used and the third, region C, in which another lead foil layer with the same thickness (total thickness of 5 mm) was used.

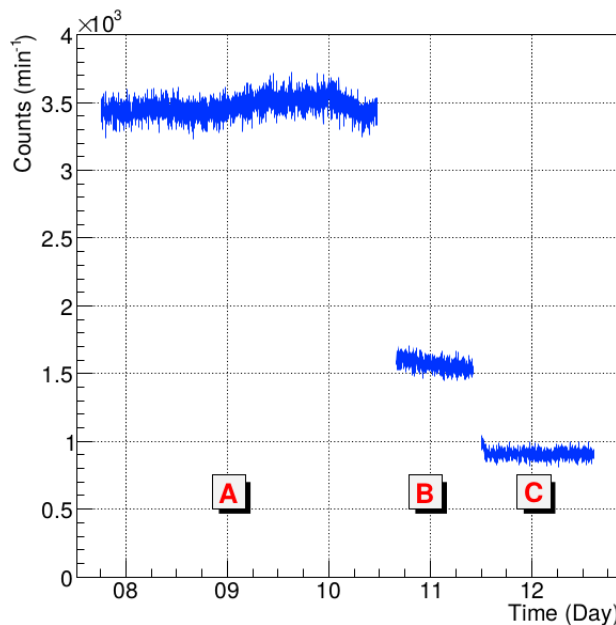


**Figura 7.5** – Measurement of the background with TRITIUM-Aveiro 0 prototype covered with different thicknesses of lead [151].

As can be seen, in the region A, the average of the data acquired during 2.5 days is  $3.5 \cdot 10^3$  counts/min (58 counts/sec). In the region B a reduction of more than two times was observed due to the covering with 2.5 mm of lead, measuring an average of  $1.6 \cdot 10^3$  counts/min (26

counts/sec). In the region C a reduction of about 4 times relatively to the region A is observed due to the covering with 5 mm of lead, measuring an average of  $0.9 \cdot 10^3$  counts/min (15 counts/sec).

It has to be taken into account that the case C is the real situation that is present in Arrocampo since, as it has been shown in section 3.4.2, the thickness of the lead shielding is 5 mm.

As it was said, the DRIM laboratory was not equipped to work with a liquid radioactive source such as tritiated water, so this prototype was installed in the LARUEX laboratory, at the University of Extremadura to finalize with the characterization measurements.

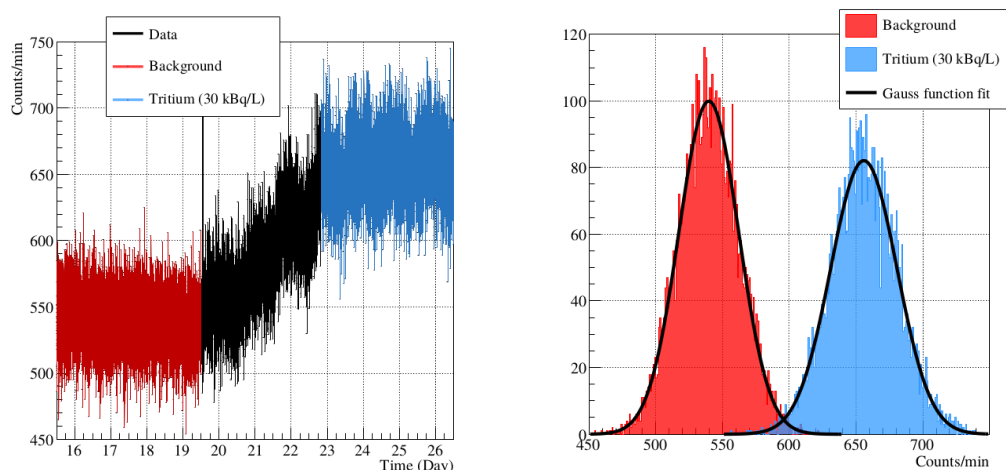
First, the background of the prototype was measured during 4 days. For this task, the prototype was filled with ultrapure water and covered with lead bricks with a thickness of XXX. The time of each measurement is 1 minut and the data is shown in Figure 7.6a and 7.6b in which a gaussian fit was done.

As a result of the gaussian fit, an average ( $N_B$ ) of 540 counts/min and standard deviation ( $\sigma_{Nb}$ ) of 22.61 counts/min was obtained. To calculate the Minimum Detectable Activity (MDA), the detection limit concepts developed by Lloyd A. Currie [150] was applied. With this concepts, the minimum net counts with the probability of a false-negative less than a 5%,  $N_D$ , and minimum net currents with the probability of a false-positive less than a 5%,  $L_C$ , called critical level, are calculated using the equations:

$$L_C = 2\kappa\sigma_{Nb} = 53 \text{ counts/min} \quad (7.1)$$

$$L_D = \kappa^2 + 2L_C = 108 \text{ counts/min} \quad (7.2)$$

Both values refer to the net counts per minute after background subtraction, so,  $L'_C$  and  $N'_D$  referred to the detector signal (before background



(a) Counts per minut measured as a function of time.

(b) Distribution of the acquired data.

**Figura 7.6** – Measurements of the background and tritium liquid source (with an activity of 29.8 kBq/L) performed with the TRITIUM-Aveiro 0 prototype and integrated during a minute [151].

subtraction) are 593 and 648 counts/min respectively.

To find the MDA associated to this  $N'_D$ , tritiated water was slowly added so that the tritium water activity increased continuously up to an average of  $656 \pm 0.43$  counts/min. Then, the tritiated water was measured with a Quantulus system, obtaining a MDA of 29.8 kBq/L.

The tritium detection efficiency can be calculated from the quotient of the net tritium counts per second measured,  $1.93 \pm 0.58$  counts/sec, and the activity of the tritium source used. The efficiency obtained is  $(6.49 \pm 1.94) \cdot 10^{-2} \frac{\text{c/s}}{\text{kBq/L}}$ . The value obtained with TRITIUM-Aveiro 0 prototype is larger than the efficiency reported by other similar experiments, Table 2.2. This is also larger than the efficiency obtained with previous TRITIUM prototypes, an expected result since the active area of this prototype is on order of magnitud larger.

The specific efficiency is calculated to compare with other scintillating detectors, the value of which is  $(1.59 \pm 0.48) \cdot 10^{-5} \frac{\text{c/s}}{\text{kBq/L cm}^2}$ . Comparing with the specific efficiency obtained with scintillating detectors developed in other experiments, Table 2.2, the value obtained for TRITIUM-Aveiro 0 prototype is close the largest specific efficiency, obtained by Hofstetter. However this prototype has a worsen specific efficiency than other prototypes developed in TRITIUM experiment (TRITIUM-IFIC 1).

It can also be noted that the efficiency uncertainties obtained for this prototype are greater than those obtained in the previous TRITIUM prototypes. The reason of that is a difference in the measurement time. The measurement time used for the TRITIUM-Aveiro prototype is 1 minute, while that used for the previous prototypes is 10 minutes. Smaller uncertainties are achieved in the measured counts and, therefore, in the efficiency when longer measurements are taken.

Finally, as lower uncertainties in the measured counts allow a lower MDA to be achieved, longer measurements are studied to quantify the reduction of the MDA of this prototype. For this task, groups of 60 successive measurements are integrated, resulting in several measurements of 60 minutes. The acquired data is shown in Figure 7.7, where it can be checked a smaller relative uncertainty than the values for 1 minute.

In this case, the average and uncertainty of the measured background data are  $3.186 \cdot 10^{-4}$  and 228 counts per hour respectively. Using the equations 7.1 and 7.2, the values of  $L_C = 530$  and  $N_D = 1043$  counts per hour are obtained respectively. Assuming linearity between the measured counts for the background and the tritiated water,  $3.872 \cdot 10^4$  counts per hour, this  $N_D$  corresponds of a MDA of 4.53 kBq/L.

A diarly oscilation is clearly observed in the Figure 7.7, showing that the measurements are affected by external light. This oscilation begins on the 19<sup>th</sup> day, where the water closed circuit pump was installed, so it is

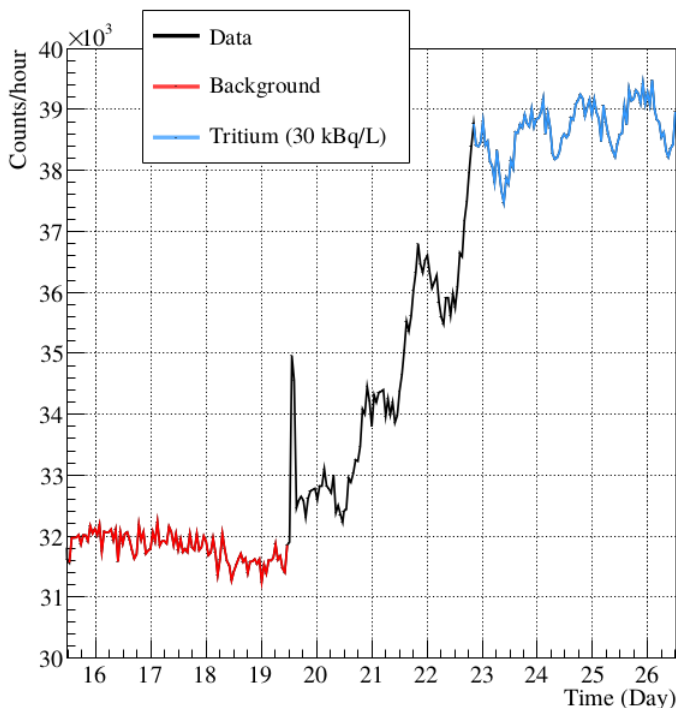


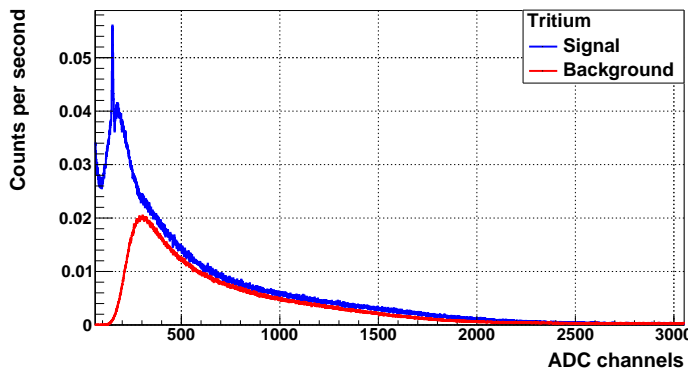
**Figura 7.7** – Measurements of the background and tritium liquid source (with an activity of 29.8 kBq/L) performed with the TRITIUM-Aveiro 0 prototype and integrated during an hour [151].

likely that the light leak is produced through this system.

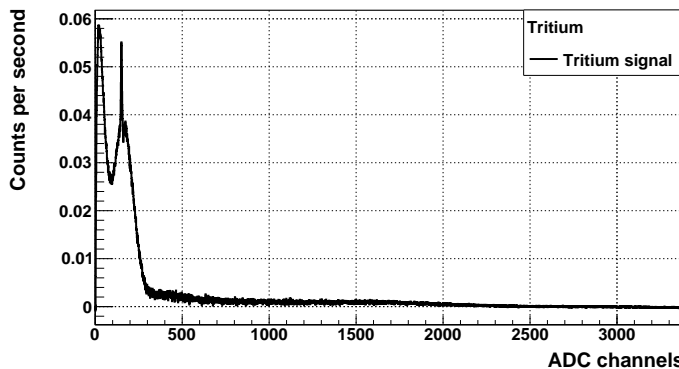
REVISAR LOS DATOS DEL APANTALLAMIENTO CON PLOMO.

#### 7.1.4 Experimental Results of TRITIUM-IFIC 2 prototype

This section shows the results of the lastest prototype developed in the TRI-TIUM experiment, TRITIUM-IFIC 2, during its installation in the Nuclear



(a) Signal and background energy spectra.



(b) Tritium energy spectrum.

**Figura 7.8** – Energy spectra experimentally measured with TRITIUM-IFIC 2 prototype.

Radiation Laboratory at IFIC. The design of this prototype is shown in section 5.2.2.

The energy spectra of the signal and background prototypes were measured, which are shown in Figure 7.8a. As it was mentioned in section 5.2.2, the signal prototype was filled with a tritiated water solution with an activity of 10 kBq/L and the background prototype was filled with ultrapure water.

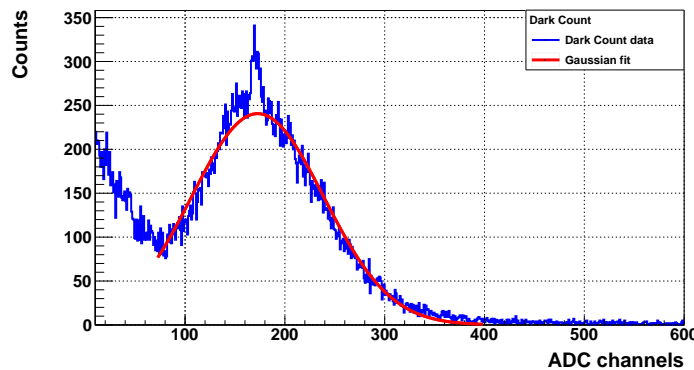
A difference between both signals is clearly visible, which corresponds to the energy spectrum of tritium, Figure 7.8b. The number of counts per second obtained for both, the signal and background, are  $19.05 \pm 0.18$  and  $11.54 \pm 0.14$  respectively. Therefore,  $7.11 \pm 0.23$  counts per second was obtained for the tritiated water source used.

The tritium detection efficiency obtained for this prototype is  $(7.11 \pm 0.28) \cdot 10^{-1} \frac{\text{c/s}}{\text{kBq/L}}$ , calculated from the quotient of both, the counts per second measured and the specific activity of the tritium liquid source used. This efficiency is larger than all scintillating detectors developed so far, including the prototypes developed in TRITIUM experiment, Table 2.2 and sections 7.1.1, 7.1.2 and 7.1.3. It is an expected result since the active area used in this prototype is larger than those used in others.

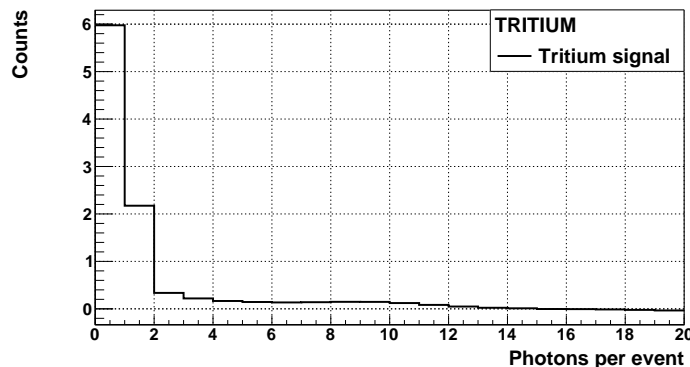
To remove the effect of different active area, the specific efficiency is measured, obtaining a value of  $(1.59 \pm 0.48) \cdot 10^{-5} \frac{\text{c/s}}{\text{kBq/L cm}^2}$  for this prototype. Again, it can be observed that this prototype has the largest specific efficiency obtained so far with a scintillating detector used for tritium detection.

Therefore, as it has demonstrated, the intrinsic and specific efficiency obtained so far for scintillating detectors used for tritium detection has been exceeded with the last TRITIUM prototype, TRITIUM-IFIC 2.

As discussed in chapter 4, the energy spectrum is shown in ADC units, proportional to energy, since it is difficult, even impossible, to calibrate a plastic scintillator due to its large relative uncertainty in the number of photons produced per event. Nevertheless, a detector calibration can be performed to express the results in units of photons detected per event. It was carried out using the single-photon distribution of the used PMTs, which was obtained from their self-emissions. Similar to the TRITIUM-Aveiro 0 prototype, the PMT used to read this prototype was decoupled to the prototype and covered with a special black blanket to ensure that



(a) Single photon distribution.



(b) Tritium energy spectrum.

**Figura 7.9** – Tritium measurement with TRITIUM-IFIC 2 prototype and expressed in photons detected per event.

external photons did not reach the PMT. The output signal of the PMT was analyzed using the electronical chain, the design of which is shown in Figure 3.14a. The distribution measured is shown in Figure 7.9a, in which a gaussian function was fitted.

As can be seen, the mean and uncertainty of the signal produced for a single photon detected with the PMT used are 172.71 and 66.19 (in ADC units) respectively. Therefore, the tritium signal, Figure 7.8b, can be expressed in number of photons detected per event, Figure 7.9b, by

simply dividing this spectrum by the mean measured for the single-photon distribution.

As can be seen, a maximum of 15 photons are generated per tritium event, which is in accordance with the expected result taking in to account the efficiencies involved.

Finally, a monitoring of both prototypes, signal and background, were carried out for several months, the measurements of which are shown in Figure 7.10.

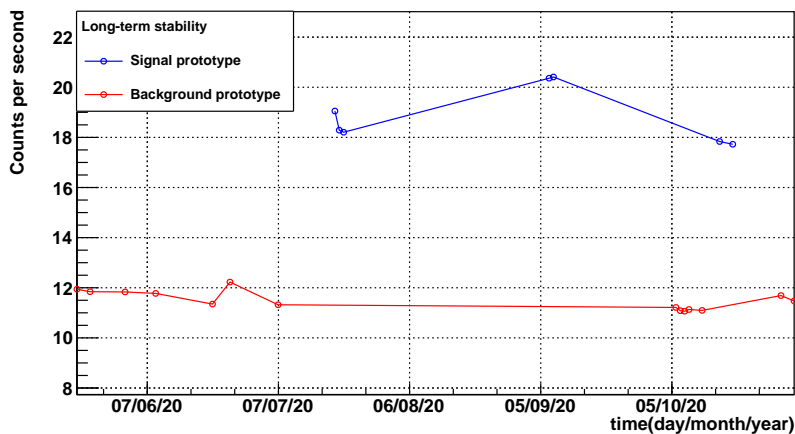


**Figura 7.10** – Monitoring of the signal and background prototypes for several months.

As can be seen, the signal of both was not reduced, ensuring the maintainance of the detector efficiency during 3 months for the signal and 6 months for the background.

## 7.2 Results from Measurements at Arrocampo dam

This section shows the measurements obtained with the TRITIUM-Aveiro 0 prototypes during their installation in the Arrocampo dam, which has been the only prototype installed in Arrocampo dam so far. This prototype was installed and working there for more than four months, from March 27, 2019 to August 18, 2019, during which time this prototype was taking background measurements. The data adquired during this time are shown in the figure 7.11, the measurement time of which is 60 minutes.

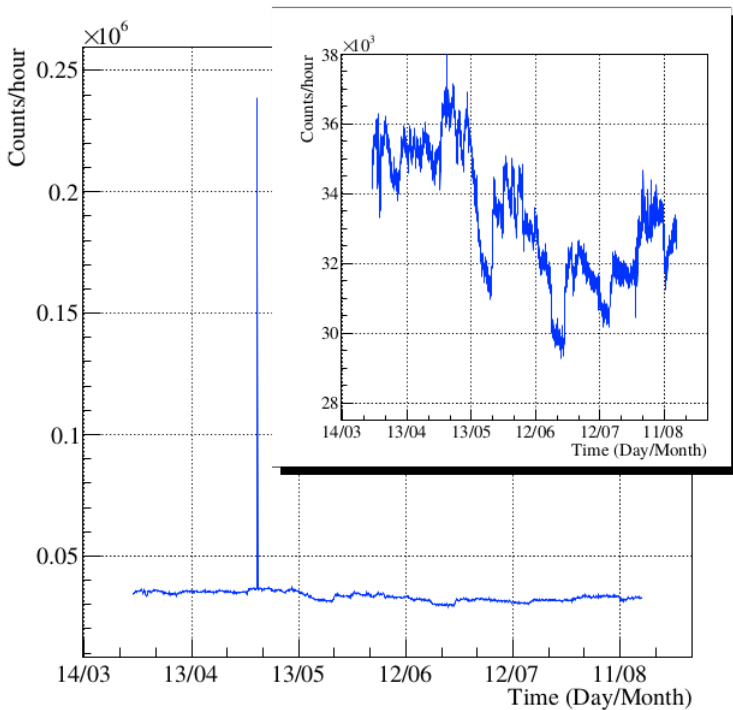


**Figura 7.11** – Background measured with the TRITIUM-Aveiro 0 prototype during its installation in Arrocampo dam [151].

This data shows good stability in the working months, measuring

a mean value of around 9.31 counts per second. A large peak is observed on May 2, 2019, caused by an opening of the roof of the lead shield to access the prototype. In the small box of the figure, the data is zoomed for a better visualization. The MDA measured in Arrocampo dam for 60 minute integration counting data is 6 times larger than that calculated in section 7.1.3. This variations can be caused by electric noise produced by the electric pumps of the water purification system and instabilities observed in the electronic boards.

A cosmic veto currently under development is planned to be installed and used in anti-coincidence with this prototype.

Furthermore, three TRITIUM-IFIC 2 prototypes and a cosmic veto, explained in section 5.2.2 and 3.4.2 respectively, are also planned to be installed in Arrocampo dam as soon as possible.

# Chapter 8

## Results of the TRITIUM Simulations

This chapter shows the results obtained in the simulations described in chapter 6, which is divided in two different sections. The first section contains the results of several simulations used to improve the design of the TRITIUM detector while the second exhibits the results obtained for the simulation of a full TRITIUM monitor based on an active veto read in anticoincidence with several TRITIUM-IFIC 2 prototypes. As shown throughout the different sections of this chapter, several tests were carried out to verify the correct simulation of the different steps such as the simulated tritium source, the energy deposition in the fibers and the production of photons in them.

## 8.1 Optimization of the TRITIUM Monitor Design

Several simulations were performed during the design of the TRITIUM detector, which were used to quantify the effect of some modifications and to choose those that optimize the tritium detection. The characteristics studied are the diameter and length of the scintillating fibers. As the tritium electrons has a very low mean free path, the shape of the simulated tritium source was also studied to reduce the consuming time and computing resources.

### 8.1.1 Optimization of the Tritiated Water Source

This section show and discuss the results obtained with the simulation described in section 6.2.1, the objective of which is to find the radial thick of the simulated tritium source that reduce the consuming time and computing resources used in the simulations.

First, the initial energy of the simulated tritium events are verified. For this task, the energy distribution of the simulated tritium electrons is obtained, shown in figure 8.1a, and compared with that obtained in the reference [145]. As can be checked, there is a good agreement between both.

In addition, a spectrum of the initial energy of tritium electrons that are capable of reaching the fiber and depositing energy are shown in Figure 8.1b, red histogram, which is compared to the energy distribution of all simulated tritium events, blue histogram. A shift to the right side in the red histogram is observed, creating a peak centred at 10 keV. This shift occurs mainly because the lower energy tritium electrons don't have enough energy to reach the fiber and overcome the water-fiber interface, producing

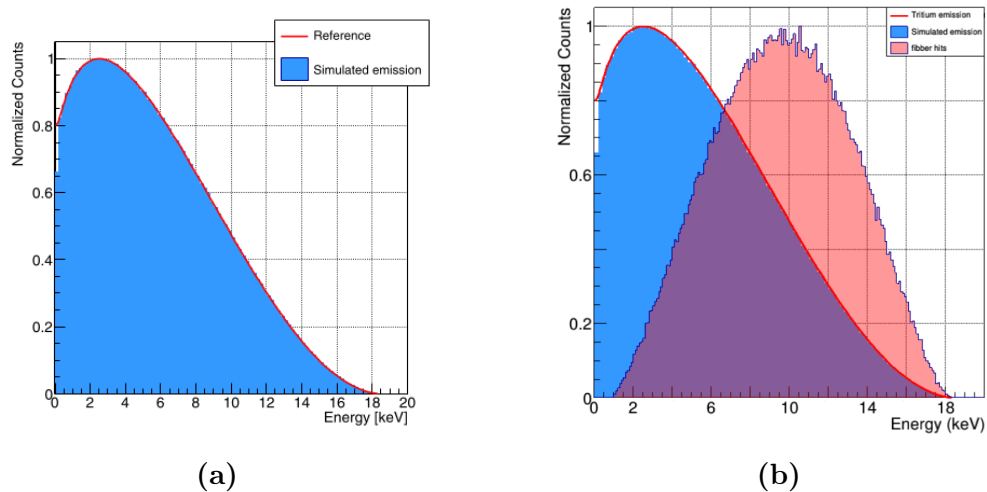


**Figura 8.1** – Energy distribution of a) simulated tritium decays b) Initial energy of tritium decays that reach the scintillating fibers (red histogram) compared the all simulated tritium events (blue histogram) [152].

a non-detected tritium event.

Regarding the radial thickness of the tritiated water source, Figure 8.2a shows a transversal cut of the 2 mm scintillating fiber, yellow, the simulated tritium source 0.5 mm thick around the fiber, green, and the tritium decays the electrons of which has deposited their energy in the scintillating fiber, red dots. Furthermore, the distribution of the radial distance between the position where tritium decays take place and the surface of the scintillating fiber are shown in figure 8.2b.

As can be seen in both figures, most of the tritium decays that are detected occur in close proximity to the scintillating fiber. A zoom is applied in the inset box of the Figure 8.2b for better viewing. The chosen thickness of the simulated tritium source is  $5 \mu\text{m}$  since the 99.4% of the events that are able to deposit energy in fibers are produced at least of this distance.

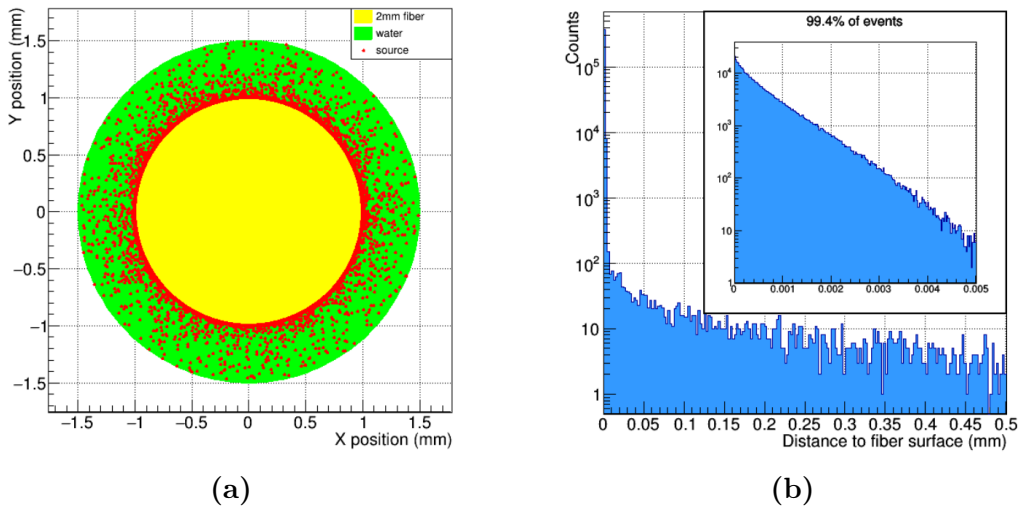


**Figura 8.2** – a) Transversal cut of simulated scintillating fiber (yellow) and tritium source (green) with various tritium decays (red dots) b) Distribution of the radial distance between the position where the tritium decay takes place and the surface of the scintillating fiber [152].

### 8.1.2 Simulation of the Output Light of Scintillating Fibers

As tritium electrons are far from being a MIP a quenching effect is produced in the output light generated by scintillating fibers, following the Birks law (equation 6.1). This quenching effect produces a reduction in the photons emitted by the scintillating fibers. The objective of this section is to quantify the significance of this effect and how it affects to the tritium detection.

First, a verification test of the energy deposition of tritium electron on scintillating fibers is carried out. In Figure 8.3 the initial energy of simulated tritium electrons that has reach the scintillating fibers, blue histogram, is compared with their energy deposited in scintillating fibers, red histogram.

A shift to the left side of the spectrum (smaller energies) is ob-

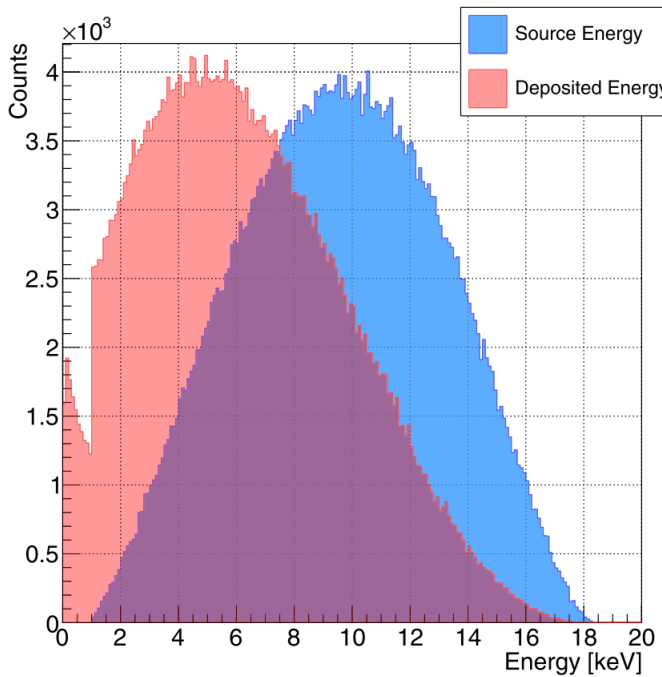


**Figura 8.3** – Distribution of the initial energy of tritium events that has reach the scintillating fibers, blue histogram, and the energy deposited, red histogram [152].

served between the blue histogram, with a peak around 10 keV, and the red histogram, with a peak around 5 keV. This displacement is mainly caused by the loss of energy of tritium electrons in the water. A cut of around 1 keV is observed in both energy distributions, produced by the default energy threshold of 990 eV that exist in the G4EmLivermorePhysics physics list.

Figure 8.4 shows two distributions of number of photons produced in scintillating fibers by tritium events, one in which the quenching effect has not been considered ( $k_B = 0$ ), red histogram, and other in which the Birks coefficient has been applied ( $k_B = 0.126 \text{ mm/MeV}$ ), blue histogram.

As expected, a distribution with a peak of around 40 photons per

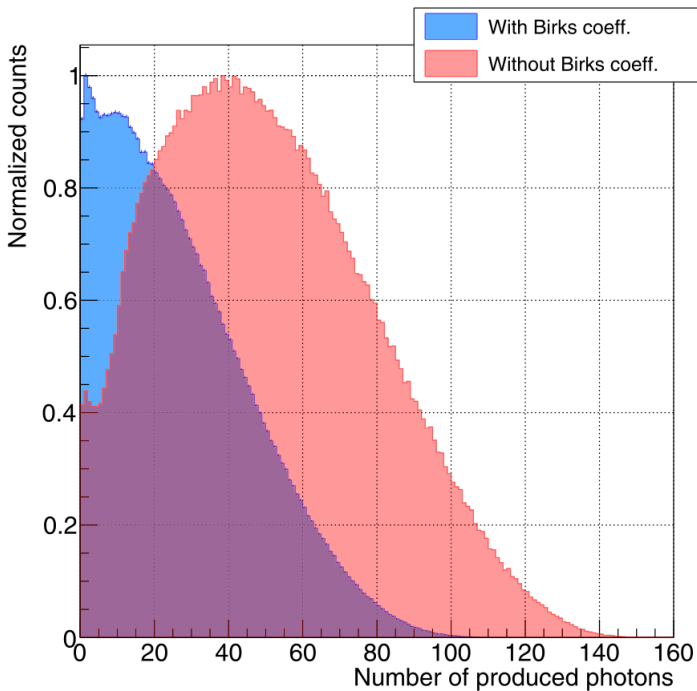


**Figura 8.4** – Energy distribution of photons produced by the scintillating fiber when the birks coefficient is not considered, red histogram, and when this is considered, blue histogram [152].

tritium event and a maximum of around 150 photons is obtained when the quenching effect was not considered. A significantly reduction of the output light is observed when the Birks coefficient is taken into account, producing a distribution with a peak centred around 10 keV and a maximum of 110 photons. The quenching effect is also observable in Figure 8.5, where the number of produced photons as a function of the energy deposited in the fiber is displayed in a bidimensional plot.

In this figure, in addition to a reduction of number of photons produced per energy deposited, a broader distribution is obtained when the Birks coefficient is considered, showing an increasement of the fluctuations of energy deposition.

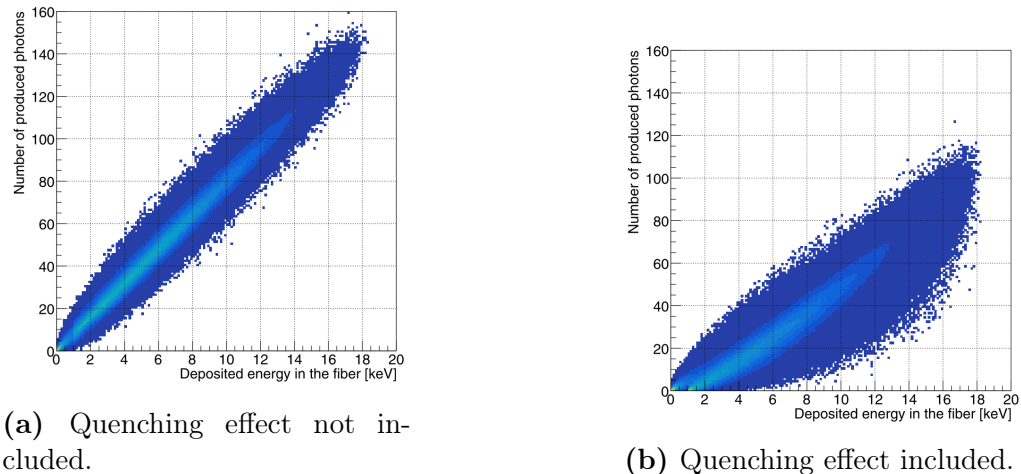


**Figura 8.5** – Number of photons produced in front of the energy deposited in the scintillating fibers when a)the birks coefficient is not considered ( $k_B = 0$ ) b) the Birks coefficient is considered ( $k_B = 0.126 \text{ mm/MeV}$ ) [152].

### 8.1.3 Optimization of the Scintillating Fiber Length

A study was carried out to choose the length of scintillating fibers that optimize the tritium detection efficiency. For this task, the complete TRITIUM-Aveiro 0 prototype was simulated, in which the photon propagation was included.

First, the propagation of photons in scintillating fibers was studied. The blue distribution of Figure 8.6 shows the number of photons produced in the fiber per tritium event that reaches them and the red distribution shows the same information but only for those events detected for both photosensors in time coincidence.

It can be seen that tritium events that produce a high number of photons are practically always detected but most of the events with fewer photons produced in the fibers are not detected, producing a peak centred of around 25 photons.

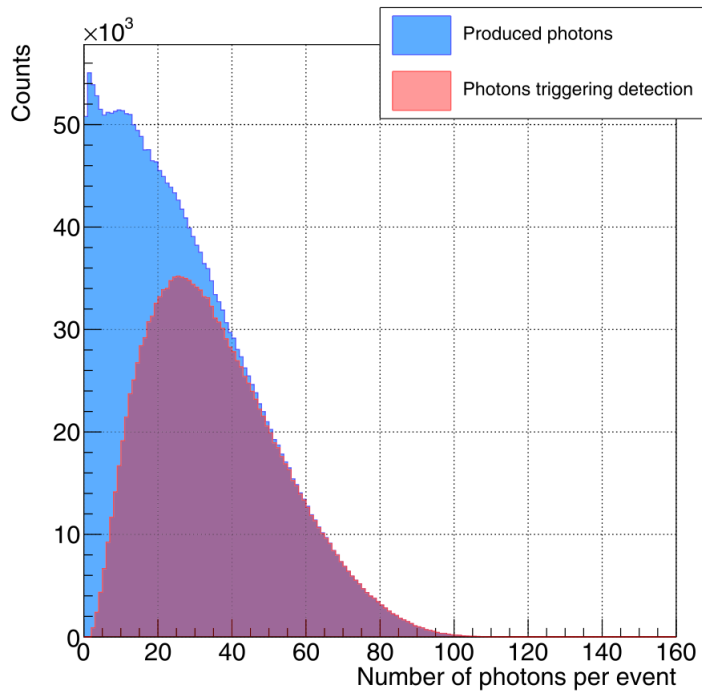


**Figura 8.6** – Number of photons produced in the fiber per tritium event for all tritium events that reach the fiber (blue histogram) and only for tritium events the photons of which are detected by photosensors (red histogram) [152].

Regarding the fiber length study, two different lengths were compared, 1 m and 0.20 m and two different tritium source activity were used, 0.5 kBq/L and 2.5 kBq/L. As detected tritium counts is proportional to the active area, 5 detectors were simulated for the case of 0.20 m fiber length to normalize the study to the same active area. The counts, which were integrated over 60 min and taken over a week, are shown in Figure 8.7.

A larger signal is seen for shorter fiber lengths in both cases, producing a increasement in tritium detection efficiency of approximately 25%, principally caused by a lower absorption of photons in shorter scintillating fibers and the leakage of some photons due to a non-perfect photon collec-

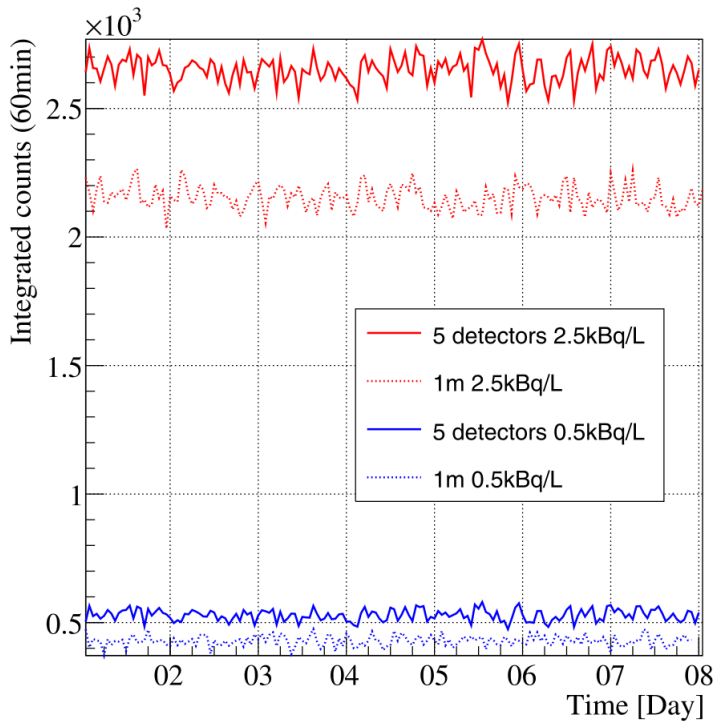


**Figura 8.7** – Counts integrated over 60 min, normalized to the same active area and taken over a week for a fiber length of 1 m, dashed lines, and 20 cm, solid lines and two different activities, 0.5 kBq/L, blue lines, and 2.5 kBq/L, red lines [152].

tion in the fiber.

#### 8.1.4 Optimization Scintillating Fiber Diameter

This study quantifies the effect of the scintillating fiber diameter on cosmic ray events detected. The energy deposited in the scintillating fiber by a cosmic ray event is proportional to the active volume crossed, which is larger for 2 mm fibers. Therefore, the cosmic ray signal obtained for a measured cosmic event will be larger for a detector based on 2 mm diameter. The

objective of this study is to find the design with which a lower background is obtained in the region of interest of tritium detection, ROI (up to 18 keV).

The distribution of energy deposited in scintillating fibers by cosmic ray events are shown in figure 8.8 for both cases, 1 mm and 2 mm fibers.

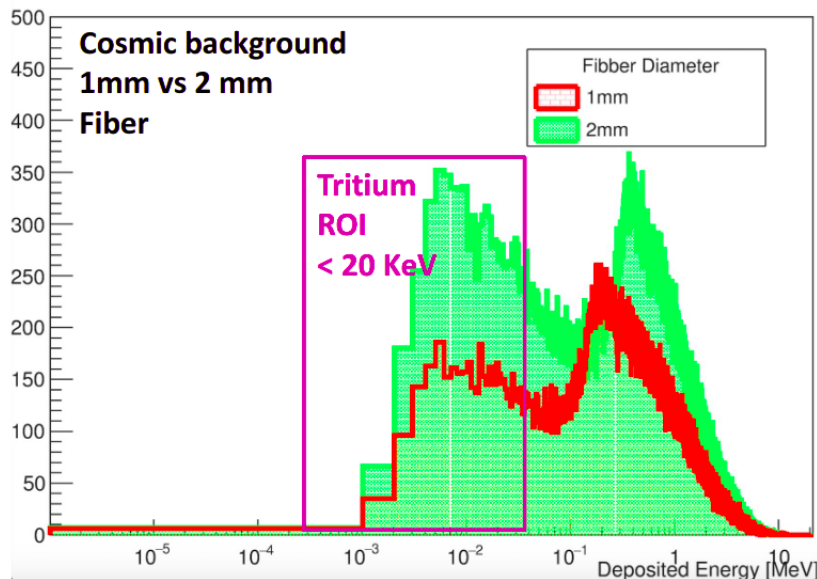


**Figura 8.8** – Comparison of the energy deposition of cosmic ray events in scintillating fibers of 1 mm and 2 mm in diameter.

As can be seen in the figure, a smaller background is measured for fiber diameters of 1 mm, which reduces the low detection level LDL of the detector. There are other reasons that favor the use of 2 mm fibers, such us their greater resistance and an improvement to the passage of water through them, so a experimental test is needed to choose the best design.

### 8.1.5 Effect of the PMMA windows

In the first prototypes, TRITIUM-IFIC 0 and TRITIUM-IFIC-1, the fibers were directly coupled to the photosensor, so the detected photons were only those guided by fibers. However, in the last prototypes, TRITIUM-Aveiro 0 and TRITIUM-IFIC 2, two PMMA windows are used, which allows the detection of photons guided by fiber and photons that come from the water medium.

To quantify the importance of this effect, the TRITIUM-Aveiro 0 prototype was simulated and the distribution of the number of photons that reach the PMMA per tritium event are shown in Figure 8.9. Fiber-guided photons are shown in a red distribution, while those traveling in the water medium are represented in the blue histogram.

It can be seen that the tritium signal obtained from the water is as important as that obtained from the fibers, contributing half of a signal. Therefore, an improvement in tritium detection efficiency is achieved using PMMA windows.

## 8.2 Simulation Results of TRITIUM monitor

This section shows the results obtained in the simulation of the TRITIUM monitor, consisting of a study of the tritium detection with various TRITIUM-IFIC 2 prototypes in parallel, section 8.2.1, and a study of the effect of the background rejection system, section 8.2.2.

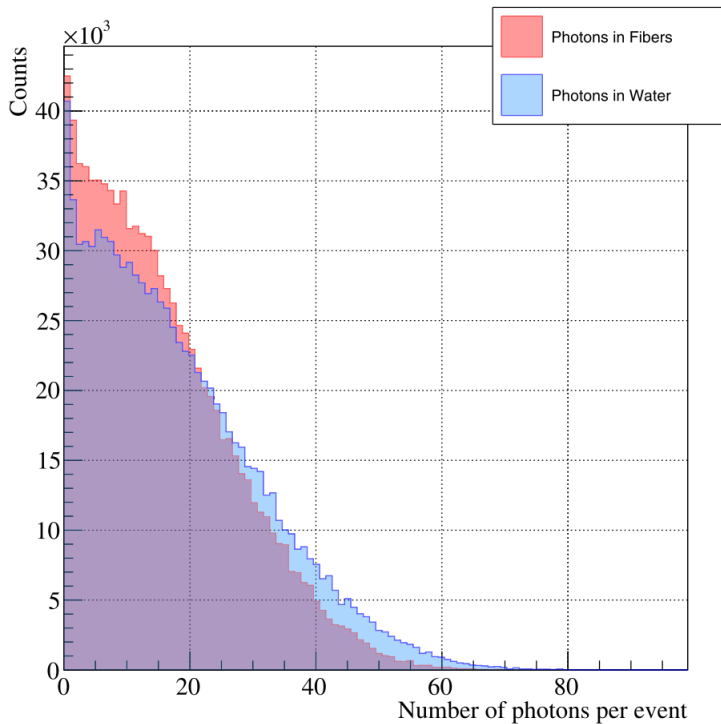


**Figura 8.9** – Distribution of photons reaching PMMA windows. The red histogram includes those guided by fibers and the blue histogram includes those traveling in the water medium [152].

### 8.2.1 Simulation Results of TRITIUM-IFIC 2

This section shows the results obtained with the simulation of the TRITIUM-IFIC 2 prototype, which was used for two different objectives. On the one hand, these simulations were carried out to find the Low Detection Limit, LDL, of this prototype for tritiated water activity, which is an important parameter to know the limitation of the prototype. On the other hand, these simulations serve to study the activity resolution of the prototype and how it can be improved through various parameters such as the increasement of the integration counting count time of the measurement and the number of prototypes read in parallel.

The detection of a tritium event by the TRITIUM-IFIC 2 prototype is shown in Figure 8.10, in which, the path followed by the photons created in scintillating fibers are represented by green lines which end in red dots when it is absorbed in the fiber or the water and blue dots when it is absorbed in the PMTs (detected). The fiber that has detected the tritium electron is clearly identified and the photons out of this are those that has not been collected due to the critical angle. Blue dots are obtained in both PMTs for this event, indicating that this is detected on time coincidence.

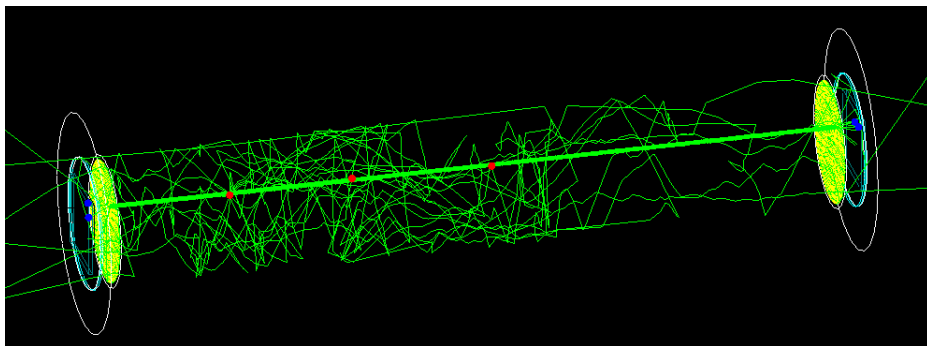


**Figura 8.10** – Tritium electron detected in the simulated TRITIUM-IFIC 2 prototype. The path of the optical photons is represented by green lines and the position in which it is absorbed is represented by red and blue dots (absorbed in water or PMT, respectively).

Several variables were used as tests in each simulated measurement to verify the different steps of the simulation such as the production of tritium events, the energy deposition in scintillating fibers and their subsequent photon emission, spatial distribution of generated events, detected events, etc.

The distribution of the number of photons detected by the PMTs per tritium event was obtained for the simulated TRITIUM-IFIC 2 prototype, shown in Figure 8.11.

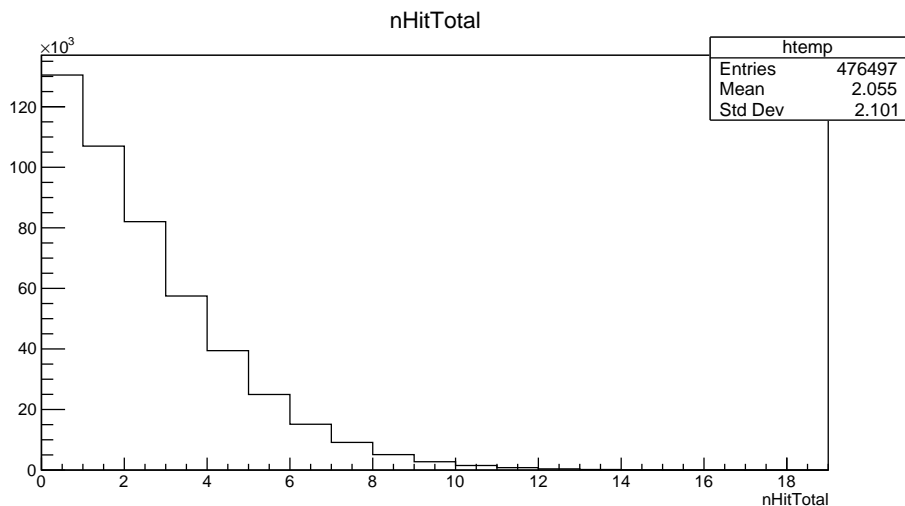
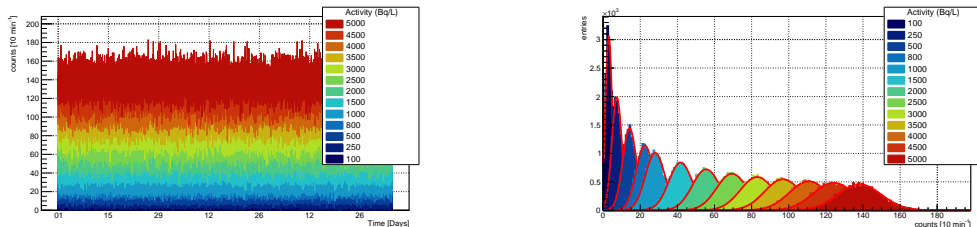


**Figura 8.11** – Photons detected by both PMTs per tritium event in the simulated TRITIUM-IFIC 2 prototype.

A maximum of 17 photons is obtained for the TRITIUM-IFIC 2 prototype simulations, which are in agreement with the maximum of 15 photons experimentaly measured by this prototype, displayed in Figure 7.9b. This confirms that the value used in the simulations for the Birks coefficient,  $k_B = 0.136 \text{ mm/MeV}$ , is adequate. The experimentally obtained distribution are a bit small between 3 and 8 photons, probably due to imperfections of the prototype which are impossible to simulate.

Various activities were simulated from 100 Bq/L to 50 kBq/L for



(a) Counts as a function of the time.

(b) Distribution.

**Figura 8.12** – Tritium counts detected with a simulated TRITIUM-IFIC 2 prototype using a integration counting time of 10 min a) as a function of the time b) distribution of them.

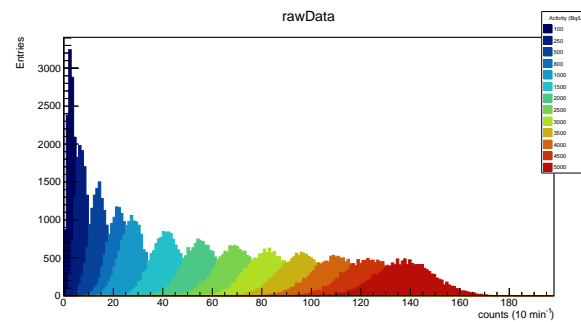
three months of simulated data taking and an integration counting time of 10 min was used.

The measurements obtained are presented in Figure 8.12a as a function of time, which are histogramed in Figure 8.12b. In this figure a zoom is applied from 100 Bq/L to 5 kBq/L (interesting range) for better visualization.

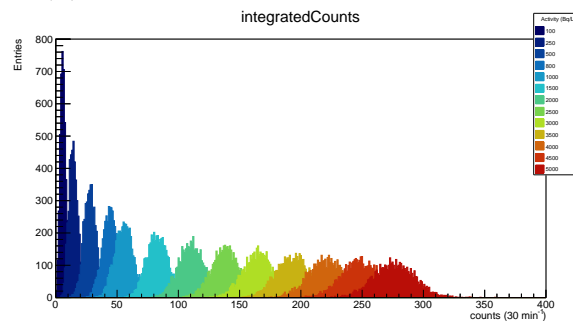
Difference of 250 Bq/L is not distinguished due to the overlapping of several distributions. To reduce the width of the distribution obtained for each activity, the statistics must be increased, which can be done in two different ways, increasing the integration counting time or increasing the number of prototypes read in parallel.

To check the effect due to an increase of the integration counting time similar distributions are obtained for three increasing integration counting times (10 min, 30 min and 60 min), which are shown in Figure 8.13.

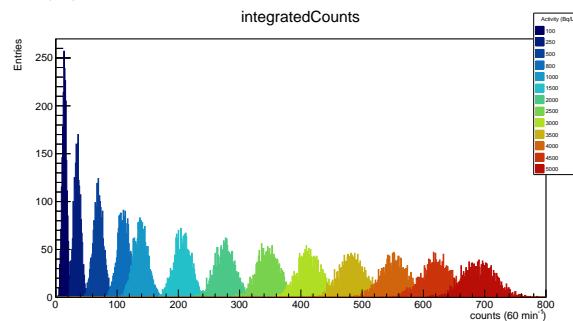
The effect of increasing the integration counting time is clearly visible in this figure, reducing the relative distribution width and improving the activity resolution of the TRITIUM monitor. Difference as low as



(a) Integration counting time of 10 min.



(b) Integration counting time of 30 min.



(c) Integration counting time of 60 min.

**Figura 8.13** – The distribution of the tritium counts detected with a simulated TRITIUM-IFIC 2 prototype for three different integration counting time, a) 10 min b) 30 min and c) 60 min.

250 Bq/L are clearly distinguished using only one detector and an integration counting time of 60 min, which we can still consider a quasi-real time measurement. Similarly, this distributions are shown in Figure 8.14 for 10 min of integration counting time, in which three increasing number of prototypes were read in parallel (1, 5 and 10).

Again the reduction of the distribution width is clearly visible in these figures, improving the activity resolution of the detector. In this case, differences of 250 Bq/L are clearly distinguished using a integration counting time of 10 min and measuring with 5 TRITIUM-IFIC 2 prototypes.

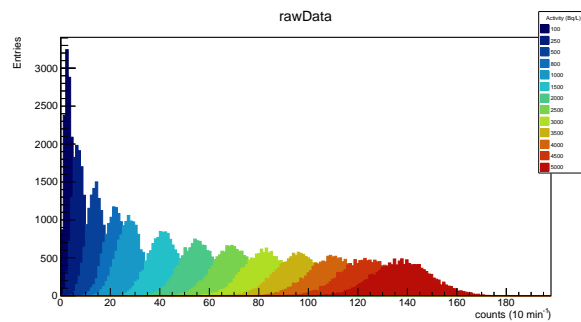
The effect on the resolution, defined as the equation 8.1, is also studied as a function of both TRITIUM monitor characteristics, integration counting time and number of used prototypes, and shown in Figure 8.15.

$$\text{Resolution}(\%) = \frac{\text{FWHM}}{\text{centroid}} \cdot 100 \quad (8.1)$$

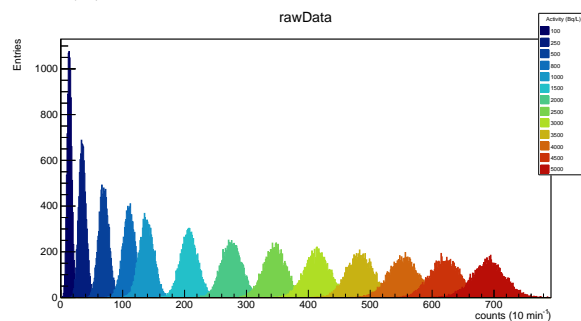
A growing improvement can be observed in both cases and, as can be verified with the lines in the figure, the resolution of both cases fit to the expected behavior of the inverse of the root of accounts.

Therefore, both characteristics must be balanced based on the requirements and financial budget of the experiment. The activity difference, the distribution peaks of which are clearly distinguished for each different case of integration counting time and number of detectors used, is summarized in Table 8.1.

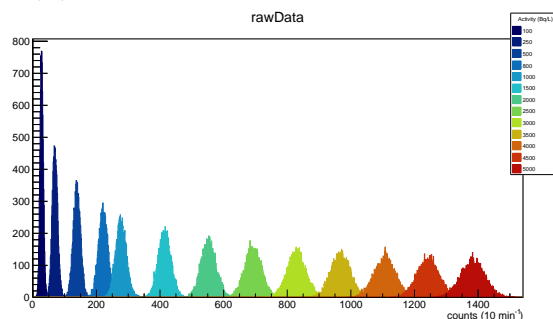
The decision made in the TRITIUM experiment is to install 3 different TRITIUM-IFIC 2 prototypes, with which differences of 250 Bq/L are expected to be distinguished using an integration counting time of 30 min. These prototypes are expected to be installed in Arrocampo dam as soon as possible. Two other TRITIUM-Aveiro 0 prototypes are being built and will be installed soon, alongside the one currently installed.



(a) One TRITIUM-IFIC 2 prototype.



(b) Five TRITIUM-IFIC 2 prototypes.



(c) Ten TRITIUM-IFIC 2 prototypes.

**Figura 8.14** – The distribution of the tritium counts detected with several simulated TRITIUM-IFIC 2 prototypes a) 1, b) 5 and c) 10 for an integration counting time of 10 min.

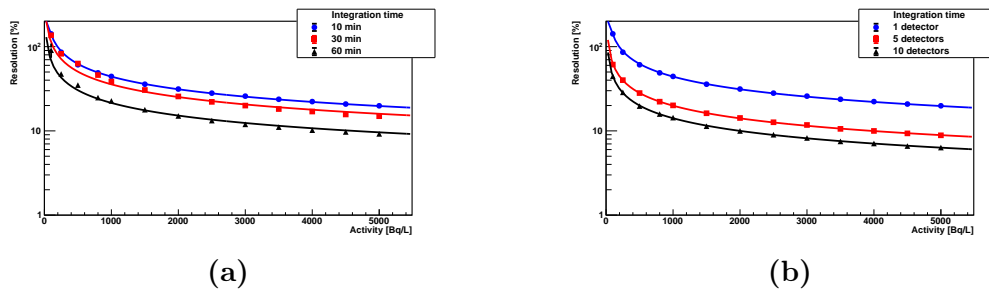


**Figura 8.15** – Resolution of the TRITIUM-IFIC 2 prototype as a function of the a) integration counting time b) number of prototypes.

# of Detectors	10 min	30 min	60 min
1	< 1000 Bq/L	500 Bq/L	200 Bq/L
5	200 Bq/L	150 Bq/L	100 Bq/L
10	150 Bq/L	100 Bq/L	≈ 50 Bq/L

Table 8.1: Difference in activity that can be clearly distinguished for various cases of the TRITIUM-IFIC 2 prototype based on different integration counting times and different number of prototypes.

### 8.2.2 Simulation Results of Background Rejection System

Finally, this section shows the results obtained with the simulation of a TRITIUM-IFIC 2 prototype when the background rejection system, detailed in section 6.2.6, is included. These simulations quantify the effect on the tritium measurement of both parts of the background rejection system, lead shield and cosmic veto.

Similar to the simulations used for the study of the TRITIUM-IFIC 2 prototype, analogous variables were used as tests, which were systematically verified, to ensure that all the steps of the simulations were carried out correctly.

Three different simulations were carried out to independently quantify how the tritium detection is affected due to both, the lead shield and the cosmic veto. The first simulation consists of a TRITIUM-IFIC 2 prototype and the cosmic ray source, in the second simulation a lead shield was added and for the third simulation, the cosmic veto was also included.

The cosmic events detected by the TRITIUM-IFIC 2 prototype are reduced around 5.5 times when a lead shielding with walls of 5 cm is included. This reduction is mainly caused due to the stop of the weak cosmic radiation (energy lower than 200 MeV).

About 10% of the cosmic events that pass through the lead shield and reach the TRITIUM IFIC 2 prototype are detected with the cosmic veto and, therefore, removed to the tritium measurement.

# Chapter 9

## Conclusions and Prospects

Punto 4.3 del paper de simulacion de carlos.

Conclusiones de los papers de carlos. Conclusiones de nuestros papers. Conclusiones presentaciones.

Que cosas se han conseguido en este experiemnto? -> DEcir que tanto l oque se ha conseguido con el detector como con las investigaciones de componentes del detector (capitulo 3)

Responder a las grandes preguntas:

- Podemos medir tritio?
- Lo podemos hacer en tiempo quasi real?
- Lo podemos hacer a la actividad que queríamos?
- Que sensibilidad se ha llegado a conseguir?
- Estabilidad temporal?
- Precio?

- Comparación con respecto al resto de experimentos? -> Poner la tabla 1.8 pero incluyendonos
- Efecto del shield
- Efecto de los vetos
- Efecto de ambas cosas
- Medidas a varias actividades

Hemos llegado a detectar 30 kBq/L con Tritium-Aveiro y se espera llegar a medir hasta menos de 5 kBq/L (superando los actuales limites).

Hemos llegado a detectar 10 kBq/L con Tritium-IFIC 2 (superando los actuales limits) y se espera llegar a medir incluso menos.

Ambos valores, lejos de ser el objetivo del proyecto, sirven para una monitorización en tiempo quasi real. Además, con el monitori final que consiste en varios modiules de estos en apralelo, se pretende llegar al objetivo deseado.

Tenemos datos de tritio en el agua bruta (agua del río) de esa zona desde 1998, pero tengo que solicitar permiso para poder dártelos. En cualquier caso, hay otra manera de conseguirlos, que es a partir de los informes del CSN al Congreso de los diputados (web CSN). Desde 2015 la concentración de tritio en el agua del río Tajo ha disminuido considerablemente porque la CNA instaló unos enfriadores por convección que emiten parte del H3 a la atmósfera. -> Tesis de Antonio Rodríguez y de Elena García.

El prototipo más avanzado hasta la fecha ha sido el de Aveiro. Prometedores resultados se estan obteniendo con el último prototipo, IFIC 2.

Como se ha dicho, se leerán varios prototipos en coincidencia, lo cual aumenta el área activa del detector. Esto nos permite obtener un mayor número de cuentas para una misma actividad de la fuente ya que estas depende linealmente del área activa, mejorando la eficiencia del detector y permitiéndonos llegar a LDLs más bajos. Sin embargo, no se espera que la eficiencia específica del detector se mejor ya que esta no depende del área activa.

Además el uso de los vetos activos nos permitirá reducir el nivel de background de la muestra. Dado que se espera que la incertidumbre relativa del background se mantenga, obtendremos incertidumbres más pequeñas, dando lugar a menores MDAs.

Study	$\varepsilon_{det}(\frac{cps \cdot 10^{-3}}{kBq/L})$	$F_{sci}$ (cm <sup>2</sup> )	$\eta_{det}(\frac{cps \cdot 10^{-6}}{kBq/L \cdot cm^2})$	LDL (kBq/L)
Muramatsu	0.39	123	3.13	370
Moghissi	4.50	> 424.1	< 10.6	37
Osborne	12	3000	4	37
Singh	41	3000	13.7	< 37
Hofstetter	2.22	~ 100	< 22.2	25
T-IFIC 0	$2.11 \pm 0.85$	219.91	$9.59 \pm 3.87$	100*
T-IFIC 1	$38.42 \pm 1.61$	402.12	$95.55 \pm 4.01$	100*
T-Aveiro 0	$64.87 \pm 19.41$	4071.50	$15.93 \pm 4.77$	29.8
T-IFIC 2	$711.03 \pm 27.77$	5026.55	$141.45 \pm 5.52$	10*

Table 9.1: Results of different scintillator detector for tritiated water detection. This table shows the efficiency of the detector ( $\varepsilon_{det}$ ), its active surface ( $F_{sci}$ ), its specific efficiency ( $\eta_{det} = \varepsilon_{det}/F_{sci}$ ), defined as its efficiency normalized to its active surface, and its low detection-level (LDL) for each study listed above. The "\*" symbol indicates that this is the specified activity that the detector can distinguish from the background, but it is not its LDL.



# Appendices



## Appendix A

# Electronical Schemes of PCBs Used for SiPM Characterization

Y más cosas aún.



# Appendix B

## Ultrapure Water System

In this appendix I show several photos of the ultrapure water system in the same order that the water flows through them.

First of all, the complete scheme of the ultrapure water system is shown in Figure B.1:

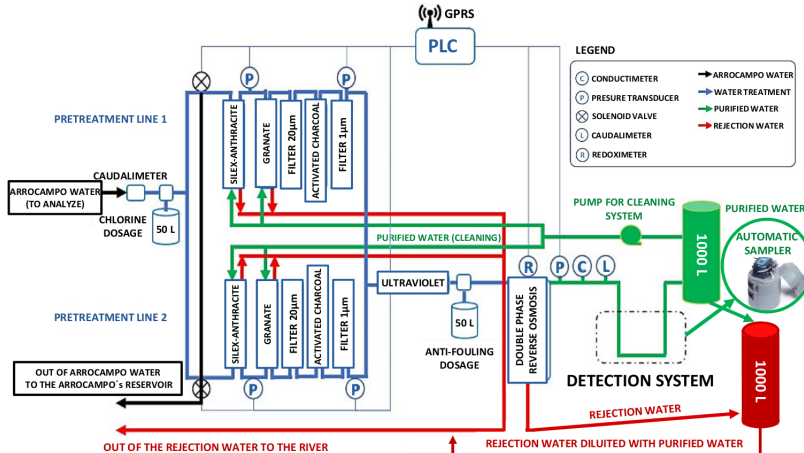


**Figura B.1** – Scheme of the ultrapure water system.

Secondly, the Gross filtering stage, made up of Silex-Antracite and

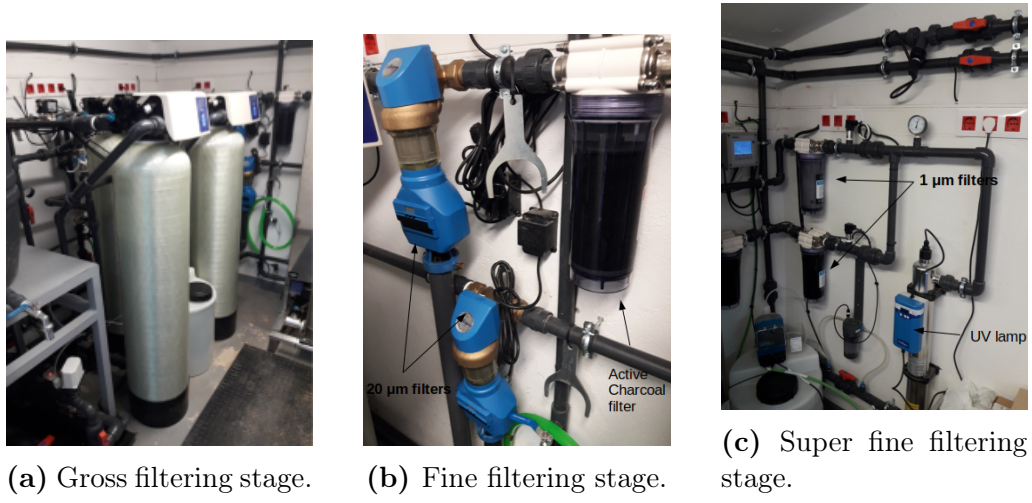


**Figura B.2** – Different stages of filtration of the ultrapure water system.

Granate filters, is shown in Figure B.2a:

In third place, the fine filtering stage, consisting of  $20\text{ }\mu\text{m}$  filter and active carbon filter, is shown in Figure B.2b:

In fourth place, the superfine filtering, composed of the  $1\text{ }\mu\text{m}$  filter and the UV lamps, is shown in Figure B.2c

In fifth place, the double phase reverse osmosis is shown in Figure B.3a

In sixth place, the containers in which we store the ultrapure water and the reject water after treatment is shown in Figure B.3b.

In seventh place, the Siemens PLC, software used to control the ultrapure water system, is shown in Figure B.4.

Finally, the complete system of the ultrapure water system is shown in Figure B.5



(a) Doble phase reverse osmosis stage.



(b) Storage containers of reject and ultrapure water.

**Figura B.3** – Doble phase reverse osmosis stage and containers used to store the outlet water of the ultrapure water system.



(a)



(b)



(c)

**Figura B.4** – Siemens PLC, software for remote control of ultrapure water system.



**Figura B.5** – General photo of the complete ultrapure water system.

Just as a curiosity, the three types of water (raw water, rejection water and ultrapure water) are shown in Figure B.6, where you can visually check the difference in the turbidity of each type of water.

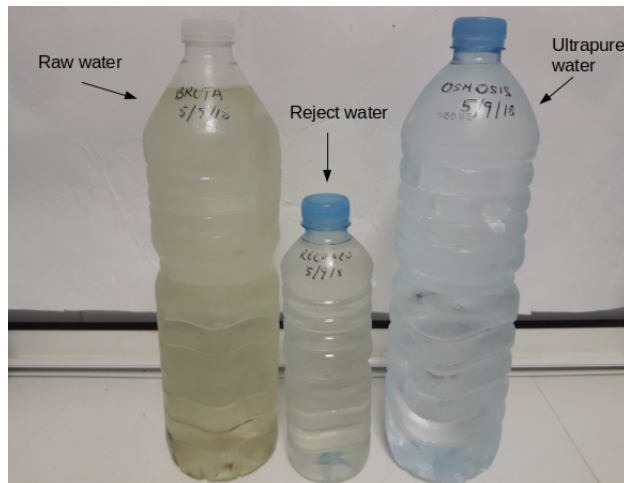


**Figura B.6** – Raw water, reject water and ultrapure water obtained with this system.

# Appendix C

## Preparation of Liquid Radioactive Source of Tritium

To prepare this radioactive liquid source, 1.86 g (uncertainty of 0.05%) of tritium was purchased from the Germany company PTB<sup>1</sup>, which has a serial number of 2005 – 1442 and reference number of PTB-6.11 – 285/03.2017 [130]

The activity of this tritium source is 26,8 MBq/g (uncertainty of 2.24%), reference data of 1 of January of 2017, and it was dissolved in 500 mL (uncertainty of 0.05%) of ultrapure water, giving 500 ml of tritium water, to which we will call standard solution, with an activity of 100.096 kBq/g (uncertainty of 2.24%), that's, 99.696 kBq/L (uncertainty of 2.24%), which was measured with the TRI-CARB 2810 system, based on liquid scintillation readout by PMT.

---

<sup>1</sup>Physikalisch-Technische Bundesanstalt, Braunschweig and Berlin, Germany

204APPENDIX C. PREPARATION OF LIQUID RADIOACTIVE SOURCE OF T

# Appendix D

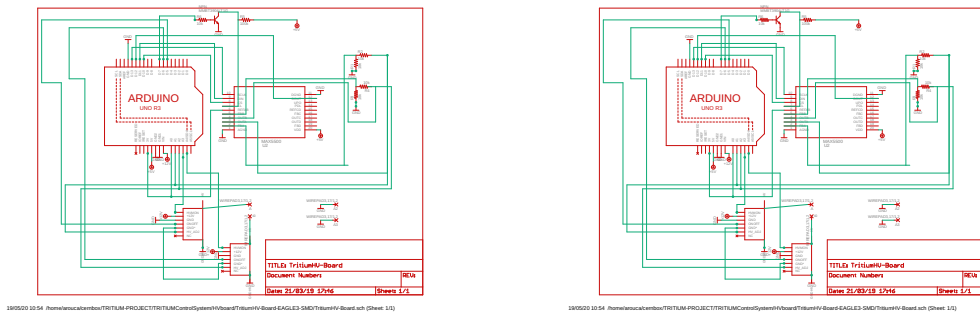
## Electronic System of TRITIUM-Aveiro 0 prototype

The electronic system used in TRITIUM-Aveiro 0 prototype consists of several PCB and can be divided into two parts:

1. A PCB, whose electronic scheme is shown in Figure D.1, was designed to power the PMTs with a negative high voltage. It consists of several high voltage power supply, model C11152-01 from Hamamatsu company [133], one for each PMT used, which is controled by a DAC<sup>1</sup>, model MAX5500 from Maxim Integrated company [134]. An Arduino Mega is used for the DAC communication and cross-checking the output values and it is connected to a Raspberry Pi to control the system.  
A graphical interface, shown Figure D.1b, has been developed to manage the different options of this system in a comfortable way.
2. A electronical chain consisting of several PCBs was used to process and analyze the system signals, whose simplified electronic scheme is

---

<sup>1</sup>DAC, Digital-to-analog converter



(a) Electronic scheme of the PCB.

(b) Graphical user interface.

**Figura D.1** – Electronic scheme of the PCB designed to power the PMTs of Aveiro prototype and the graphical user interface developed to control it.

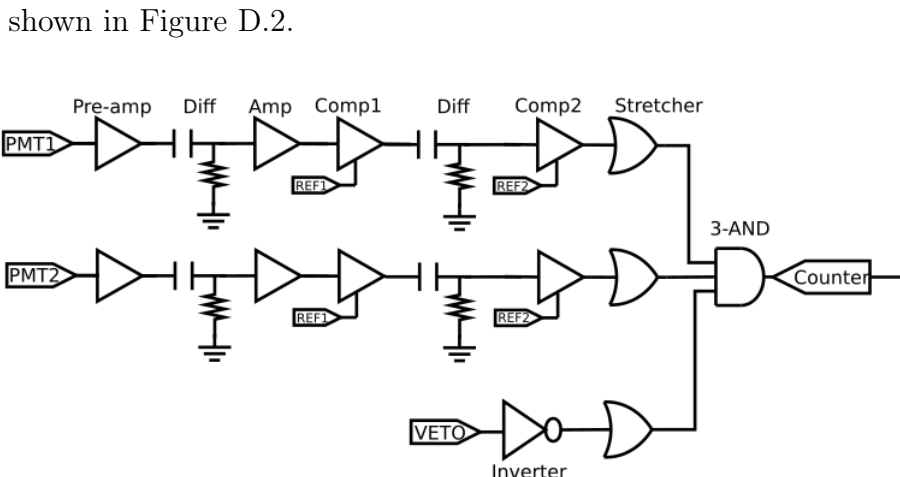


**Figura D.2** – Simplified electronic scheme used to process and analyze the signal of TRITIUM-Aveiro 0 prototype.

It consists of three different lines, two of them are used for the PMT signals of the prototype and the remaining line is used for doing anti-coincidence with a active veto.

To test this electronic chain a plastic scintillation with dimensions of  $10 \cdot 10 \cdot 1 \text{ cm}^3$  was used to simulate a veto signal but four different vetos are being developed, each one is based on a rectangular plas-

tic scintillations of Saint-Gobain company [135], whose dimensions are  $50\text{ cm} \cdot 30 \cdot 2\text{ cm}^3$  with a PMT coupled, model R2154-02 2" from Hamamatsu company [132]. The output signal of these PMTs will be input in a OR stage, whose response will be introduced in the veto line shown previously in Figure D.2. As a result, each plastic scintillator will be read in anticoincidence with tritium-Aveiro prototype.

Both lines, used to process and analyze the PMT signals of the prototype, are equal and they are used to operate in time coincidence. First, each PMT signal is introduced in a prepamplifier model CR111 from CREMAT Inc. company [136], which is used to shape and pre-amplify the signal. To reduce electronic noise and signal loss, both preamplifiers are connected as close as possible to the PMTs and they are located inside of aluminum boxes which act like a Faraday cage.

Each preamplifier is followed by a differentiation stage, which is used to reduce the time width of the signal, and amplification stages, used to amplify the signal. The amplification used is the model OPA656 from Texas Instruments [137].

Then, a fast comparator, model LT111 from Linear Technology company [138], is used to set a threshold which will be used to remove the PMT signals whose amplitude are below this value (dark counts of the PMT). A MAX5500 DAC is used to configure the thresholds.

The time width of the preamplifier output signal is too large,  $200\text{ }\mu\text{s}$ , so which too many false coincidence will be registered. To solve this problem a second differentiation stage is included and a second comparator are added to produce a 5V square signal again.

Finally a tunable pulse stretcher based on an OR gate, model SN74AHC1 from Texas Instruments company [139], is used to set the time width of each signal at 100 ns, with which the time coincidence windows of our acquisition system is 200 ns, narrow enough to have a negligible false coincidence rate.

In the remaining line, used for the veto signal, an inverter is used in

the first stage. With it, the signal will always be in the high level, 5 V, except when a cosmic particle is detected, in which case the signal will be in the low level, 0 V. Then, another stretcher is used to create a signal with the same time width than the others, 100 ns.

Lastly, these three signals are introduced into a 3-input AND gate, model SN74LVC1G11 from Texas Instruments company [140], to perform a logic level comparison. With this last stage we achieve a temporal coincidence of both PMT signals of the prototype and anti-coincidence of them with the veto signal. The output signal of this last stage is simply connected to a pulse counter.

A GPIO pins of a Raspberry Pi is used to communication with the system, control it and configure the different threshold levels and a graphical user interface, whose appearance is shown in Figure D.3, has been developed to manage in a comfortable way the counter system.

In addition to count, which is the option normally used in our detector, this electronic system include a voltage follower circuit connected to the preamplifier output signal which can be used to obtain a energy spectrum of each PMT of the prototype.

It is important to note that, although this system has a graphical user interface that allows comfortable control of the system, the usual way in which it is controlled is remotely through the computer terminal.

In Figure D.4 two screenshots are shown to demostrate two different situations of this system. There, we have four different signals. The yellow and cyan signal are input signals of the AND-Gate, which come from the PMT signals of the prototype. The pink signal is the third remaining input signal of the AND-Gate, which come from the PMT signal of the veto. The last signal, green, is the output signal of the AND-Gate.

As can be seen, in Figure D.4a both PMTs of the prototype have detect a time coincident event, which has not been detected for the veto, so this event is counted. In Figure D.4b, a time coincidence

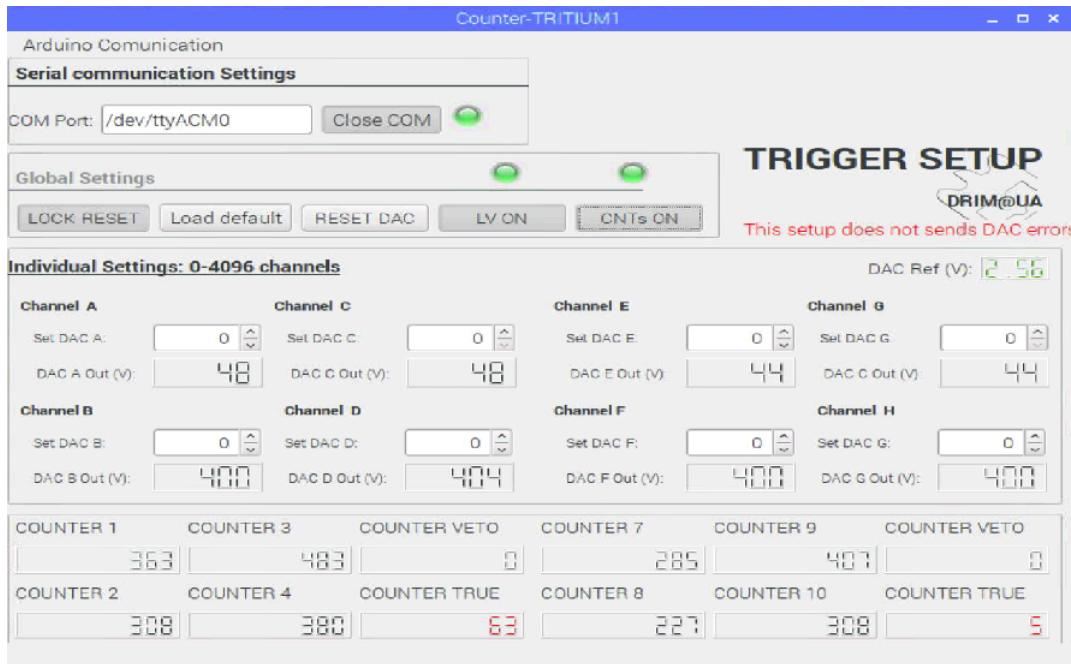
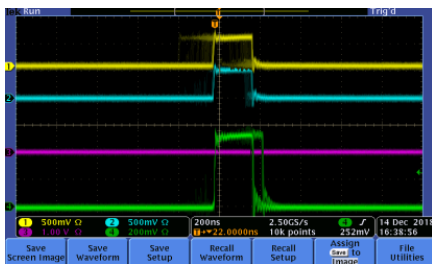
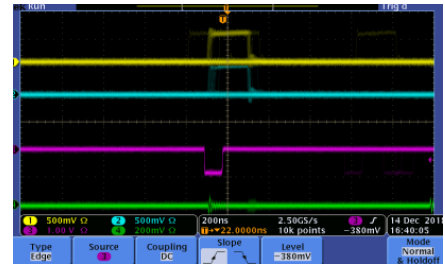


**Figura D.3** – Graphical user interface used to manage the counter system.

event has been observed in the three PMTs, which means that it is a cosmic event, so this event is not counted.



(a) Event accepted by the electronic system.



(b) Event rejected by the electronic system.

**Figura D.4** – Two different situations of the electronic chain response. A.- Event accepted since veto has not detected it. B.- Event rejected since veto has detected it

# Bibliography

- [1] IAEA, *The International Atomic Energy Agency Webpage*.
- [2] UNSCEAR, *The United Nations Scientific Committee on the Effects of Atomic Radiation Webpage*.
- [3] CSN, *Consejo de Seguridad Nuclear, Spain Webpage*.
- [4] ICRU, *International Commission of Radiological Units and Measurements Webpage*.
- [5] ICRP, *International Commission on Radiological Protection Webpage*.
- [6] ISR, *International Society of Radiology Webpage*.
- [7] UN, *United Nations Webpage*.
- [8] CSN, *Red de Estaciones Automáticas, REA Webpage*.
- [9] CSN, *Red de Estaciones de Muestreo, REM Webpage*.
- [10] *Council directive 2013/15/euratom*.
- [11] J. W. BERTHOLD, L. A. JEFFERS, *Phase 1 Final Report for In-Situ Tritium Beta Detector*, U. S. Department of Energy, McDermott Technology, Inc., Research and Development Division, **DE-AC21-96MC33128**, April, 1998.

- [12] J. W. BERTHOLD, L. A. JEFFERS, *In Situ Tritium Beta Detector*, U. S. Department of Energy, McDermott Technology, Inc. (MTI), Technology development data sheet, **DE-AC21-96MC33128**, May, 1999.
- [13] X- HOU, *Tritium and  $^{14}C$  in the environmental and nuclear facilities: Sources and analytical methods*, Journal of the Nuclear Fuel Cycle and Waste Technology (JNFCWT), 16 (2018), 11-39 **DOI: 10.7733/jnfcwt.2018.16.1.11**.
- [14] REFERENCIAAAAAAAA.
- [15] *Avance del informe del sistema eléctrico español, 2019*, Red eléctrica española.
- [16] *China construirá 60 centrales nucleares en la próxima década*, Europa press.
- [17] *Inversión de EE. UU. de 35 millones para centrales nucleares*, Energy News
- [18] *Three mile island accident*, World Nuclear Association.
- [19] *International Energy Outlook 2013*. U. E. Energy Information Administration.
- [20] Tritium at Fermilab.
- [21] **Brookhaven National Laboratory (BNL)**.
- [22] ALEKSANDRA SAWODNI, ANNA PAZDUR, JACEK PAWLÝTA, *Measurements of Tritium Radioactivity in Surface Water on the Upper Silesia Region*, Journal on Methods and Applications of Absolute Chronology, Geochronometria, Vol. 18, pp 23-28 **2000**.
- [23] M. L. OLIPHANT, P. HARTECK and E. RUTHERFORD, *Transmutation Effects observed with Heavy Hydrogen*, Nature, 133, 413 (1934)**DOI: 10.1038/133413a0**.

- [24] LUIS W. ALVAREZ and R. CORNOG, *Helium and Hydrogen of Mass 3*, Physical Review Journals Archive, 56, 613 (1939) DOI: [10.1103/PhysRev.56.613](https://doi.org/10.1103/PhysRev.56.613).
- [25] *DOE Handbook: Primer on Tritium Safe Handling Practices*, U. S. Departament Of Energy Washington, D.C. 20585.
- [26] ROBERT HAIGHT, JOSEPH WERMER and MICHAEL FIKANI, *Tritium Production by Fast Neutrons on Oxygen: An Integral Experiment*, Journal of Nuclear Science and Technology, 39:sup2, 1232-1235, DOI: [10.1080/00223131.2002.10875326](https://doi.org/10.1080/00223131.2002.10875326).
- [27] INSTITUT DE RADIOPROTECTION ET DE SURETÉ NUCLÉAIRE *Tritium and the environment, Tritium and the environment*, IRSN, Enhancing nuclear safety.
- [28] , REFERENCIAAAA,
- [29] *International Atomic Energy Agency*.
- [30] *Tritium decay image*.
- [31] ZHANG LIN, *Simulation and Optimization Design of SiC-Basaed PN Betavoltaic Microbattery Using Tritium Source*, MDPI Open Access Journal 12/02/2020, DOI:[10.3390/cryst10020105](https://doi.org/10.3390/cryst10020105)
- [32] BLAUVELT, R.K., DEATON, M.R. and GILL, J.T., *Health Physics Manual of Good Practices for Tritium Facilities*, EG and G Mound Applied Technologies, Miamisburg, OH (United States), Technical Report, 01 December 1991, DOI: [10.2172/266889](https://doi.org/10.2172/266889).
- [33] TSUYOSHI MASUDA and TOSHITADA YOSHIOKA, *Estimation of radiation dose from ingested tritium in humans by administration of deuterium-labelled compounds and food*, Scientific reports, 02 February 2021, DOI: [10.1038/s41598-021-82460-5](https://doi.org/10.1038/s41598-021-82460-5).

- [34] Z. PIETRZAK-FLIS, I. RADWAN, Z. MAJOR and M. KOWALSKA, *Tritium Incorporation in Rats Chronically Exposed to Tritiated Food or Tritiated Water for Three Successive Generations*, Journal of Radiation Research, Vol 22, Issue 4, December 1981, page 434-442 DOI: [10.1269/jrr.22.434](https://doi.org/10.1269/jrr.22.434).
- [35] J.R. MARTIN and J.J. KORANDA, *Biological Half-Life Studies of Tritium in Chronically Exposed Knagaroo Rats*, Journal of Radiation Research, Vol 50, Issue 2, May 1972, page 426-440 PMID: **5025235**.
- [36] T STRAUME and A. L. CARSTEN, *Tritium radiobiology and relative biological effectiveness*, Health Physics, Vol. 65, Number 6, December 1993, DOI: [10.1097/00004032-199312000-00005](https://doi.org/10.1097/00004032-199312000-00005) .
- [37] RYTOEMAA, T., SALTEVO, J. and TOIVONEN, H., *Radiotoxicity of Tritium-Labelled Molecules*, International Atomic Energy Agency symposium, IAEA, Vienna: Biological Implications of Radionuclides Released from Nuclear Industries, INIS Vol. 11, INIS Issue. 13, Reference Number, 11535484, 1979.
- [38] INTERNATIONAL COMMISSION ON RADIOLOGICAL PROTECTION, ICRP, *Recommendations of the ICRP. Annals of the ICRP, 21(1.3), 1991a. 1990. Oxford, Pergamon Press (Publication 60)..*
- [39] WORLD HEALTH ORGANIZATION, WHO, *Guidelines for Drinking-Water Quality. Vol 1. Third Edition. Geneve, Switzerland, 2004.*
- [40] INTERNATIONAL COMMISSION ON RADIOLOGICAL PROTECTION, ICRP, *Age-dependent doses to members of the public from intake of radionuclides: Part 5. Compilation of ingestion and inhalation dose coefficients. Oxford, Pergamon Press (International Commission on Radiological Protection Publication 72), 1996.*
- [41] DÉPARTEMENT FÉDÉRAL DE L'INTÉRIEUR, DFI (FEDERAL DEPARTMENT OF THE INTERIOR), *Ordonnance du DFI sur les sub-*

- stances étrangères et les composants dans les denrées alimentaires (817.021.23), 2006, Switzerland (in French).
- [42] ONTARIO MINISTRY OF THE ENVIRONMENT, *Ontario Drinking Water Objectives*. Toronto, Ontario, 1994.
- [43] QUÉBEC, *Résultats du programme de surveillance de l'environnement du site de Gentilly. Rapport annuel 2006*. Québec, Canada..
- [44] RUSSIA, *NRB-99 Radiation Safety Norms*, 2007.
- [45] AUSTRALIAN GOVERNMENT, NATIONAL HEALTH AND MEDICAL RESERCH COUNCIL and NATURAL RESOURCE MANAGEMENT MINISTERIAL COUNCIL, *AustralianDrinking Water Guideilnes 6*, National Water Quality Managment Strategy, Version 3.6, Updated March 2011.
- [46] NUCLEAR ENERGY AGENCY, NEA, *Radiation and Nuclear Safety Authority*, 1993. Radioactivity of Household Water. ST 12.3. Erweko Paintuote, Helsinki, Finland, 1994.
- [47] OFFICE OF ENVIRONMENTAL HEALTH HAZARD ASSESSMENT, OEHHA, *Public Health Goals for Chemicals in Drinking Water-Tritium*. OEHHA, California Enfironmental Protection Agency, California USA, September, 2007.
- [48] UNITED STATES ENVIRONMENTAL PROTECTION AGENCY, US EPA, *Drinking Water Requirements for States and Public Water Systems*, Radionuclides Rule, 1976.
- [49] INSTITUT DE RADIOPROTECTION ET DE SÛRETÉ NUCLÉAIRE, IRSN (RADIOPROTECTION AND NUCELAR SAFETY INSTITUTE), *Bilan de l'état radiologique de l'environnement français de 2015 à 2017*. France.

- [50] BUNDESAMT FÜR STRAHLENSCHUTZ, BMU (FEDERAL OFFICE FOR RADIATION PROTECTION), *Environmental Radioactivity and Radiation Exposure*, Annual Report, 2005, (Jahresbericht 2005). BMU, Bonn, Germany (in German).
- [51] CONSEJO DE SEGURIDAD NUCLEAR, CSN, NUCLEAR SAFETY COUNCIL, *National Regulation of Radionuclides*.
- [52] EUROPEAN ATOMIC ENERGY COMMUNITY, EURATOM, *Council directive 2013/15/euratom*, October, 2013. Laying down requirements for the protection of the health of the general public with regard to radioactive substances in water intended for human consumption.
- [53] M. N. AL-HADDAD, A. H. FAYOUMI and F. A. ABU-JARAD, *Calibration of a liquid scintillation counter to assess tritium levels in various samples*, Nuclear Instruments and Methods in Physics Research A, Volume 438, Issues 2-3, December 1999, Pages 356-361, DOI: [10.1016/S0168-9002\(99\)00272-7](https://doi.org/10.1016/S0168-9002(99)00272-7).
- [54] K. J. HOFSTETTER and H. T. WILSON, *Aqueous Effluent Tritium Monitor Development*, Fusion Technology, Volume 21, 2P2, Pages 446-451, March 1992, DOI: [10.13182/FST92-A29786](https://doi.org/10.13182/FST92-A29786).
- [55] M. PALOMO. A. PEÑALVER, C. AGUILAR and F. BORRULL, *Tritium activity levels in environmental water samples from different origins*, Applied Radiation and Isotopes, Volume 65, Issue 9, September 2007, Pages 1048-1056, DOI: [10.1016/j.apradiso.2007.03.013](https://doi.org/10.1016/j.apradiso.2007.03.013).
- [56] R. A. SIGG, J. E. McCARTY, R. R. LIVINGSTON and M. A. SANDERS, *Real-time aqueous tritium monitor using liquid scintillation counting*, FNuclear Instrument and Methods in Physics Research A, Volume 353, Issues 1-3, 30 Decembre 1994, Pages 494-498 DOI: [10.1016/0168-9002\(94\)91707-8](https://doi.org/10.1016/0168-9002(94)91707-8).
- [57] N. P. KHERANI, *An alternative approach to tritium-in-water monitoring*, Nuclear and Methods in PHysics Research A, Volume 484,

Issues 1-3, 21 May 2002, Pages 650-659 DOI: [10.1016/S0168-9002\(01\)02008-3](https://doi.org/10.1016/S0168-9002(01)02008-3)

- [58] Z. CHEN, S. PENG, D. MENG Y. HE and H. WANG, *Theoretical study of energy deposition in ionization chambers for tritium measurements*, Review of Scientific Instruments, 84, 103302, 2013, DOI: [10.1063/1.4825032](https://doi.org/10.1063/1.4825032).
- [59] C. G. ALECU, U. BESSERER, B. BORNSCHEIN, B. KLOPPE, Z. KÖLLÖ and J. WENDEL, *Reachable Accuracy and Precision for Tritium Measurements by Calorimetry at TLK*, Fusion Science and Technology, 60:3, 937-940, DOI: [10.13182/FST11-A12569](https://doi.org/10.13182/FST11-A12569).
- [60] A. BÜKKI-DEME, C. G. ALECU, B. KLOPPE and B. BORNSCHEIN, *First results with the upgraded TLK tritium calorimeter IGC-V0.5*, Fusion Engineering and Design, Volume 88, Issue 11, November 2013, Pages 2865-2869 DOI: [10.1016/j.fusengdes.2013.05.066](https://doi.org/10.1016/j.fusengdes.2013.05.066).
- [61] M. MATSUYAMA, Y. TORIKAI, M. HARA and K. WATANABE, *New Technique for non-destructive measurements of tritium in future fusion reactors*, IAEA Nuclear Fusion, Volume 47, Number 7, S464, June 2007, DOI: [10.1088/0029-5515/47/7/S09](https://doi.org/10.1088/0029-5515/47/7/S09).
- [62] M. MATSUYAMA, *Development of a new detection system for monitoring high-level tritiated water*, Fusion Engineering and Design, Volume 83, Issue 10-12, December 2008, Pages 1438-1441 DOI: [10.1016/j.fusengdes.2008.05.023](https://doi.org/10.1016/j.fusengdes.2008.05.023).
- [63] S. NIEMES, M. STURM, R. MICHLING and B. BORNSCHEIN, *High Level Tritiated Water Monitoring by Bremsstrahlung Counting Using a Silicon Dipt Detector*, Fusion Science and Technology, 67:3, 507-510, 2015, DOI: [10.13182/FST14-T66](https://doi.org/10.13182/FST14-T66).
- [64] K. S. SHAH, P. GOTHSKAR, R. FARRELL and J. GORDON, *High Efficiency Detection of Tritium Using Silicon Avalanche Photodiodes*,

IEEE Transactions on Nuclear Science, Volume 44, Issue 3, June 1997,  
**DOI: 10.1109/23.603750**

- [65] P. JEAN-BAPTISTE, E. FOURRÉ, A. DAPOIGNY, D. BAUMIER, N. BAGLAN and G. ALANIC, *<sup>3</sup>He mass spectrometry for very low-level measurement of organic tritium in environmental samples*, Journal of Environmental Radioactivity, Volume 101, Issue 2, February 2010, Pages 185-190, **DOI: https://doi.org/10.1016/j.jenvrad.2009.10.005**.
- [66] C. BRAY, A. PAILOUX and S. PLUMERI, *Tritiated water detection in the 2.17  $\mu\text{M}$  spectral region by cavity ring down spectroscopy*, Nuclear Instruments and Methods in Physics Research A, Volume 789, 21 July 2015, Pages 43-49, **DOI: 10.1016/j.nima.2015.03.064**.
- [67] M. MURAMATSU, A. KOYANO and N. TOKANUGA, *A Scintillation Probe for Continuous Monitoring of Tritiated Water*, Nuclear Instruments and Methods, Volume 54, Issue 2, October 1967, Page 325-326, **DOI: 10.1016/0029-554X(67)90645-3**.
- [68] A. A. MOGHISSI, H. L. KELLEY, C. R. PHILLIPS and J. E. REGNIER, *A Tritium Monitor Based on Scintillation*, Nuclear Instruments and Methods, Volume 68, Issue 1, 1 February 1969, Page 159, **DOI: 10.1016/0029-554X(69)90705-8**.
- [69] R. V. OSBORNE, *Detector for Tritium in Water*, Nuclear Instruments and Methods, Volume 77, Issue 1, 1 January 1970, Page 170-172, **DOI: 10.1016/0029-554X(70)90596-3**.
- [70] A. N. SINGH, M. RATNAKARAN and K. G. VOHRA, *An Online Tritium-in-Water Monitor*, Nuclear Instruments and Methods, Volume 236, Issue 1, 1 May 1985, Page 159-164, **DOI: 10.1016/0168-9002(85)90141-X**.
- [71] M. RATNAKARAN, R. M. REVETKAR, R. K. SAMANT and M. C. ABANI, *A Real-time Tritium-In-Water Monitor for Measurement Of*

*Heavy Water Leak To The Secondary Coolant*, International congress of the International Radiation Protection Association, Volume 32, Issue 15, 14-19 May 2000, P-3a-197, Reference number: **32015986**

- [72] K. J. HOFSTETTER and H. T. WILSON, *Aqueous Effluent Tritium Monitor Development*, Fusion Technology, Volume 21, 2P2, 1992, Pages 446-451, **DOI: 10.13182/FST92-A29786**.
- [73] K. J. HOFSTETTER and H. T. WILSON, *Continuous Tritium Effluent Water Monitor at the Savannah River Site*, International conference on advances in liquid scintillation, Vienna (Austria), 14-18 September 1992.
- [74] *Tritium, Interreg Sudoe Program. Tritium website.*
- [75] CERN COLLABORATION, *Geant4: A toolkit for the simulation of the passage of particles through matter.. Website.*
- [76] GLENN F. KNOLL, *Radiation Detection and Measurement*, Third Edition, John Wiley and Sons, Inc. 1999.
- [77] WILLIAM R. LEO, *Techniques for Nuclear and Particle Physics Experiments: a how-to approach*, Second Revised Edition, Springer-Verlag Berlin Heidelberg GmbH, 1994. **DOI: 10.1007/978-3-642-57920-2**.
- [78] SAINT-GOBAIN CERAMICS AND PLASTICS, INC., *Scintillating Optical Fibers*, It's What's Inside that Counts, 2005-14. **Data sheet**.
- [79] , , .
- [80] , , .
- [81] HAMAMATSU PHOTONICS K.K., *Photonmultiplier tube R8520-406/R8520-506*. **Data sheet**.

- [82] JAVIER PÉREZ PÉREZ, *Caracterización de los Fotomultiplicadores R8520-06SEL para NEXT*, 25-06-2010.
- [83] DAVID LORCA GALINDO, *Tesis: SiPM based tracking for detector calibration in NEXT*, Departamento de física atómica, molecular y nuclear, Universidad de Valencia (UV), Valencia, Spain, 03/2015.
- [84] OSI OPTELECTRONICS, *Characteristics and Applications*.
- [85] HAMAMATSU PHOTONICS K.K. SOLID STATE DIVISION, *MPPC Multi-Pixel Photon Counter S13360-6050*. **Data sheet**.
- [86] HAMAMATSU PHOTONICS K.K. SOLID STATE DIVISION, *MPPC Multi-Pixel Photon Counter S13360-6075*. **Data sheet**.
- [87] HAMAMATSU PHOTONICS K.K. SOLID STATE DIVISION, *MPPC Multi-Pixel Photon Counter S13361-6050*. **Data sheet**.
- [88] HAMAMATSU PHOTONICS K.K. SOLID STATE DIVISION, *MPPC Multi-Pixel Photon Counter S13361-3050*. **Data sheet**.
- [89] SENSL SENSE LIGHT, *Introduction to the SPM TECHNICAL NOTE*. February 2017 **Document**.
- [90] KEITHLEY, A GREATER MEASURE OF CONFIDENCE, *Model 6487 Picoammeter/voltage source, Manual reference*. **Data sheet**.
- [91] TENNELEC, *Model TC 952 High Voltage Supply, Manual reference*. **Data sheet**.
- [92] WENZEL ELECTRONIK, *Model N 1330-4 High Voltage Power Supply*. **Website**.
- [93] PHILIPS SCIENTIFIC, *Model 740 Quad Linear Fan-In/Out, Manual reference*. **Data sheet**.
- [94] ORTEC, *Model 9326 FastPreamplifier, Manual reference*. **Data sheet**.

- [95] ORTEC, *Model 575A Amplifier, Manual reference.* **Data sheet.**
- [96] ORTEC, *Model 671 Spectroscopy Amplifier, Manual reference.* **Data sheet.**
- [97] ORTEC, *Model CF8000 Octal Constant-Fraction Discriminator, Manual reference.* **Data sheet.**
- [98] CAEN, *Model 84, 4 channels discriminator.* **Data sheet.**
- [99] LECROY, *Model 465 Coincidence Unit, Manual reference.* **Data sheet.**
- [100] CERN, *Coincidence Unit Type N6234, Manual reference.* **Data sheet.**
- [101] ORTEC, *Model 416A Gate and Delay Generator, Manual reference.* **Data sheet.**
- [102] AMPTEK, *MCA8000D, Pocket MCA, Digital Multichannel Analyzer, Manual reference.* **Data sheet.**
- [103] PETsys Electronics. **Website.**
- [104] Thorlabs, Inc.. **Website.**
- [105] SAINT-GOBAIN CERAMICS AND PLASTICS, INC., *Optical fiber BCF-98, Manual reference.* **Manual reference.**
- [106] THORLABS, *LED430L - 430 nm LED with a Glass Lens, 8 mW, TO-18.* **Datasheet.**
- [107] PALL THEODÓRSSON, *Measurement of weak radioactivity,* World Scientific, 1996.
- [108] R D EVANS, *The Atomic Nucleus,* McGraw-Hill, Inc., 1996.

- [109] P.A. ZYLA ET AL., (*Particle Data Grup*), *PDG, Prog. Theor. Exp. Phys.* **2020** no. 8, 083C01 (2020). **Website DOI:** [10.1093/ptep/ptaa104](https://doi.org/10.1093/ptep/ptaa104).
- [110] HIROYUKI SAGAWA & ITSUMASA URABE (2001), *Estimation of Absorbed Dose Rates in Air Based on Flux Densities of Cosmic Ray Muons and Electrons on the Ground Level in Japan*, *Journal of Nuclear Science and Technology*, 38:12, 1103-1108, **DOI:** [10.1080/18811248.2001.9715142](https://doi.org/10.1080/18811248.2001.9715142).
- [111] T. SZÜCS, D. BEMMERER, T. P. REINHARDT, K. SCHMIDT, M. P TAKÁCS, A. WAGNER, L. WAGNER, D. WEINBERGER AND K. ZUBER, *Cosmic-ray induced background intercomparison with actively shielded HPGe detectors at underground locations*. **DOI:** [10.1140/epja/i2015-15033-0](https://doi.org/10.1140/epja/i2015-15033-0).
- [112] EPIC CRYSTAL, *Plastic scintillator of Epic Crystal, Manual reference. Data sheet*.
- [113] THORLABS, *Guide to connectorization and polishing optical fibers*, 2006. **Manual Reference**.
- [114] INDISTROĀÑ FIBER OPTICAL, *POF Cutter block*. **Website**.
- [115] DAVID SÁEZ-RODRÍGUEZ, KRISTIAN NIELSEN, OLE BANG AND DAVID JOHN WEBB, *Simple Room Temperature Method for Polymer Optical Fibre Cleaving*, *Journal of lightwave technology*, vol 33, No. 23, December 1, 2015. **DOI:** [10.1109/JLT.2015.2479365](https://doi.org/10.1109/JLT.2015.2479365).
- [116] S.H. LAW, J.D. HARVEY, R.J. KRUHLAK, M. SONG, E. WU, G.W. BARTON, M.A. VAN EIJKELENBORG AND M.C.J. LARGE, *Cleaving of microstructured polymer optical fibres*. **DOI:** [10.1016/j.optcom.2005.08.011](https://doi.org/10.1016/j.optcom.2005.08.011).
- [117] NANOTEC, *ST4209S1404-A - STEPPER MOTOR NEMA 17*. **Data sheet**.

- [118] *ARDUINO*, **Website**.
- [119] *CNC shield V3.0, Reference manual*.
- [120] *ALLEGRO Driver Pololu A4988, DMOS Microstepping Driver with Translator And Overcurrent Protection, Data sheet*.
- [121] *TEXAS INSTRUMENTS Driver DRV8825 Stepper Motor Controller IC, Data sheet*.
- [122] *Driver TMC2208, Step/Dir Drivers for Two-Phase Bipolar Stepper Motors up to 2A peak- StealthChop for Quiet Movement- UART Interface Option, Data sheet*.
- [123] ROITHNER LASERTECHNIK GMBH *LED435-03, 20 mW, 20 mA, Reference*.
- [124] , , **Reference**.
- [125] SAINT-GOBAIN CERAMICS AND PLASTICS, INC., *BC-630, Silicone Optical Grease, Website*.
- [126] THORLABS, *BK5 - Black Nylon, Polyurethane-Coated Fabric, 5'x9' (1.5m x 2.7m) x 0.005" (0.12 mm) Thick, Datasheet*.
- [127] SAN NOPCO COMPANY, *Wetting property, Website*.
- [128] HANNA INSTRUMENTS, *Multiparamétrico con opciones GPS, sonda autoregistradora, turbidez e ISE, Website*.
- [129] CAEN COMPANY, *Quad Scaler And Preset Counter-Timer, N1145, Datasheet*.
- [130] PHYSIKALISCH-TECHNISCHE BUNDESANSTALT, PTB, BRAUNSCHWEIG AND BERLIN, GERMANY *Calibration Certificate of tritium source, PTB-6.11-2005-1442*.

- [131] SAINT-GOBAIN CERAMICS AND PLASTICS, INC., *Scintillating Optical Fibers*, It's What's Inside that Counts, 2005-14. **Data sheet**.
- [132] HAMAMATSU PHOTONICS K.K., *Photonmultiplier tube R2154-02 2"*. **Data sheet**.
- [133] HAMAMATSU PHOTONICS K.K., *High Voltage Power Supply C11152-01*. **Data sheet**.
- [134] MAXIM INTEGRATED, *Low-Power, Quad, 12-Bit, Voltage-Output DACs with Serial Interface*. **Data sheet**.
- [135] SAINT-GOBAIN, *Scintillating plastic grown with polymeric method*. **Data sheet**.
- [136] CREMAT INC., *CR 111-R2.1 Charge sensitive preamplifier*. **Data sheet**.
- [137] TEXAS INSTRUMENTS, *OPA656 Wideband, Unity-Gain Stable, FET-Input Operational Amplifier*. **Data sheet**.
- [138] LINEAR TECHNOLOGY, *LT111A*. **Data sheet**.
- [139] TEXAS INSTRUMENTS, *SN74AHC1G32 Single 2-Input Positive-OR Gate*. **Data sheet**.
- [140] TEXAS INSTRUMENTS, *SN74LVC1G11DBVR Single 3-Input Positive-AND Gate*. **Data sheet**.
- [141] J. ALLISON, *Geant4 - A simulation toolkit*. DOI:[10.1016/S0168-9002\(03\)01368-8](https://doi.org/10.1016/S0168-9002(03)01368-8)
- [142] PLOT NUCLEAR DATA (NADS), *Physics simulation packages, CRY (cosmic-ray particle showers)*. **Website**
- [143] CHRIS HAGMANN, DAVID LANGE and DOUGLAS WRIGHT, *Cosmic-Ray particle Showers Generator (CRY) for Monte Carlo*

- Transport Codes*, IEEE Nuclear Science Symposium conference record. Nuclear Science Symposium 2:1143-1146, January 2007. **DOI:10.1109/NSSMIC.2007.437209**
- [144] H. BUITEVELD, J.H.M. HAKVOORT, M. DONZE, *Optical properties of pure water*, in:*Proc. 2258 Ocean Optics XII, Bergen, Norway, 1994*. **DOI:10.1117/12.190060**
- [145] S. MAERTENS, ET AL., *Sensitivity of next-generation tritium beta-decay experiments for keV-scale sterile neutrinos*, *J. Cosmol. Astropart. Phys.* 2015 (2015) 020. DOI:10.1088/1475-7516/2015/02/020
- [146] J. ARGYRIADES, ET AL., *Spectral modeling of scintillator for the NEMO-3 and SuperNEMO detectors*, *Nucl.Instrum. Methods A* 625 (2011) 20-28. **DOI:10.1016/j.nima.2010.09.027**
- [147] J B BIRKS, *Scintillations from Organic Crystals: Specific Fluorescence and Relative Response to Different Radiations*, *Proc. Phy. Soc. A* 64 874, April 12th, 1951. **DOI:10.1088/0370-1298/64/10/303**
- [148] B.D. LEVERINGTON, M. ANELLI, P. CAMPANA and R. ROSELLINI, *A 1mm Scintillating Fibre Tracker Readout by a Multi-anode Photomultiplier*, July 5, 2011, arXiv.
- [149] CAEN, TOOLS FOR DISCOVERY, *CAEN V1724, 8 Channels, 14 bit, 100MS/s Digitalizer*. **Data sheet**
- [150] LLOYD, A. CURRIE, *Limits for Qualitative Detection and Quantitative Determination. Application to Radiochemistry*, *Anal. Chem.* 1968, 40, 3, 586-593, March 1, 1968. **DOI: 10.1021/ac60259a007**
- [151] C.D.R. AZEVEDO, A. BAEZA, E. CHAUVEAU, J.A. CORBACHO, J. DÍAZ, J. DOMANGE, C. MARQUET, M. MARTINEZ-ROIG, F. PIQUEMAL, J.F.C.A. VELOSO and N. YAHALALI, *First prototype module development for a tritium in water real-time monitor*.

- [152] C.D.R. AZEVEDO, A. BAEZA, E. CHAUVEAU, J.A. CORBACHO, J. DÍAZ, J. DOMANGE, C. MARQUET, M. MARTINEZ-ROIG, F. PIQUE-MAL, J.F.C.A. VELOSO and N. YAHLALI, *Simulation results of a real-time in water tritium monitor*, *Nuclear Instruments and Methods in Physics Research Section A: Accelerators, Spectrometers, Detectors and Associated Equipment*, Vol. 982, 1 December 2020, pages 164555. DOI: [10.1016/j.nima.2020.164555](https://doi.org/10.1016/j.nima.2020.164555)